DEVELOPMENT AND OPERATION OF AN INTEGRATED SAMPLING PROBE AND GAS ANALYZER FOR TURBULENT MIXING STUDIES IN COMPLEX SUPERSONIC FLOWS

by

JOHN D. WISWALL

Presented to the Faculty of the Graduate School of
The University of Texas at Arlington in Partial Fulfillment
of the Requirements
for the Degree of

MASTER OF AEROSPACE ENGINEERING

THE UNIVERSITY OF TEXAS AT ARLINGTON
AUGUST 2013

Acknowledgements

I would first like to thank my wife Amanda, who has always been encouraging, supportive, and very patient with all of the late nights and long hours. I'm so grateful to have you in my life and I love you. I'd also like to thank my family, particularly my mother Katy, my father Jim, and my two sisters Laura and Hanna.

I'm grateful to my advisor, Dr. Luca Maddalena, for his expertise and guidance every step of the way in this process. Without his experience and willingness to take the time explaining things, this instrument would not be half of what it is today. I'd also like to thank my defense committee of Dr. Lu and Dr. Wilson for their service.

Much deserved gratitude goes to my two research associates, Matthew Crisanti and Fabrizio Vergine. I thank Fabrizio for help running the supersonic facilities and teaching me about mixing physics with vorticity. I thank Matthew for countless hours of assistance, often late nights and weekends, in constructing, re-constructing, and implementing this probe. Matthew's particular expertise in electronics, laboratory operations, and precision modification of very tiny fragile things was invaluable in making this probe as successful as possible. It has been a pleasure to work with both of you.

I thank the MAE department's machinist Kermit Beird for his craftsmanship of the complex machined components for this project and his experienced input. I also thank Maxon Widner IV, who designed the entire traversing system for these experiments and helped ensure that everything ran smoothly.

I would like to thank the NASA Hypersonics Program, the sponsor of our research group's project.

Lastly I would like to thank the people of UTA's Aerodynamics Research Center (ARC). David Carter has been particularly eager to assist in my research efforts, providing experienced input and time into numerous technical issues and ensuring that I don't blow myself up in the

process. I'd also like to thank the late Rodney Duke (2012) for his assistance in the early days. The entire ARC student group has also been helpful and I thank each of you.

August 14, 2013

Abstract

DEVELOPMENT AND OPERATION OF AN INTEGRATED
SAMPLING PROBE AND GAS ANALYZER
FOR TURBULENT MIXING STUDIES IN
COMPLEX SUPERSONIC FLOWS

John D. Wiswall

The University of Texas at Arlington, 2013

Supervising Professor: Luca Maddalena

For many aerospace applications, mixing enhancement between co-flowing streams has been identified as a critical and enabling technology. Due to short fuel residence times in scramjet combustors, combustion is limited by the molecular mixing of hydrogen (fuel) and air. Determining the mixedness of fuel and air in these complex supersonic flowfields is critical to the advancement of novel injection schemes currently being developed at UTA in collaboration with NASA Langley, and are intended to be used on a future two-stage to orbit (~Mach 16) hypersonic air-breathing vehicle for space access.

Expanding on previous work, an instrument has been designed, fabricated, and tested in order to measure mean concentrations of injected helium (a passive scalar used instead of hazardous hydrogen) and to quantitatively characterize the nature of the high-frequency concentration fluctuations encountered in the compressible, turbulent, and high-speed (up to Mach 3.5) complex flows associated with the new supersonic injection schemes. This important high-frequency data is not yet attainable when employing other techniques such as Laser Induced Fluorescence, Filtered Rayleigh Scattering or mass spectroscopy in the same complex supersonic flows.

The probe operates by exploiting the difference between the thermodynamic properties of two species through independent massflow measurements and calibration. The probe samples isokinetically from the flowfield's area of interest and the helium concentration may be uniquely determined by hot-film anemometry and internally measured stagnation conditions. The final design has a diameter of 0.25" and is only 2.22" long. The overall accuracy of the probe is 3% in molar fraction of helium. The frequency response of mean concentration measurements is estimated at 103 Hz, while high-frequency hot-film measurements were conducted at 60 kHz. Additionally, the work presents an analysis of the probe's internal mixing effects and the effects of the spatial-temporal characteristic scales of the flow on the resulting time-area-averaged concentration measurements.

Two series of experiments were performed to verify the probe's design; the first used Schlieren photography and verified that the probe sampled from the supersonic flowfield isokinetically. The second series involved traversing the probe across a free mixing layer of air and helium, to obtain both mean concentration and high-frequency measurements. High-frequency data was statistically analyzed and inspection of the Probability Density Function (PDF) of the hot-film response was instrumental to interpret how well the resulting average mixing measurements represent these types of complex flows.

The probe is minimally intrusive, has accuracy comparable to its predecessors, has an improved frequency response for mean concentration measurements, and samples from a very small area in the flowfield.

Table of Contents

List of Figures

List of Tables

Nomenclature

A_1*	Virtual nozzle area
A_t	Throat area
a	Calibration constant
b	Calibration constant
C	Specific heat
C_i	Mass concentration of species i
C*	Critical, sonic fluid function
D	Mass diffusion coefficient
d	Hot-film diameter
E	Energy
G	Transfer function
h	Heat transfer coefficient
I	Current
k	Thermal conductivity
L	Integral scale
l	Hot-film active sensing length
l_k	Kolmogorov length scale
M	Mach number
MW	Molecular weight
Nu	Nusselt number
n	Unit normal vector
P	Pressure
Pr	Prandtl number
Q	Heat transfer
R	Specific gas constant

Re	Reynolds number
R_f	Hot-film resistance
R_{HFC}	Hot-film circuit resistance
R_s	Series resistance
r	Vortex radius
T	Temperature
t	Time
TKE	Turbulent kinetic energy
U	Uncertainty
u	Streamwise velocity
V	CTA Voltage
X_{He}	Molar concentration of helium
x	Spanwise horizontal coordinate
y	Spanwise vertical coordinate
z	Streamwise coordinate

Greek

Γ	Vortex circulation
γ	Specific heat ratio
ε_{yy}	Normal strain rate
θ_c	Cone half-angle
θ_v	Freestream velocity angularity
κ	Wave number
μ	Dynamic viscosity
ρ	Density
τ	Time constant

Chapter 1

Introduction

1.1 Motivation and Scope

Since the origin of flight at Kitty Hawk by the Wright brothers' Flyer I in 1903, engineers have aspired to build faster and higher-flying aircraft. The supersonic combustion ramjet, or scramjet, has the potential to make rapid global transit and affordable space access a reality. Scramjet engine research has been ongoing since the 1960s, and a comprehensive overview of ramjet propulsion, both subsonic and supersonic, is provided by Fry[1]. The first hypersonic scramjet flight test was conducted in Russia in 1991; the vehicle operated using a scramjet engine which achieved Mach 5.35, and then Mach 5.6 later in 1995. A major milestone in scramjet engine technology was achieved when NASA's scramjet-powered X-43A was flown freely for 10 seconds at Mach 7 in March 2004, and then at Mach 10 for 11 seconds in November 2004. Boeing's scramjet-powered X-51 later broke the record for the longest air-breathing hypersonic flight, when in its 4^{th} flight test it achieved Mach 5.1 and flew for 240 seconds in May 2103. Scramjet engine research is ongoing, and some interesting engineering challenges exist.

Figure 1 is a schematic for the basic layout of a scramjet engine. Scramjets are unique in that the aircraft body is integrated into the propulsion system by means of appropriate shock-induced compression stages. In the combustion chamber, the injected fuel is mixed into the supersonic air, combusted, and expanded through the nozzle. Unlike the ramjet, the flow is supersonic through the entire scramjet engine. Due to scramjet's very high freestream velocity, fuel residence time in the combustor is on the order of milliseconds and combustion of the majority of the fuel becomes a major challenge. Mach numbers in the combustor are generally around $^1/_3$ of the vehicle Mach number, which dictates the optimal fuel. For M_∞ < 7-8, hydrocarbons are used, with faster scramjets using hydrogen. Hydrocarbons are preferred for their higher energy density, but additional time for vaporization and cracking are problematic at

higher Mach numbers (and therefore higher enthalpies), whereas hydrogen cracks at a higher enthalpy and can rapidly vaporize if stored in liquid form. Cracking is an endothermic process, which reduces the fuel's potential to produce thrust. Our study models a TSTO vehicle at Mach 16-18 in order to achieve orbit, and so hydrogen is the clear choice. Within these few milliseconds, the fuel and air must mix and then combust before exiting the nozzle. Combustion of air and hydrogen is a fast process relative to the fuel residence time, and so the entire supersonic combustion process is *mixing limited*. Unmixed fuel cannot burn, and is simply discharged out the nozzle. Hydrogen and air mixing enhancement is desirable to achieve complete combustion, resulting in reduced combustor length, reduced drag and heat transfer within the combustion chamber, and increased net thrust. Total pressure losses must also be considered for different injection schemes to improve or maintain overall engine efficiency.

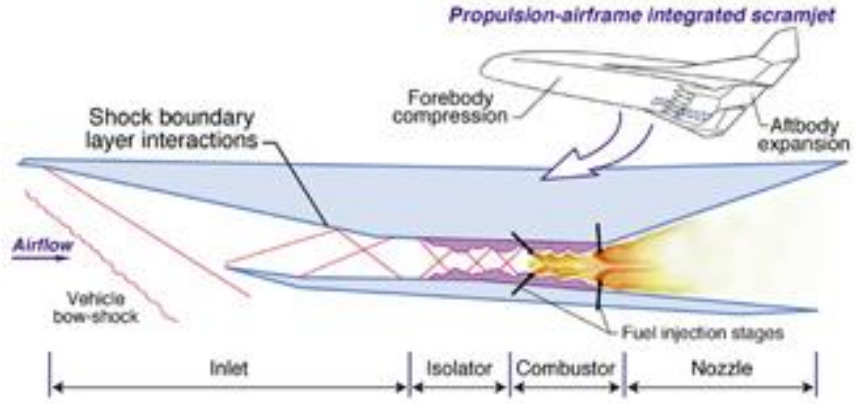

Figure 1: Scramjet Schematic (source: www.nasa.gov)

This thesis describes the development and implementation of an instrument to assess scramjet fuel injection methods. This probe is a useful tool for turbulent mixing studies, as part of an ongoing research effort at UTA's Aerodynamics Research Center (ARC) to design and test an improved scramjet fuel injection system, with a focus on the fuel and air mixing process. A good injection scheme should provide the appropriate dispersion of the fuel plume in the combustor and subsequent molecular mixing. Lifting the fuel plume from the combustor walls is

necessary to decrease the structural heat loads while a molecularly mixed fuel/oxidizer is a prerequisite for combustion. By measuring fuel concentration and then correlating this with a particular mixing enhancement technique, its effectiveness may be assessed and then iteratively improved. This probe was designed to measure the concentration of a passive scalar (testing with helium instead of hazardous hydrogen) in a complex, turbulent, vortex-dominated supersonic flow at Mach 2.5. Due to a large projected test matrix and short test durations, a high-frequency response was an important design requirement to reduce testing time. Relative accuracy of concentration measurements was conserved from previous designs of the same type. High-frequency fuel concentration components may be retrieved, in order to evaluate mixedness of the fuel and air and assess the injector. The principle of operation is discussed at length in Chapter 2.

1.2 Gas Composition Measurements

Several techniques enable gas composition measurement for dynamic systems. Two preferred methods are direct sampling with mass spectroscopy and laser-based flow diagnostics. Both methods only offer limited information for particular flow scenarios, which in our case is a turbulent, supersonic, 3-dimensional flowfield of a binary gas mixture with intermittent vortical structures. Neither technique can resolve high-frequency fluctuations in concentration, which are critical for the detection of concentration intermittencies in the freestream and how this affects helium dispersion. The probe in this thesis is able to partially resolve this high-frequency component of helium concentration, as will be demonstrated.

Direct sampling with mass spectroscopy involves extraction of the gas mixture through a sampling point which is then transferred to a spectrometer. The spectrometer ionizes the gas mixture, sorts individual species according to their mass-to-charge ratios, dynamically detects the quantities of these charged particles, and then correlates these readings to a database of species with known physical properties. Modern mass spectrometers can resolve gas

compositions of an arbitrary number of species to the order of parts per billion. Mass spectrometers are typically large, and not practically integrable inside supersonic flowfields. Therefore some length of plumbing is required to connect the sampling point to the mass spectrometer outside the flowfield. The gases continue to mix inside this channel, effectively damping high-frequency information. The technique works well in flowfields where gas composition does not change in time for a fixed point in space, but this is not typical for mixing investigations. These systems have a relatively poor frequency response as well; the mass spectrometer itself is not necessarily slow, but the particle flush time through the plumbing can greatly increase the overall experiment time, which is a major limitation for tunnels with short test durations.

Laser-based flow diagnostics are appealing because the entire flowfield can be spatially resolved simultaneously, within the limitations of the optics, laser system, and imaging devices employed. Two common techniques for measuring gas composition are laser-induced-fluorescence (LIF) and Filtered Rayleigh Scattering (FRS). The principle of these techniques is similar; a laser sheet is cast on the flowfield while a high-speed camera records light intensity that corresponds to some flowfield property to be measured. Tracer species are targeted by a laser of appropriate wavelength. In LIF, individual molecules of the tracer species absorb the incident laser light and become excited. This process is *inelastic,* i.e. energy is transferred from the incident photon to the tracer species molecule, so the emitted photon has less energy, and thus a longer wavelength. It is possible, with appropriate assumptions on the state of the flow, to directly retrieve the mole fraction of the tracer species by means of a digital imaging device such as an intensified CCD camera. In contrast, Rayleigh scattering is *elastic*, i.e. the incident photon has the same wavelength as the emitted photon. Rayleigh scattering outputs a weaker signal, but is simpler to employ in practice. To calculate gas composition using either technique, the local thermodynamic state of the mixture must be assumed or independently measured. For supersonic flows, sufficient flowfield information is often difficult or impossible to obtain without

two or more simultaneous measurements. To this end, FRS and LIF measurements are often performed simultaneously, which is both complex and costly. Due to these complicating issues inherent in non-intrusive techniques, intrusive probe-based techniques are often viewed as an attractive alternative. Additionally, these optical systems are often limited by the operational frequency of the cameras and lasers used, making high-frequency measurements unattainable.

The integrated sampling probe and gas analyzer only works for a *binary* gas mixture where the two species have selectively different thermodynamic properties. Using a hot-wire or hot-film sensor with an anemometer and measuring the local thermodynamic state, the gas composition is implicitly calculated by exploiting the difference in the properties of the two gases, particularly the molecular weight. This technique effectively reduces the size of the sensing element to that of a thin filament, which may be positioned very close to the sampling point, thus reducing the effects of internal mixing and allowing the measurement of high-frequency components. Additionally, the probe samples the binary gas mixture isokinetically, i.e. independent of the flowfield Mach number, therefore reducing the probe's intrusiveness in supersonic flow.

The optimal measurement technique is dependent on both the flowfield characteristics and the temporal resolution of concentration data required. For flowfields without temporal variations in gas composition, integrated sampling and mass spectroscopy is an excellent solution. For flowfields where the thermodynamic state at each point may be reasonably assumed or independently measured, either laser-based technique would work well. The integrated sampling probe and gas analyzer is ideally suited for flowfields in which the local thermodynamic state and gas composition fluctuate intermittently in both space and time, i.e. flowfields where other techniques cannot reproduce the same measurement quality. Its ability to resolve high-frequency components of helium concentration is a major benefit when studying turbulent mixing with large expected fluctuations.

1.3 Previous Concentration Probe Designs

The first instrument of this type was designed and built by Brown and Rebollo[2] in 1972. Since that time, many adaptations have been used successfully, particularly in the *supersonic* flow regime. This original probe was designed to operate in *subsonic* flow, and is well-refined for a first prototype. A schematic of the probe geometry is shown below:

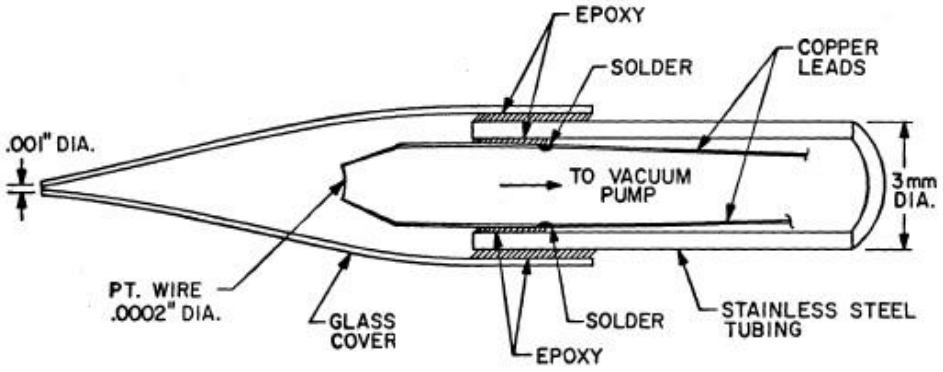

Figure 2: Brown and Rebollo Probe[2]

The design consists of a 0.0002” (7.9 μm) platinum filament attached to 3 mm stainless steel tubing and a drawn glass cover with a 0.001” (39 μm) inlet. The inlet is a fine hole that was exposed by grinding a drawn glass tip, and therefore the surrounding surface is blunt. The hot-wire leads are connected to an external constant temperature anemometer (CTA) and flexible tubing attaches directly to a vacuum pump. Freestream pressure measurements are taken with a separate instrument, but are still required to uniquely correlate the instrument output to the correct composition. The ideal use for this particular probe is subsonic applications, where the freestream total pressure may be assumed constant in the flowfield. In this particular case when pressure and temperature remain constant, the molar fraction of helium may be uniquely determined by the CTA voltage obtained from the heated platinum filament.

The Brown and Rebollo probe is frequently referenced in the literature and has been reproduced for numerous applications in subsonic flow. The small inlet and sensor size are

desirable because the probe can resolve measurements at smaller length scales than the supersonic probes, and therefore more accurately (but not completely) model the physics of molecular mixing than larger probes, which will be discussed at length in Section 6.2. It has a frequency response of 5 kHz, can detect 1% molar fraction of helium in air according to the designer, and is simple to construct and quite rugged. Without integrated pressure or temperature measurements, the probe cannot be used for non-uniform flowfields where the thermodynamic state changes, but it works well for the experiments for which it was intended. These limitations are tolerable in subsonic flow where total pressure measurements are comparatively simple and total temperatures may be assumed constant. Efforts to improve upon this design are scarce in the literature, although many researchers have adapted the concept to a rake of several probes to reduce testing time, e.g. Birch et. al.[3].

The first adaptation to *supersonic* flow was introduced in 1989 by Ng and Ninneman[4]. The design is similar to the subsonic probe, but incorporates a downstream throat and integrated pressure measurement. A schematic of the probe geometry is shown below:

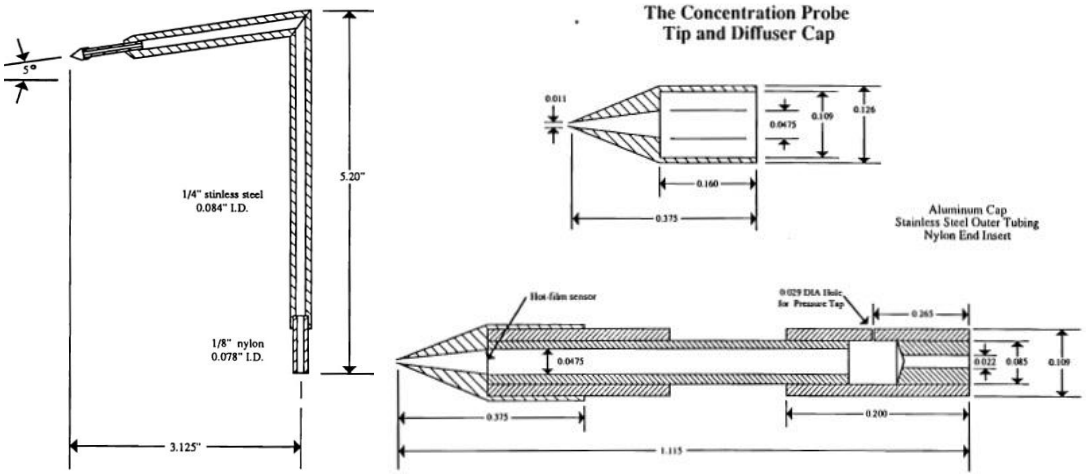

Figure 3: Ng and Ninneman Probe[4]

This design and others were specifically tailored to measure concentration close to a wall in a wind tunnel, hence the downward angle of the inlet. A second downstream throat is

attached to a vacuum pump, and thus forces a normal shock to occur inside the probe due to the massflow constraint, preventing the normally occurring standoff bow shock. There is a divergent channel immediately downstream of the inlet, where the incoming mixture expands supersonically, and the channel is designed such that a normal shock occurs upstream of the sensors. Aerodynamics of the supersonic configuration will be discussed at length in Chapter 2. It should be noted that this probe is larger than Brown and Rebollo's subsonic design. This is for two main reasons; first, the leading edge must be sharp, within practical machining limitations, to minimize the aerodynamic effects of a blunt leading edge in supersonic flow. Blunt surfaces create local standoff shocks, which violates the critical assumption of isokinetic sampling, to be explored in depth in Section 3.2. Second, additional internal space is required for an integrated pressure measurement and the throat. The inlet diameter is 0.011" (0.43 mm) and the probe is encased in ¼" (6.4 mm) stainless steel tubing. As seen in most supersonic designs, the wire and vacuum line exit is typically integrated into the body to minimize blockage area in the test section and avoid starting issues. In this probe, a pressure transducer is connected externally with ~1 meter of tubing, and hence a considerable time lag is introduced into the overall measurement, resulting in a frequency response of 10 Hz. Even though the CTA can resolve up to 20 kHz, helium concentration measurements are limited by the pressure lag. Ng and Ninneman determined this probe to have a typical accuracy of 2% molar fraction of helium. A typical set of calibration curves is below:

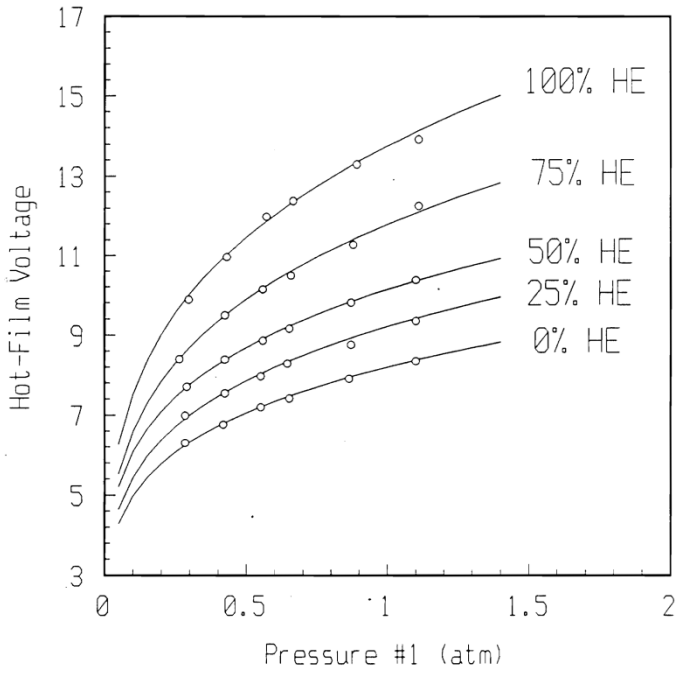

Figure 4: Ng and Ninneman Calibration Curve[4]

These calibration curves are similar for all probes in this class. Figure 4 is a map of helium concentrations which are uniquely correlated to the probe's measured anemometer voltage and internal pressure. Calibration takes place over a test matrix of helium concentrations and pressures, and these power law curves are fit to the data. Intermediate values of concentration are calculated through interpolation. Adaptations of this base design have been numerous, since test facilities have different traversing abilities, space limitations, and flowfield conditions. However, the basic principle of operation is preserved. Two more previous adaptations of this design will be explored in this introduction.

In 1998 Xillo[5] designed a probe which integrated a subminiature pressure transducer inside the body, rather than using a static pressure tap. This probe measures temperature with the use of 2 hot-films operating at different overheat ratios. Xillo's goal was to improve the overall frequency response by implementing faster instrumentation. This model positioned the two hot-films upstream of the normal shock that occurs inside the divergent channel, intending

to reduce internal mixing effects. Unfortunately, this hot-film placement violates one of the crucial assumptions of constrained mass flow through the throat. This made the instrument sensitive to changes in the freestream, whereas the design intention is to sample isokinetically, therefore making the probe sensitive *only* to the helium concentration in the freestream. Additionally, shock impingement on the hot-film support structure introduced severe noise in the pressure signal. The probe's simplified shape allows for easy integration into an instrument rake. The inlet has a diameter of 0.086" (2.2 mm) and the probe has an overall frequency response of 2.5 kHz, but at the cost of uncertainty as high as 27% in molar fraction of helium. In Figure 5 below, the left drawing shows details of the sampling point geometry, with sharp edges and a divergent channel, and the right schematic shows a general layout of the probe and its sensors.

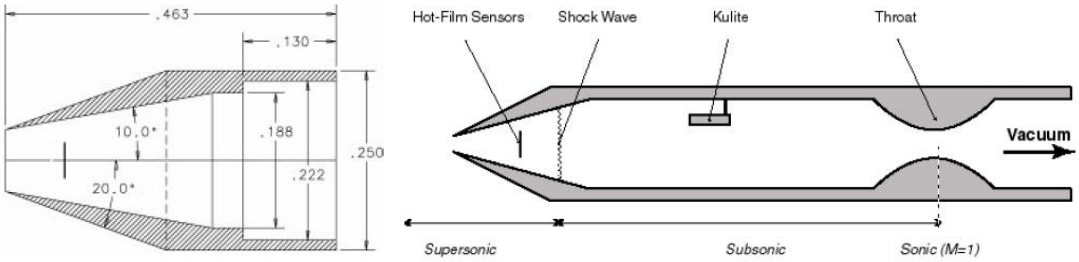

Figure 5: Xillo Probe[5]

In 2007, Maddalena[6] designed a probe similar to Ninneman and Ng, made specifically for near-wall measurements to study wall injectors. This probe was intended to operate in flowfields up to Mach 4, which was accomplished with a double divergent channel and more conservative inlet-to-throat area ratio. This ensured that the internal normal shock would occur far from the instrumentation, while avoiding liquefaction that occurs with unheated air around Mach 4.5. The throat is also replaceable, allowing inspection and replacement for impurities blocking the orifice, thus changing the throat area, altering the effective flowrate, and ruining the calibration. The probe integrates a type-K thermocouple which allows the probe to be used in

flowfields of different temperatures. The Maddalena probe has an inlet diameter of 0.025" (0.64 mm), a frequency response of 3 Hz, and a typical accuracy of 2%. A schematic of the probe's geometry is shown below.

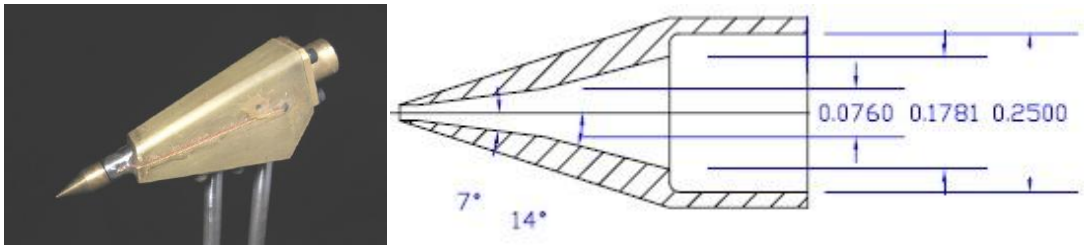

Figure 6: Maddalena Probe[6]

The interested reader is referred to the references for a more complete description of each design. The author's probe is based on the original supersonic design of Ng and Ninneman that builds on the concepts of each design discussed. Like Xillo's probe, it contains a subminiature pressure transducer. Like Ninneman and Ng's probe, it has a throat to inlet area ratio greater than unity, improving the frequency response. And like Maddalena's probe, it has an integrated thermocouple. An optimal probe design depends largely on the intended use, which must be taken case-by-case for a supersonic configuration. The present probe for use in UTA's supersonic wind tunnel was designed to operate under the flowfield conditions outlined in Section 1.1.

Chapter 2

Principle of Operation

The integrated sampling probe and gas analyzer determines gas composition by exploiting the difference in the thermodynamic properties of two species, with improved sensitivity from steeper differences. It will be demonstrated that for *binary* gas mixtures, the composition may be uniquely determined by using a hot-film with an anemometer and the measured thermodynamic state inside a plenum. Air and helium will induce different heat transfer rates, which is the primary indication for the concentration of each gas.

The idea to use an aspirating probe to measure gas composition was first conceived by Blackshear[7] in 1962, who built a water-cooled variant to measure heat flux, but also recognized its ability to measure concentration in isothermal binary mixtures. Instrumentation for this particular probe includes a hot-film, which is maintained at a constant temperature as heat is transferred to the local impinging mixture, while a thermocouple and subminiature pressure transducer measure stagnation properties in a downstream plenum.

The unknown mixture enters the probe and the flowrate is measured by the hot-film. The mixture also passes through a choked orifice which provides an independent flowrate measurement. The choked flowrate depends on P_t, T_t, and γ, and since $\dot{m}$ is independently measured from the hot-film, the only unknown is γ. Because air and helium have different thermodynamic properties, this allows X_{He} to be directly calculated.

The hot-film is maintained at a temperature well above the freestream with a constant-temperature anemometer (CTA). The CTA is an analog device with a feedback loop that drives an internal Wheatstone bridge towards balance. The hot-film circuit is one leg of that bridge, and the “hot” operating resistance is imposed with a control resistor on the opposite leg. Since the hot-film temperature is fixed, the heat transferred to the fluid is equal to the electrical power output, which is measured directly. Via calibration, the molar concentration of helium can be determined based on this CTA output voltage and measured stagnation conditions.

2.1 Probe Aerodynamics & Design Requirements

Figure 7 below shows a sketch of a concentration probe. A vacuum pump is attached to the throat downstream of the sampling point. Due to the induced pressure gradient from the vacuum pump, the bow shock will be swallowed inside the probe under the right conditions, to be discussed in Section 3.2. The flow is therefore subsonic across the sensing elements.

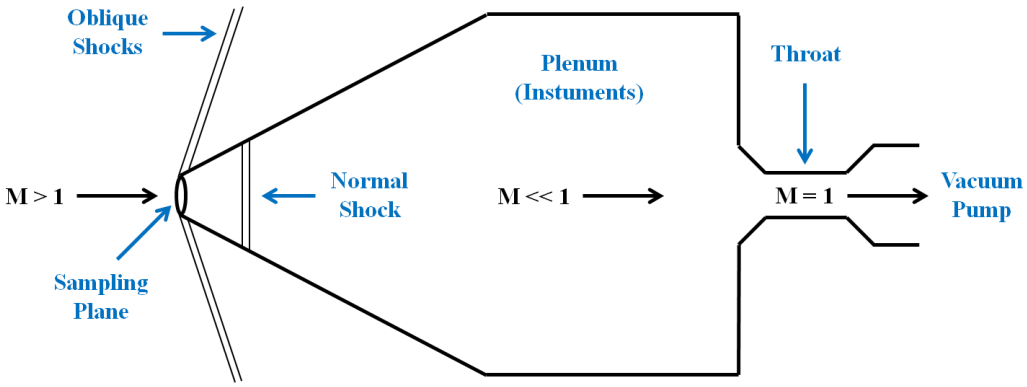

Figure 7: Probe Aerodynamics

The sampling inlet area is small to increase the probe's spatial resolution. The mixture enters the probe isokinetically, i.e. the Mach number at the inlet is the same as the freestream Mach number. The mixture is then supersonically expanded in a diverging channel until a normal shock occurs due to the mass flow constraint imposed by the throat. The mixture then expands subsonically to a Mach number << 1 in the plenum, where the mixture impinges on the hot-film and stagnation properties are measured. A vacuum pump downstream of the throat provides a sufficiently low backpressure to ensure that the throat is continuously choked. This probe can also operate in subsonic flow, the only difference being that the inlet is choked as well as the throats. This allows for calibration from a stagnant reservoir, rather than a costly calibration in a supersonic freestream.

Various requirements were imposed in the design phase, which are separated into four categories. The methods used to prove compliance are discussed in later chapters.

Aerodynamic requirements (for each Mach number up to 3):

- Moderate flow angularity does not inhibit isokinetic sampling
- The normal shock is swallowed, but does not contact the hot-film
- Air (oxygen) does not liquefy inside the probe
- Stagnation properties may be assumed in the plenum

Time response requirements:

- The time response is significantly improved from the previous design (300 ms)
- The steady-state particle flush time agrees with the analytical response time
- High-frequency (~100 kHz) fluctuations can be resolved

Geometric limitations:

- Deflection of the sampling inlet under supersonic forces is negligible
- Machining methods are feasible at this scale and complexity
- Construction is feasible using unskilled labor
- The vacuum line plumbing and wiring exit strategy are clean

Measurement accuracy requirements:

- Mean concentration accuracy is maintained or improved from previous designs

2.2 Mass Flow Measurement

Several methods exist which are capable of measuring massflow of a moving fluid. Thermal anemometry is most suited to the requirements for this probe, due to its fast frequency response and small size. Two types of anemometers exist: constant current anemometers (CCA) and constant temperature anemometers (CTA). The CTA was chosen due to its faster frequency response, better sensitivity to impinging fluids, and no risk of filament burnout from excessive current. Two types of sensors are available: hot-wires and hot-films. Hot-wires have a solid cross-section of a highly conductive, high strength metal (usually platinum) while hot-films have a thin film (usually platinum) deposited on a cylindrical glass or quartz substrate. Hot-wires

are very small (4 μm) and have an excellent frequency response (~200 kHz), while hot-films are larger (25 μm) and have a slower frequency response (~100 kHz). Responses of up to 1 MHz can be achieved with smaller wires and higher overheat ratios, but are not suitable not for this particular application; the frequency response will be discussed at length in Section 5.1. However, hot-films are much less fragile, less susceptible to particle impacts, and can withstand larger forces without strain due to the increased diameter. Due to the delicacy of potential repairs to the filament, the hot-film was selected while tolerating the slower response as a design trade-off. Many probe variants, such as Brown and Rebollo's, opted to draw a bare wire across an expanse, rather than using an off-the-shelf hot-wire system with included supports and body. Although this drastically reduces the overall sensor size, these systems are much less rugged and difficult to repair when compared to an off-the-shelf sensor with known properties. Due to their convenience and relatively low cost, a pre-fabricated sensor was used in this probe, at the minor expense of a larger size. The heat transfer measurement system thus consists of an off-the-shelf hot-film connected to a CTA.

The CTA is essentially a four-arm Wheatstone bridge with a feedback loop that maintains the operating resistance of the hot-film circuit. The output is a dynamically compensated voltage signal corresponding to the power required to maintain the filament at constant temperature. The active bridge arm consists of the hot-film in series with the wire leads and is balanced by a control resistor on the opposite arm of the bridge. In this way, the control resistor may be selected to impose a "hot" operating resistance of the hot-film. The overheat ratio is the ratio of the hot-film resistance at operating temperature to its resistance at ambient temperature. The overheat ratio is chosen to be as high as possible for improved sensitivity without damaging the filament itself, and a value of 1.56 was used for this probe. A schematic of the Wheatstone bridge and feedback loop is below:

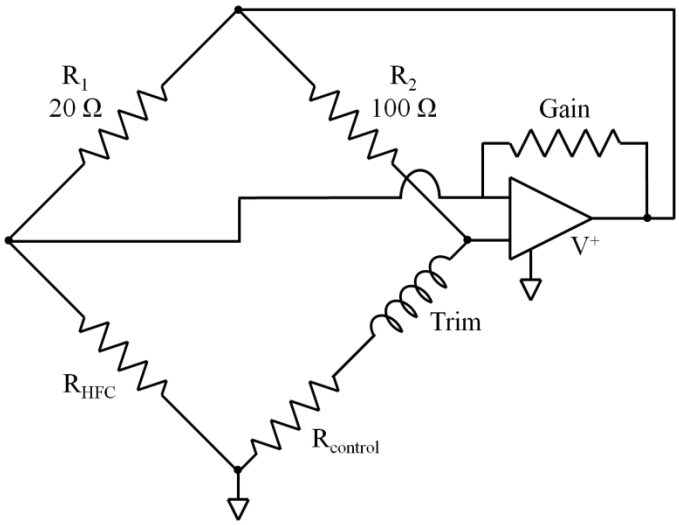

Figure 8: Wheatstone Bridge Diagram

In the schematic above, R_{HFC} is the combined resistance of the hot-film and wiring to the CTA and $R_{control}$ is the control resistance. This probe uses a TSI 1276-10A subminiature hot-film in conjunction with a TSI 1750A CTA. Specifications are below:

Table 1: Hot-film Specifications

Film	Diameter	25 μm
	Active sensing length	250 μm
Body	Diameter	0.9 mm
	Length	37 mm
Spec.	Max. operating temp.	250 °C
	Frequency response (measured)	~60 kHz
	Frequency response (typical)	100 kHz
	Material	Platinum

With this probe configuration, it was observed that the frequency response achieved a maximum of 60 kHz. The TSI 1750A CTA is an analog device with adjustable trim and gain settings, allowing for fine tuning of the response for a given probe circuit. A detailed analysis of the frequency characteristics of the hot-film and CTA system is presented in Section 6.1.

2.3 Pressure Measurement

One limiting factor of two previous designs[4,6] was pressure measurement. The use of hypodermic tubing to transfer the mixture to an external transducer is great for reducing the probe's size, but also introduces a considerable time lag. This lag may be reduced by decreasing the length of tubing or filling the tubing with grease, but the response is still slow and difficult to predict. Recent advancements in subminiature transducer technology make previous size constraints less stringent. Integration of a transducer inside the probe was chosen as a simpler solution to improve the frequency response.

This probe uses a subminiature Kulite XCQ-062-50A. It was chosen based on its small size, good accuracy, and excellent frequency response. Specifications are below:

Table 2: Pressure Transducer Specifications

Diameter	1.7 mm
Length	9.5 mm
Pressure range	0-50 psia
Operational range	-55° C to 120° C
Accuracy	0.50% FSO
Frequency response	60 kHz

Like most transducers, this model is strain-gauge based and uses a very thin silicon diaphragm. The frequency response is related to the diaphragm's natural frequency, which is unique for each pressure range. At this scale, the diaphragm has very little inertia and thus responds rapidly. The transducer is also temperature compensated via an external module. This compensation is particularly important for higher Mach number applications, where static temperatures can be quite low for unheated air. For the Mach 2.5 flow in this study, the nominal freestream static temperature is 133 K. A schematic of the transducer is shown in Figure 9:

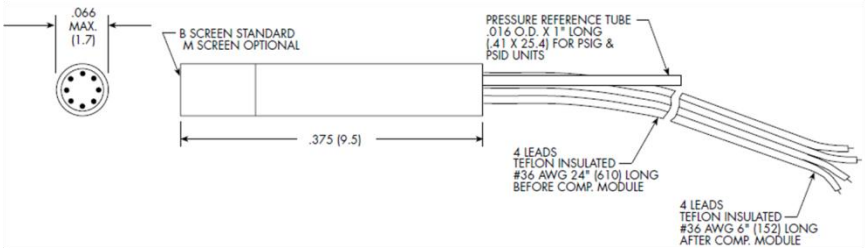

Figure 9: Kulite Pressure Transducer (source: www.kulite.com)

2.4 Temperature Measurement

Although it may seem easy, fast, reliable temperature measurements are difficult to obtain. Thermocouples are most commonly used, and can be very small and versatile, with the smaller and inexpensive models yielding a frequency response of ~1 kHz. Thermocouples at this physical size are fragile when exposed to vibrations or high-speed turbulent flow. Fortunately, conditions inside the plenum are low-speed, which enables the use of a very small sensing element. Previous work[4,5] has noted that total temperature inside the probe's plenum did not change significantly over the course of a single test, due to flow replenishment as the probe aspirates and short test durations. This trend was not observed for this test campaign, however, which will be discussed at length in Section 7.3.

The selected thermocouple is a fine-gage (13 μm) Omega CHAL-0005 Type-K with an accuracy of 0.75 °C. The frequency response is estimated at 1 ms and is empirically measured using heated air at 20 m/s by the manufacturer. Its actual frequency response will depend on the velocity and thermodynamic properties of the impinging medium inside the probe, and is estimated at 3 ms, to be described in detail in Section 5.2. The use of two hot-films operating at different overheat ratios (like Xillo's probe) is a good alternative temperature measurement scheme, but at the cost and complexity of an additional CTA. Although this yields temperature measurements on the order of the CTA (100 kHz), the *overall* response of the probe is

ultimately limited by its internal volume and flush time, to be discussed at length in Section 5.4. Thus, the additional cost and complexity could not be justified.

2.5 The Governing Equation

Dimensional analysis of the heated filament was originally performed by Brown and Rebollo[2]. Power output to the hot-film is calculated from the electrical signal, and equated to the heat transferred to the fluid since the hot-film is maintained at constant temperature. They verified that the backpressure was sufficiently low, static and total conditions were negligibly different in the hot-film's vicinity, and the species had the same total temperature and similar Prandtl number. A typical size of the sensing filaments is $\mathcal{O}(10^{-5}$ m), and at this scale the species may not behave as a fluid continuum. The Knudsen number, defined as a particle's mean free path λ divided by a characteristic length d (in this case, the filament diameter), is of $\mathcal{O}(0.1)$, but fortunately these effects and any other physical subtleties are accounted for by calibrating. Using the hot-film to develop the governing equation, they determined that the helium concentration is uniquely determined by correlating the Nusselt and Reynolds numbers.

$$Nu_d = f(X_{He}, Re_d) \tag{2.1}$$

Dimensional analysis provides insight into the dominant parameters that model the instrument's response. Calibration was performed to correlate the probe's voltage, total pressure, and molar concentration of helium. In supersonic flow, stagnation conditions can have significant spatial and temporal variations in the flowfield. For choked, steady-state flow, the mass flux over the hot-film can be written as:

$$\rho u = \frac{P_t C^* A^*}{\sqrt{T_t} A_C} \tag{2.2}$$

C* denotes the sonic fluid function, which is constant for a calorically perfect mixture of fixed composition and is defined as:

$$C^* = \sqrt{\frac{\gamma}{R}} \left(\frac{2}{\gamma + 1} \right)^{\frac{\gamma+1}{2(\gamma-1)}} \tag{2.3}$$

This mass flux formulation is a convenient expression using stagnation conditions, the sonic fluid function, and the area ratio. The Reynolds number is expressed using the hot-film diameter as the reference length:

$$Re_d = \frac{\rho u d}{\mu} = \frac{P_t C^*}{\sqrt{T_t}} \frac{A^*}{A_C} \frac{d}{\mu} \tag{2.4}$$

The CTA output voltage is proportional to the heat transferred from the heated filament to the mixture. Because each resistance is maintained constant, the electrical power output across the filament may be written as:

$$\dot{Q}_f = I_f^2 R_f = \left(\frac{V}{R_f + R_s} \right)^2 R_f \tag{2.5}$$

R_f is the hot-film operating resistance and R_s is the lead and cable resistance in series with the hot-film. The heat transferred to the fluid is expressed as:

$$\dot{Q}_f = hA\left(T_f - T_t\right) = Nu_d \pi k l \left(T_f - T_t\right) \tag{2.6}$$

'*l*' is the active sensing length of the hot-film. The *total* temperature is used in (2.6) because total and static properties in the vicinity of the hot-film are negligibly different. Because the hot-film temperature is constant, the two heat transfer rates are equal. Re-writing in terms of the Nusselt number yields:

$$Nu_d = \frac{V^2 R_f}{\pi k l \left(T_f - T_t\right)\left(R_f + R_s\right)^2} \tag{2.7}$$

An experimental survey by Devillers and Diep[8] determined that the most appropriate correlation for air and helium mixtures is a power law with the Nusselt number expressed in terms of the Reynolds number, rather than the well-known King's Law:

$$Nu_d = a(Re_d)^b \tag{2.8}$$

Similarly, forced convection theory for cross-flow over a semi-infinite cylinder predicts the average Nusselt number over the film's surface for laminar flow as:

$$Nu_{d,avg} = 0.593 Re_d^{1/2} Pr^{1/3} \tag{2.9}$$

The power law correlation is the more general approach, where both a and b are functions of the helium concentration only. These constants a and b must be determined from calibration. Expanding (2.8) and solving for the CTA voltage yields:

$$V^2 = \frac{\left(R_f + R_s\right)^2}{R_f} \pi k l a \left(\frac{P_t C^* A^*}{\sqrt{T_t} A_C} \frac{d}{\mu}\right)^b \left(T_f - T_t\right) \tag{2.10}$$

This is the final governing equation for the hot-film using the sensor outputs. Many of the parameters do not change over the course of an experiment:

$$\left(R_f, R_s, l, d, A^*, A_C, T_f\right) = const. \tag{2.11}$$

When evaluated at measured stagnation conditions, several parameters are unique functions of the helium concentration:

$$(k, C^*, \mu, a, b) = f(X_{He}) \tag{2.12}$$

The helium concentration is implicitly included in (2.10), and with the considerations from (2.11) and (2.12), the governing equation reduces to a simple functional form:

$$X_{He} = f(P_t, T_t, V) \tag{2.13}$$

The helium concentration is therefore uniquely determined by stagnation conditions inside the probe's plenum and the CTA voltage.

Chapter 3

Final Design

This final design was produced after many iterations, and builds on design concepts from previous probes. A description of the design is presented, compliance with the design requirements is demonstrated, and then construction and implementation are discussed.

3.1 General Arrangement of the Probe

The probe consists of four interlocking brass parts. A removable cap was designed with particular internal and external geometry to achieve the desired aerodynamic effects. Two small throats were machined into a holder which also secured each sensor in place. Two barb fittings at the exit evacuate the mixture via flexible tubing to the vacuum pump. The sensor wires exit the holder from the rear through clearance holes. Assembly of the machined parts and sensors was accomplished with a combination of adhesives and press fitting. All sensing elements are inside the cap, with the rest of the probe body designed to house the sensors and channel the mixture downstream to the vacuum pump. An instrument rake was designed simultaneously to house up to two probes as part of UTA's new two-dimensional traversing system for supersonic testing. A CAD model of the probe's exterior is shown below.

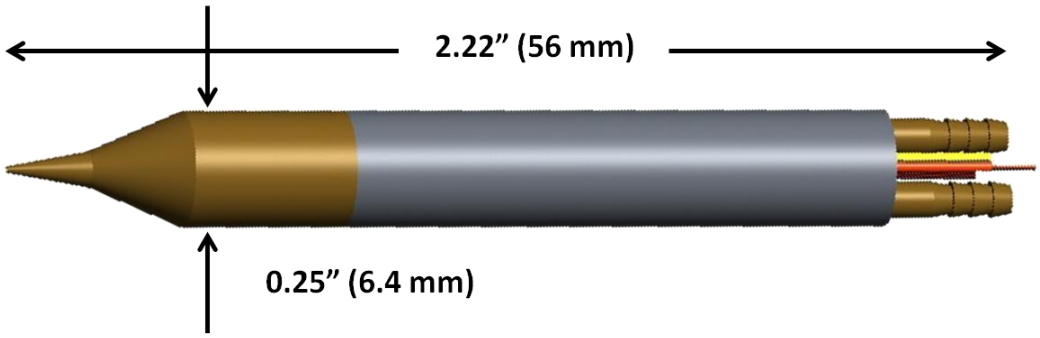

Figure 10: CAD Model of Probe Exterior

The hot-film consists of a thin filament attached to a long stainless steel housing via small insulated supports. The cap was designed to tightly enclose the hot-film sensor. This was

done for two reasons; first, reducing the cross-sectional area at the hot-film sensor plane results in a higher impinging velocity and therefore improved sensitivity. Second, positioning the hot-film close to the inlet decreases the mixture's residence time before impingement and thus the negative effects of internal probe mixing. The CAD model below shows the orientation of the hot-film with respect to the cap.

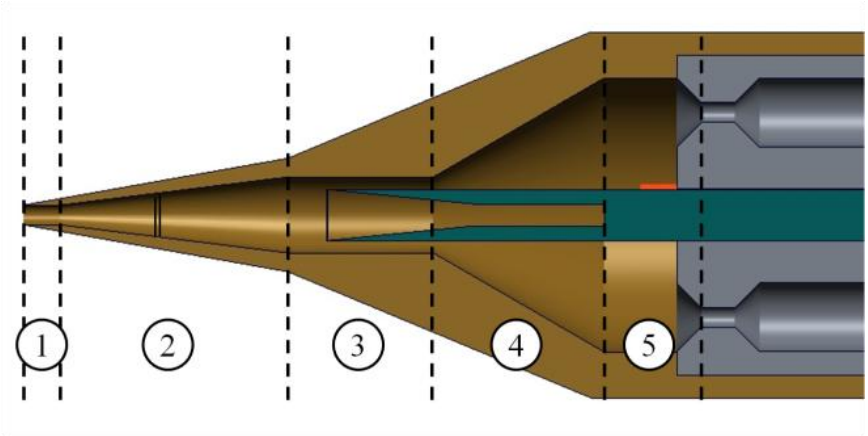

Figure 11: Cap's Aerodynamic Layout

The inlet area was machined as small as possible within practical limits, to a diameter of 0.0135" (0.343 mm) for improved spatial resolution. The cap geometry consists of 5 sections. Section 1 is a short, straight inlet that helps accommodate moderate flow angularity. Section 2 is a 7° divergent channel, designed to prevent boundary layer separation, which expands the mixture supersonically until a normal shock occurs, after which the mixture expands subsonically. Section 3 is a straight channel that encloses the hot-film, with a short length of 0.10" to account for minor positioning errors. Section 4 is a 30° divergent channel expanding up to the main plenum. Section 5 is a short straight channel which is designated as the main plenum, where stagnation properties are measured with the pressure transducer and thermocouple. The CAD model below shows the orientation of all the instruments with respect to the cap and holder.

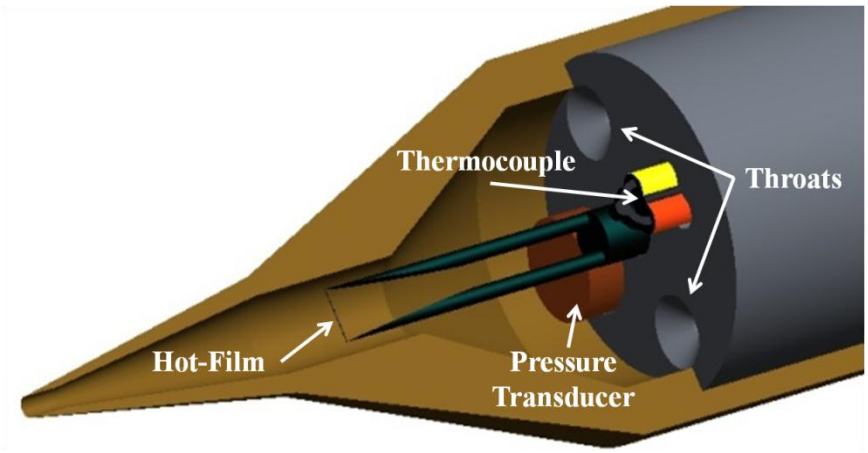

Figure 12: Instrument Location inside Cap

The volume inside the cap was minimized, providing sufficient space for the sensors themselves. This minimization was done to increase the frequency response of the overall probe, to be described in detail in Section 5.3. Downstream of the throats, the first segment of the vacuum line is built directly into the holder. The probe's specific aerodynamic configuration is shown below:

Figure 13: Aerodynamic Configuration & Vacuum Line

The mixture is choked through *2 symmetrical throats*, and then channeled downstream to two flexible tubes, connected with barb fittings. The purpose of two throats instead of one was for better flow symmetry through the plenum. The barb fittings are press fitted with a thin epoxy layer for a tight seal. The overall length of the holder, and therefore the probe itself, is imposed by the length of the hot-film's stainless steel body. The diameter of the probe was chosen to match previous designs, while also minimizing the cross-sectional area to reduce blockage in the relatively small wind tunnel test section.

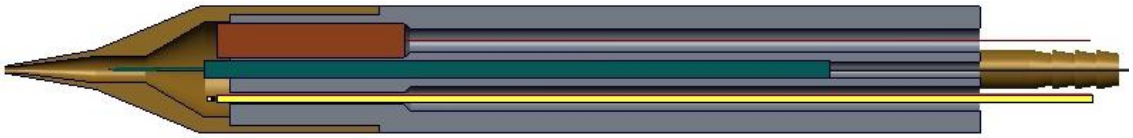

Figure 14: Instrument Plane Cross-Section

As seen in Figure 14 above, the plenum diameter was minimized to tightly fit around the relatively large pressure transducer (pictured on top). The transducer and the hot-film each have a lip inside their respective channel for easy depth positioning inside the holder, and the thermocouple depth is manually positioned to match the transducer. A thin epoxy layer is applied to each instrument before being placed in the holder, securing each from movement and creating a tight seal. Major dimensions of the probe's geometry are presented below:

Table 3: Bulk Probe Geometry

Overall dimensions		Internal areas		
Overall length	2.22"	Inlet area	ϕ = 0.0135"	143 x 10^{-6} in^2
Outer diameter	ϕ = 0.25"	Hot-film area	ϕ = 0.0520"	2124 x 10^{-6} in^2
Inlet to throat distance	0.449"	Plenum area	ϕ = 0.1875"	31400 x 10^{-6} in^2
Inlet to throat volume	0.003206 in^3	Throat area	2 x ϕ = 0.0135"	286 x 10^{-6} in^2

Technical drawings of the CAD model are presented in Appendix B. The image below shows the probe mid-assembly with a size reference.

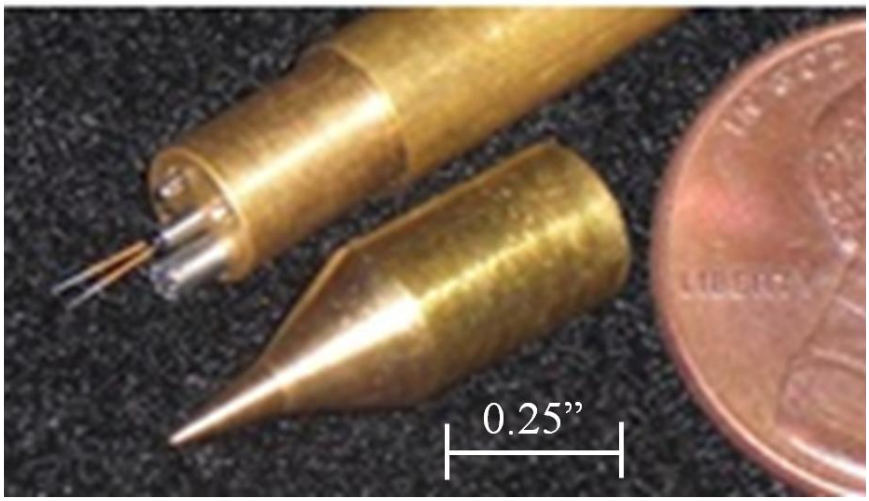

Figure 15: Scaled Image of Probe

3.2 Compliance with Aerodynamic Constraints

All aerodynamic requirements outlined in Section 2.1 were satisfied for the final design, and the methods used to demonstrate compliance are presented in this section. Prevention of a standoff shock is important to ensure isokinetic sampling. Analysis parameters are the cone half-angle θ_c, freestream Mach number M_∞, and specific heat ratio γ. A perfectly sharp leading edge is realistically unmachinable, and local standoff shocks will always occur for blunt surfaces in supersonic flow. This effect is reduced as the vacuum pump induces a low backpressure that sucks the mixture inside the probe. The analysis below initially assumes that the leading edge is perfectly sharp and local standoff shocks do not occur.

For conical flow, pathlines downstream of the oblique shock curve smoothly until becoming parallel with the cone’s surface. Taylor-Maccoll numerical analysis is used to calculate the maximum cone half-angle for which the oblique shock remains attached. The technique initially guesses the shock angle, calculates the post-shock velocity, numerically integrates the Taylor-Maccoll differential equation until the tangential velocity component is zero, and iterates the guessed shock angle until the velocity direction matches the cone half-

angle θ. Bow shocks at the leading edge need to be prevented for the expected ranges for wind tunnel testing, and Figure 16 illustrates the actual (exaggerated) and ideal geometry:

$$1.8 < M_\infty < 2.8 \quad and \quad 1.40\ (Air) < \gamma < 1.667\ (Helium)$$

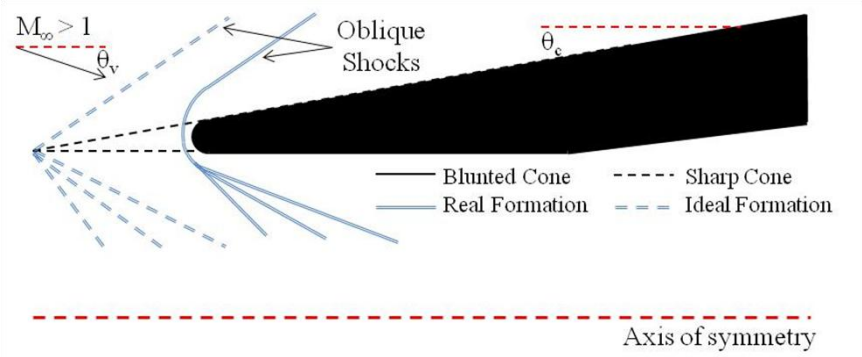

Figure 16: Blunt and Sharp Leading Edge Shock Formations

The sketch illustrates the effects of a blunt leading edge for a cone in supersonic flow. For a perfectly sharp cone with no flow angularity, an oblique shock forms on the upper surface and a Mach line on the lower surface. In the real case, local normal shocks will occur, which makes the shock more difficult to swallow. A sharper leading edge makes the normal shock easier to swallow. The maximum cone half-angle θ_c for attached oblique shocks increases with Mach number, and the worst-case is for helium at Mach 1.8 where shock detachment occurs at 33.9°. This result is not conservative, and calculation of an actual maximum is impossible due to the effect of local blunt surfaces at the leading edge. The freestream can also have moderate flow angularity, particularly when sampling close to the fuel injector. This imposes further restrictions on θ_c by increasing the *effective* cone half angle, defined as $\theta_{eff} = \theta_c + \theta_V$. A maximum flow angularity of 10° is expected for these experimental surveys. With a perfectly sharp leading edge, this limits θ_c to 23.9°. Ng and Ninneman[4] experimentally determined the angular sensitivity of their probe, and found that for 15° flow angularity, the resulting error in X_{He} was less than 2.5%. Schlieren photography and pressure comparisons will ultimately be used to determine to what extent the shock is actually swallowed, and therefore the validity of the

isokinetic sampling assumption. Because the mixture expands supersonically after entering the probe, the normal shock in the divergent channel is stronger than a normal shock occurring at the freestream Mach number. Therefore a larger total pressure loss is expected inside the probe, and comparison with a pitot tube measurement at the same point will indicate shock swallowing.

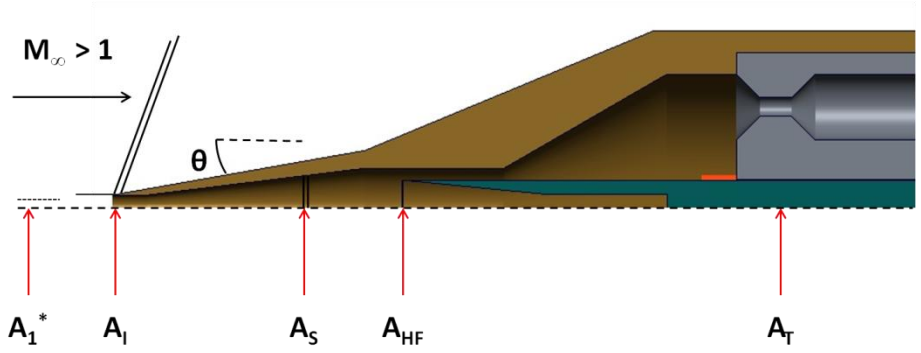

Figure 17: Mach Number and Shock Locator

The following model provides both the Mach number everywhere inside the probe as well as the location of the normal shock. Appropriate aerodynamics equations are taken from Anderson[9]. It is assumed that:

- A stream tube equal in size to the inlet area enters the probe undisturbed
- Expansion in the divergent section is isentropic, both pre-shock and post-shock
- The flow is choked at both of the throat areas

With the assumption that the shock is swallowed due to the backpressure from the vacuum pump, the first goal is to ensure that $A_i < A_S < A_{HF}$, i.e. the shock does not impinge on the hot-film. With the freestream Mach number known, the area-Mach relation is written for the inlet and freestream, using a virtual nozzle area A_1^*.

$$\left(\frac{A_i}{A_1^*}\right)^2 = \frac{1}{M_\infty^2}\left[\frac{2}{\gamma+1}\left(1+\frac{\gamma-1}{2}M_\infty^2\right)\right]^{\frac{\gamma+1}{\gamma-1}} \tag{3.1}$$

This equation can be solved for A_1*. For steady-state flow of a constant composition and fixed total temperature, continuity yields the following equation which relates the throat area and virtual nozzle area:

$$\dot{m}_1 = \dot{m}_1 \Rightarrow \frac{P_{t,1} C_1^* A_1^*}{\sqrt{T_{t,1}}} = \frac{P_{t,2} C_2^* A_t}{\sqrt{T_{t,1}}} \Rightarrow P_{t,1} A_1^* = P_{t,2} A_t \tag{3.2}$$

The throat area is fixed and A_1* is known, so the total pressure ratio is calculated directly. Due to losses across the normal shock, internal pressure is substantially less than the freestream total pressure. A total pressure loss of up to 71% is expected at Mach 2.8 without considering skin friction drag. The calculated total pressure ratio corresponds to some normal shock strength, and using normal shock relations, the Mach numbers upstream and downstream of the shock may be calculated. The area-Mach relation is then written for the shock plane area and the virtual nozzle area, using the pre-shock Mach number M_s:

$$\left(\frac{A_s}{A_1^*}\right)^2 = \frac{1}{M_S^2}\left[\frac{2}{\gamma+1}\left(1 + \frac{\gamma-1}{2} M_S^2\right)\right]^{\frac{\gamma+1}{\gamma-1}} \tag{3.3}$$

This equation yields the area at the shock plane, which can be used to find the shock distance from the leading edge from the probe geometry. This process was repeated over a range of freestream Mach numbers and specific heat ratios (for different gases) to find the worst case scenario where the shock propagates furthest downstream. To satisfy the design requirement, the hot-film plane area must be larger than the shock area.

Air liquefaction, specifically oxygen, can occur from overexpansion at high Mach numbers in unheated flow, so prevention is necessary to ensure that liquid oxygen, a very powerful oxidizing agent, is not formed and does not damage the instruments (or ruin the calibration). The shock plane area is known for each scenario, so the Mach number just upstream of the shock is found using the 1-dimensional area-Mach relation. Helium can safely be expanded to very high Mach numbers without risk. Oxygen liquefies around 90 K at atmospheric pressure, and so for T_t ~ 300 K, this imposes an upper limit of Mach 3.4.

The Mach number is now known at every point inside the probe. However, the plenum is very close to the throats, and this 1-dimensional analysis becomes invalid due to the abrupt change in area. Stagnation and static properties should be less than 1% apart to neglect this difference and validate the assumption.

$$1 \geq \frac{P_t}{P} = \left[1 + \frac{\gamma - 1}{2} M^2\right]^{\frac{\gamma}{\gamma - 1}} \geq 0.99 \tag{3.4}$$

This constraint must be satisfied to reasonably assume that stagnation properties are being measured at the sensor plane. Chamfering around both throats straightens the flow in their proximity. The Mach number may be calculated for the chamfered area using 1-dimensional analysis. A summary of the aerodynamic requirements and worst-case compliance is below.

Table 4: Aerodynamic Design Requirements

Parameter	Air	Helium	Requirement
A_{HF}/A_S	10.6	11.7	>> 1
θ_c	10°	10°	<< 23.9°
M_{max}	3.16	3.18	< 3.4
$(P/P_t)_{cutout}$	99.8%	99.8%	> 99%

The normal shock occurs at an area which is 9.4% of the hot-film plane, which ensures that the shock will never approach the hot-film. The probe's leading edge has a half angle of 10°, which is much less than the non-conservative maximum of 23.9°. Schlieren imaging will verify this design intention. This value was reduced as a tradeoff with instrument fragility and machining limitations. Liquefaction will not occur inside the probe, as the maximum Mach number is less than 3.4 for all cases for air. The pressure ratio at the chamfered cutouts is higher than 99%, and so the pressure ratio in the larger *plenum* will be much higher.

3.3 Construction and Implementation

Construction and implementation proved to serious obstacles in obtaining good results, specifically in maintaining a good vacuum line. The biggest design challenge was to use the limited space available to fit each instrument, while safeguarding wires and maintaining the choked condition at the throats. The small size of the probe, coupled with the geometrical constraints of the tunnel's test section and the traversing system, required the use of small $^{1}/_{16}$" ID flexible Tygon® tubing for a large portion of the vacuum line. For the probe to function properly, the throats must be continuously choked, and the vacuum pump (or pumps) had *constant* difficulties maintaining this condition. The line consisted of a short $^{3}/_{64}$" channel through the probe body, 27" of $^{1}/_{16}$" tubing out the test section, and finally 78" of ¼" tubing that connected to a vacuum pump on the floor. Each length of flexible tubing was minimized to reduce the load on the vacuum pump. However, this length reduction combined with vigorous leak prevention was not sufficient to ensure that *both* throats were continuously choked. This is for two main reasons: first, helium has a very low molecular weight and will always leak regardless of preventative measures, and a leak in the vacuum line on the order of the inlet diameter (0.34 mm) could easily disrupt the choked condition at the throats. Second, L/D for this vacuum line is around 800, and pressure losses are significant after considering skin friction drag. To resolve this issue, one of the throats in the plenum was closed off with epoxy, and no further issues were experienced. Removing the downstream manifold reduced the load on the vacuum pump. The cost of this modification is an increase in the response time.

The probe geometry was designed in close collaboration with the machine shop, due to the small size and tight constraints. Drill depths were limited for narrow, long bores due to drill bit bending. Brass was selected primarily for machinability and sufficient strength, since FEM predicted only minor structural stresses. A shallow flat was milled into one side of the holder to ensure proper angular alignment of the instruments in the holder. Although each part was small,

the probe was fully machined using conventional machining methods, avoiding the added cost of CNC, EDM, or 3-dimensional printing techniques.

These fragile instruments required careful handling during construction. The probe was designed such that unskilled labor was used rather than outsourcing to a third party. Hot-film alignment with the tight cap clearance was the biggest concern. Another issue was how to affix each instrument to the holder without blocking the throat. The construction procedure was re-iterated several times for predicted difficulties.

- Calibrate the probe's thermocouple before beginning assembly
- Clamp the holder in a vice and cover the throats with tape
- Channel all instrument wires through the holder
- Apply epoxy to each instrument and slide into the holder
- Remove excess epoxy and allow it to set
- Partially slide each barb fitting into the back slots
- Apply epoxy to the holder surface that overlaps the cap, and slide the cap on while maintaining proper alignment using a V-shaped channel
- Attach the cap cover and tap with a mallet to press fit all four parts together
- Verify the hot-film is electrically insulated by measuring the circuit resistance
- Apply epoxy to the back of the holder, creating a secondary wire seal

Figure 18 shows images taken during construction and implementation:

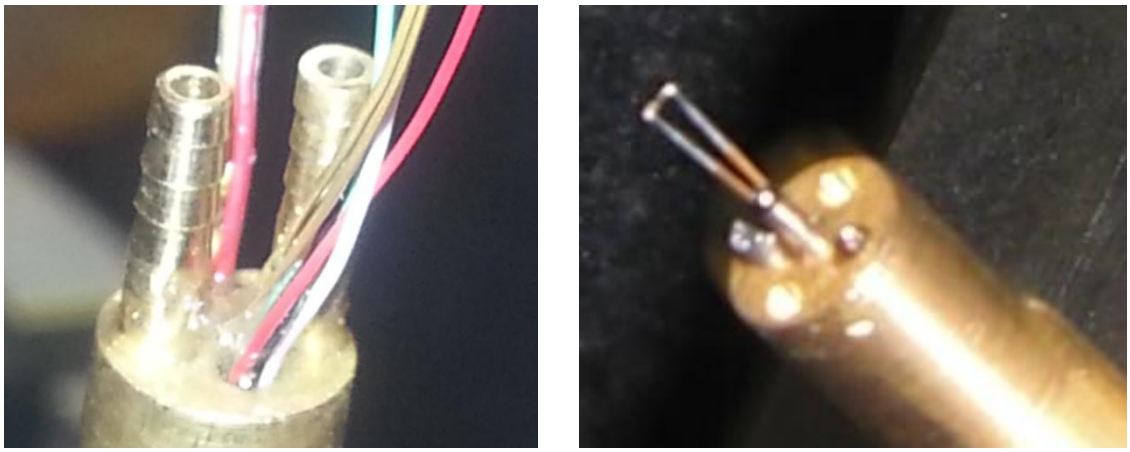

Figure 18: Probe Assembly Snapshots

Figure 19: Zoom in of Physical Probe

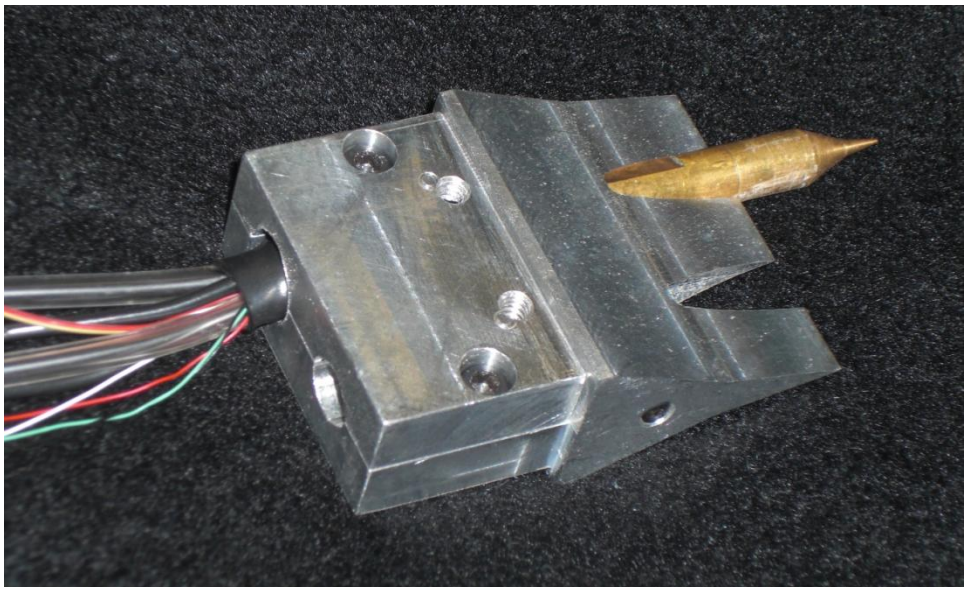

Figure 20: Probe Mounted in Instrument Rake

Chapter 4

Data Acquisition and Calibration

4.1 Data Acquisition System

Data was acquired using an NI PCI-6024E DAQ which has a 200 kS/s sampling rate, 12-bit A/D converter, and eight differential analog input channels. Inputs were wired to a SCB-68 connector block. A LabView VI (virtual instrument) was created by the author to record the probe's output over the course of each test and also control the ratio of helium and air. The probe output may be observed while calibrating to record data at target points and also note any discrepancies. Two screenshots of the partial interface are shown below:

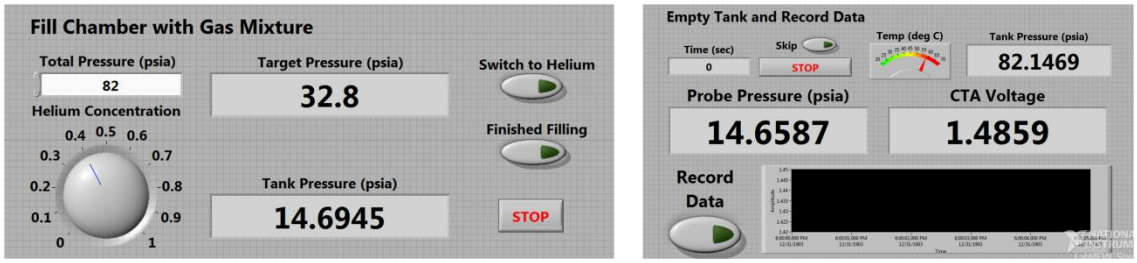

Figure 21: LabView Calibration VI Interface

4.2 Calibration

The CTA voltage is the dependent variable for calibration. X_{He} and P_t are imposed in a controlled environment over a range of expected pressures and helium concentrations in the flowfield. A calibration tank was built for this purpose, where helium concentration may be directly imposed by the partial pressures of air and helium in the tank:

$$X_{He} = \frac{P_{He}}{P_{He} + P_{air}} \tag{4.1}$$

Particular care was taken to minimize leaks in this setup, preserving the initially imposed helium concentration for the duration of each test. With a known mixture, the probe samples directly from the tank while the data acquisition system records the CTA voltage, total pressure, and total temperature. A support facility was designed and assembled to perform

probe calibrations. A 380 in^3 (6,200 cc) aluminum pressure vessel encloses the binary gas mixture. The tank pressure was monitored by an Omega PX-429-150GV5 transducer, which is temperature compensated from -29 °C to 85 °C with an accuracy of ±0.08%. Air and helium bottles were connected to the tank with separate valves. A manual relief valve was installed to expedite the emptying process between target pressures. A Hyvac 2-45 vacuum pump was used to empty the tank of residual gases between mixtures, and a separate vacuum pump of the same model was used to provide low backpressure to the probe's throat. A 24VDC computer fan was installed inside the tank to enhance mixing. The probe samples from the tank via 5 cm of $^1/_4$" ID flexible Tygon® tubing and was firmly clamped to minimize spillage. $^1/_{16}$" ID flexible Tygon® tubing connected the probe's throats to an adaptor, which manifolded the two throats and then connected to the vacuum pump via $^1/_4$" ID flexible Tygon® tubing. A picture of the calibration setup is shown in Figure 22:

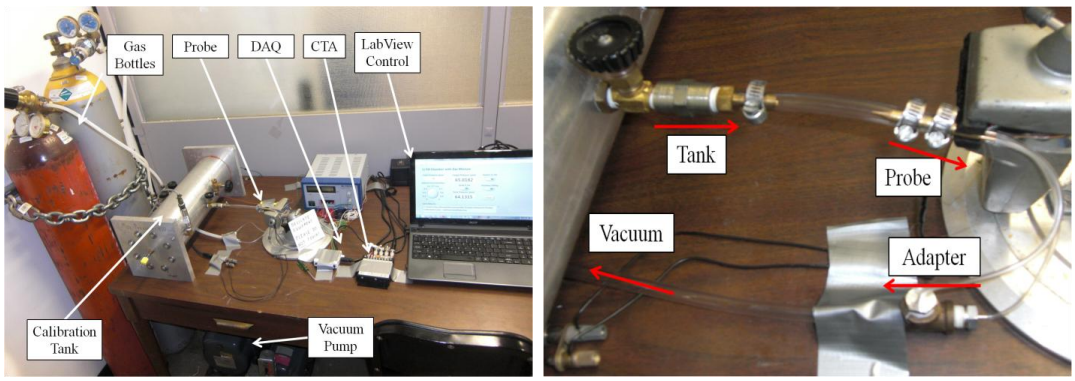

Figure 22: Calibration Facility

Using this setup, the following procedure was employed to calibrate the probe:

- Close all valves and run the Labview VI
- Evacuate the tank of residual gases using the first vacuum pump
- Fill the tank with air and helium to the desired helium concentration
- Turn on the CTA, mixing fan, and probe's pressure transducer

- Wait 60 seconds for the fan to mix the gases together
- Turn on the second vacuum pump
- Open the probe valve to begin sampling from the tank
- At specified target pressures, manually trigger data recording using the VI
- Use the relief valve to expedite the emptying process between target pressures
- Turn off all power supplies and vent the tank contents to the atmosphere
- Repeat for the full range of helium concentrations

Relieving the tank pressure between target pressure values has two purposes; first, the probe evacuates the tank very slowly, so expedited evacuation decreases the mixture residence time in the tank, decreasing the inevitable effect of helium leaks and preserving the accuracy of the nominal helium concentration. Second, venting the mixture to the atmosphere causes further mixing due to the induced motion, reducing the possibility of stratification inside the tank.

The array of target pressures was selected based on expected tunnel freestream conditions. For the conservative Mach envelope of $1.8 < M_\infty < 2.8$ and any combination of air and helium, it was found that the pressure inside the probe would be bound between 20 and 60 psia. This prediction was later confirmed during wind tunnel testing. Additionally, calibrating at lower pressures can potentially contaminate the calibration curves, because sub-atmospheric pressures in the calibration tank potentially allows ambient air into the system, corrupting X_{He}.

Final calibration results are shown in Figure 23 below. Both P vs. V and Nu vs. Re plots are shown, as well as a table of calibration constants. A MatLab script is given in Appendix A which was used to reduce the raw data, generate these curves, and determine the calibration constants. A least-squares curve fitting technique is used to fit a power law to the data, as it best represents air and helium mixtures based on previous observations[8]. The coefficients in Figure 23 quantify the relation $\mathrm{Nu_d} = \mathrm{a}(\mathrm{Re_d})^{\mathrm{b}}$ for each helium concentration.

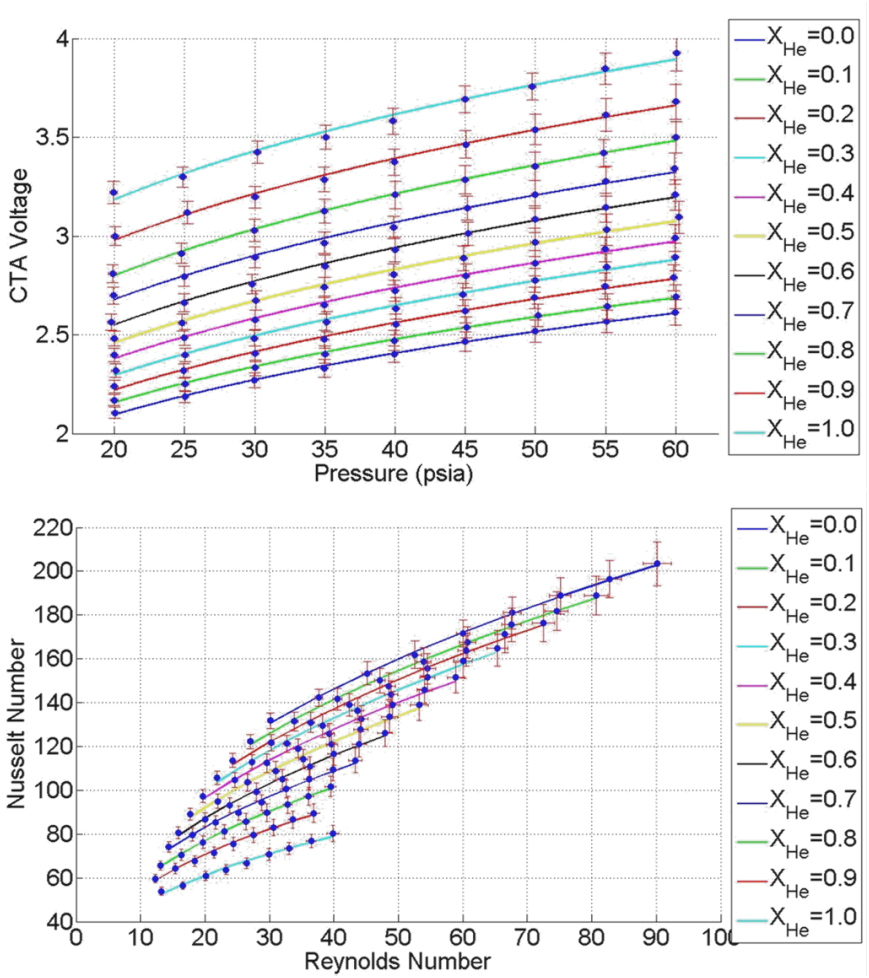

X_{He}	0	0.1	0.2	0.3	0.4	0.5	0.6	0.7	0.8	0.9	1
a	33.3	32.0	29.9	28.8	28.6	27.1	25.4	25.7	23.4	22.9	20.3
b	0.402	0.403	0.413	0.415	0.406	0.409	0.412	0.392	0.397	0.376	0.368

Figure 23: Final Calibration Output

Error bars are plotted from random fluctuations with a 95% confidence interval. Fluctuations in the CTA voltage are caused by changes in the *local* helium concentration impinging on the hot-film, signal compensation, and turbulence. For calibration, the CTA output was averaged over ~2000 data points per target pressure, and voltage fluctuations are not considered to be a source of error in the uncertainty analysis. It was observed over the course

of several calibrations that the total temperature inside the probe's plenum changed negligibly while the probe aspirated, which has indeed been observed by other investigators as well[2,4].

4.3 Determination of the Calibration Constants

Helium concentration is determined using standard linear interpolation techniques. A given data point of [P_t, Tt, V] is measured during an experiment, which corresponds to *exactly one* helium concentration. First, the viscosity and thermal conductivity of air and helium are calculated separately based on the temperature using empirical curve fits from Fuller[10] and Wilke[11]. Pressure dependence is negligible for the observed ranges of these experiments. Then, composite gas equations for the mixture's thermodynamic properties from Burgers[12] are used for every concentration in the calibration file, usually X_{He} = [0, 0.1, 0.2, ..., 1.0]. The Nusselt and Reynolds numbers are then calculated for each concentration, based on the values of [P_t, Tt, and V]. With the Reynolds number calculated, the expected Nusselt number for each particular concentration is calculated using $\mathrm{Nu_d} = \mathrm{a}(\mathrm{Re_d})^{\mathrm{b}}$. A computer routine then finds the upper and lower bounding concentration curves from the Nu vs. Re calibration plot and linearly interpolates to calculate the concentration of that data point. This is repeated for every data point in the file, and a routine then generates a contour plot of the 1-dimensional or 2-dimensional concentration map, as well as other statistical analysis. A MatLab script is presented in Appendix A.

4.4 Uncertainty Analysis

There are three main sources of error for this probe; deviation of individual data clusters from the calibration curve fits, fixed instrument error, and random error from noise and fluctuations. To quantify the errors introduced from imposing curve fits on the raw calibration data, an interpolation technique is used, shown graphically below:

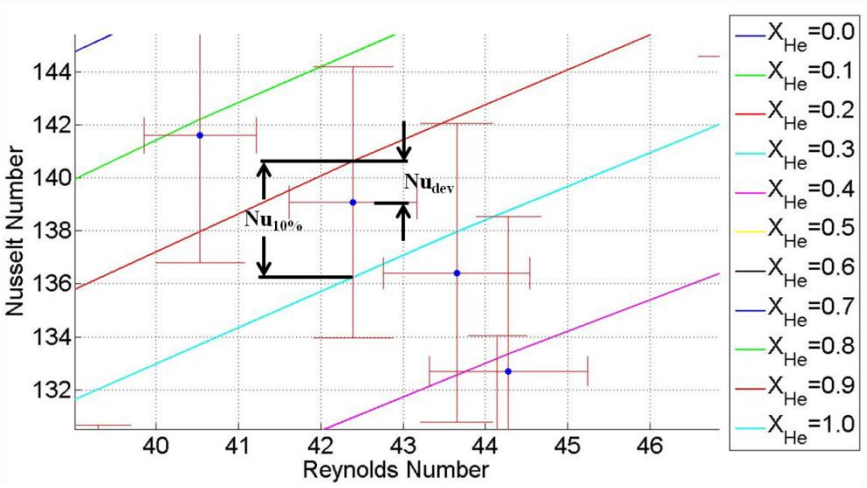

Figure 24: Perturbation Method

A numerical technique calculates the values of Nu_{dev} and $Nu_{10\%}$ for each cluster. $Nu_{10\%}$ is the local Nusselt number difference at the given Reynolds number between the two bounding concentration curves. Clearly the deviation varies point-by-point. This deviation is significantly higher for Nu vs. Re plots as opposed to P vs. V plots, because $Nu \sim V^2$ and thus voltage deviations are *amplified* on the Nu-Re plots. Extrapolation is performed for points at the extremities for which there is only one curve. The deviation of each cluster from the nominal curve is then given by:

$$\% \, Error(X_{He}) = (10\%) \frac{Nu_{dev}}{Nu_{10\%}} \tag{4.2}$$

Because X_{He} is implicitly included in the governing equation, a perturbation method is used to quantify concentration error due to errors in each instrument's measurement. The method is presented in Doebelin[13] as the root-sum-square method, which quantifies the uncertainty in X_{He} as:

$$U_{X_{He}} = \pm \sqrt{\left(\frac{\partial X_{He}}{\partial V} U_{\mathrm{V}}\right)^2 + \left(\frac{\partial X_{He}}{\partial T} U_T\right)^2 + \left(\frac{\partial X_{He}}{\partial P} U_{\mathrm{P}}\right)^2} \tag{4.3}$$

Each partial derivative is the sensitivity of X_{He} to the respective independent parameter, where U_x is the uncertainty of the parameter 'x'. Similarly to the calibration uncertainty, these sensitivities will change point-by-point as the nominal conditions change. Rather than calculating these partial derivatives by hand, a simpler approach is the numerical MatLab function that was built to reduce mean concentration data from the SSWT. Small perturbations of P, T, and V at different nominal conditions yield the sensitivities directly.

Fixed error is provided for the thermocouple and pressure transducer by the manufacturer, and is not applicable to the CTA voltage. Errors in the 12-bit A/D conversion from the DAQ are small and thus neglected. To recapitulate from the instrumentation descriptions in Section 2.3 and 2.4, the thermocouple has an accuracy of 0.75 °C, and the pressure transducer has an accuracy of 0.5% FSO, or 0.25 psia.

Random CTA voltage error is neglected, as fluctuations can be attributed to different *local* mixtures impinging on the hot-film and turbulence. The pressure and temperature fluctuations are considered a source of random error, and a 95% confidence interval is taken to quantify this uncertainty. Combining all of these errors, and assuming no uncertainty in the CTA voltage, the error in X_{He} is:

$$U_{X_{He}} = (10\%)\frac{Nu_{dev}}{Nu_{10\%}} + \sqrt{\left(\frac{\partial X_{He}}{\partial T}U_T\right)^2 + \left(\frac{\partial X_{He}}{\partial P}U_{\mathrm{P}}\right)^2} \qquad (4.4)$$

U_x is the combined fixed and random error for each measurement 'x'. Plots are shown below for nominal calibration error, combined instrument error, and total error.

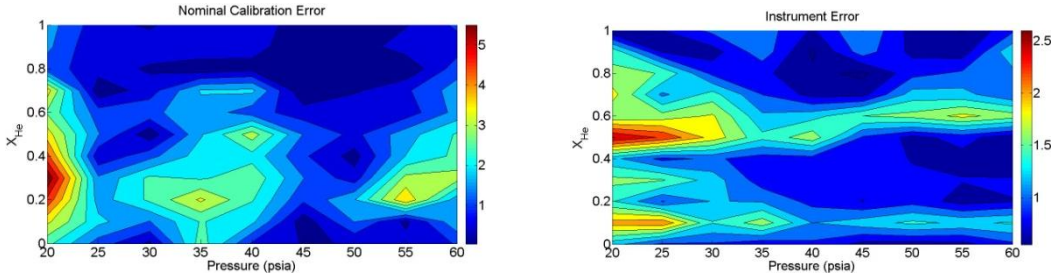

Figure 25: Calibration Error (Left) and Instrument Error (Right)

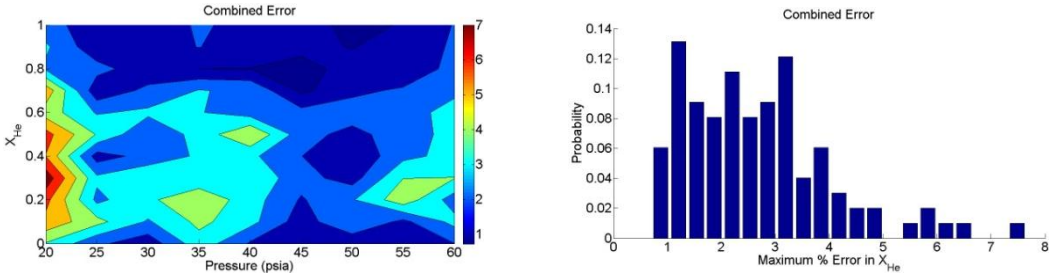

Figure 26: Combined Concentration Error

There appear to be no noticeable trends in the calibration error, whereas instrument errors are higher at lower pressures, due to the transducer's fixed error and convergence of the curves at lower pressures. The sensitivity coefficients are useful for quantifying the relative errors in concentration for arbitrary changes in measurement outputs. For example, the temperature sensitivity indicated that a certain level of temperature bias can be tolerated without noticeably affecting the overall concentration measurement. The following table shows the errors and sensitivities for percent of molar helium concentration.

Table 5: Expected Errors and Sensitivities in X_{He}

	Average	Maximum
Combined Error	2.7%	7.6%
Calibration Error	1.5%	6.0%
Instrument Error	1.1%	2.6%
Temperature Sensitivity	0.59% per °C	0.82% per °C
Pressure Sensitivity	-1.5% per psia	-3.7% per psia
CTA Voltage Sensitivity	0.10% per mV	0.23% per mV

Chapter 5

Frequency Response Characteristics

The probe's overall response depends on the frequency characteristics, i.e. the transfer functions, of the three sensors as well as the probe's internal volume. In previous designs, the limiting factor in mean concentration measurements was plumbing from an internal pressure tap to a transducer outside the test section. In this design, the probe's internal volume is the limiting factor. The volume was minimized to improve the frequency response, allowing sufficient space for instrumentation and preserving aerodynamic constraints.

5.1 Hot-film and CTA system

CTAs incorporate a dynamic compensation circuit which significantly improves the frequency response of the heated filament by itself; dynamic compensation is explained by Doebelin[13]. This principle is often applied to measuring devices where the desired behavior is not obtainable by adjusting its own parameters, and so a lag compensator can be used to improve the frequency response. For the specific case of a hot-film and CTA system, the filament has thermal inertia and requires time to equilibrate with the surrounding medium. A sketch of the filament is shown in Figure 27.

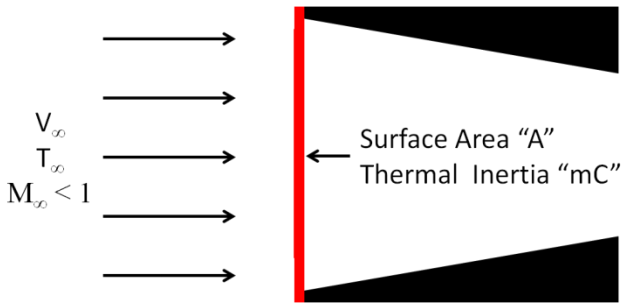

Figure 27: Uncompensated Hot-Film Model

The hot-film's response time to temperature changes in the surrounding medium can be quantified with a simple heat transfer analysis. The hot-film's thermal inertia is equated with the

medium's convective heat transfer. Without feedback to maintain the temperature, the hot-film simply equilibrates with the surrounding fluid at T_∞.

$$mC\frac{dT_{HF}}{dt} = hA(T_{HF} - T_\infty) \tag{5.1}$$

Taking the Laplace transform and solving for the transfer function yields:

$$\frac{T_{HF}(s)}{T_\infty(s)} = \frac{1}{\left(\frac{mC}{hA}\right)s + 1} = \frac{K}{\tau s + 1} \tag{5.2}$$

To demonstrate the need for compensation, a simple approximation is made to estimate the time constant for a 25 μm hot-film immersed in air moving at 20 m/s. The platinum filament has known specific heat and density, the geometry of the wire is known, and the heat transfer coefficient may be quickly approximated using a forced convection empirical equation for turbulent flow over a cylinder, such as the well-known Churchill-Bernstein equation[14]:

$$\overline{Nu}_d = \frac{\bar{h}d}{k} = 0.3 + \frac{Re_d^{1/2}Pr^{1/3}}{[1 + (0.4/Pr)^{2/3}]^{1/4}}\left[1 + \left(\frac{Re_d}{282{,}000}\right)^{5/8}\right]^{4/5} \tag{5.3}$$

This example yields a 95% response time (3τ) of 3.71 ms, or 270 Hz. This frequency response is clearly not adequate for the purposes of detecting any mixture intermittency, since helium residence time is on the order of 1 ms. Further reducing the size of the filament is not practical beyond certain mechanical limits, but a dynamic compensator may be used instead. Hot-films connected to CTAs, after compensation, have a frequency response on the order of 100 kHz. These are analog electronic devices, and can be either active or passive.

This compensation cannot be carried beyond a certain point, due to additional noise, but a response speedup on the order of 100:1 has been demonstrated for hot-film and CTA systems as well as thermocouples. Compensators may be built using any number of components, but a simple RC circuit with amplification is common, shown in the diagram below:

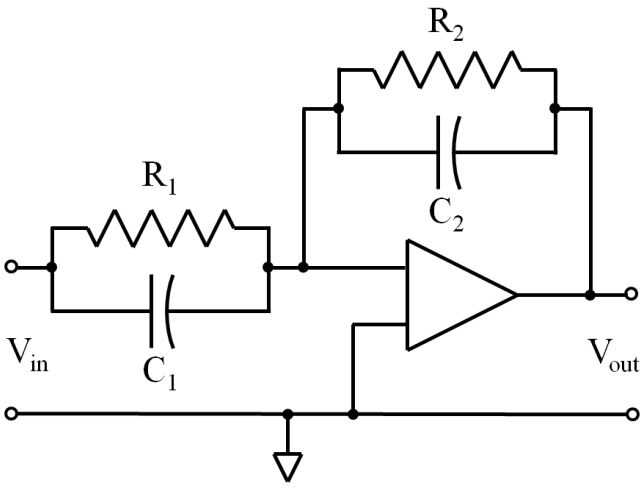

Figure 28: Dynamic Compensation Circuit

The RC lag compensator above has a transfer function of:

$$G_2(s) = \frac{V_{out}(s)}{V_{in}(s)} = \left(-\frac{R_2}{R_1}\right)\frac{R_1C_1s + 1}{R_2C_2s + 1} \tag{5.4}$$

The components are chosen to replace the instrument's transfer function with an improved one. For a 1st order instrument such as the uncompensated CTA, the transfer function is of the form:

$$G_1(s) = \frac{K}{\tau s + 1} \tag{5.5}$$

The value for R_1C_1 is chosen to be the same as τ of the uncompensated system. If τ is unknown or is subject to change, then the compensated system will exhibit 2nd order behavior. By cascading the instrument output with the compensator, the new transfer function of the compensated system becomes:

$$G_3(s) = G_1G_2 = \left(-\frac{R_2}{R_1}\right)\frac{K}{R_2C_2s + 1} = \frac{K_1}{\tau_1 s + 1} \tag{5.6}$$

Thus, the new time constant R_2C_2 may be imposed directly on the system, effectively replacing the undesirable time constant of the original system. For the 1750 CTA used with this probe, the trim and gain are manually adjustable to optimize the frequency response for the flow

impinging on the filament surface. A square wave is sent into one side of the bridge, and the response may be observed on an oscilloscope, allowing the signal to be tuned to the specific system. The goal of fine tuning is to minimize the pulse width, thus improving the response time, while tolerating reasonable pulse amplitude. The frequency response of the CTA output depends on many different factors and must be directly measured. In general, the following factors increase the frequency response: smaller filaments, higher feedback gain, more thermally conductive gas, and higher velocity. This probe has a slightly slower response of ~60 kHz, due to the relatively slow velocity of ~20 m/s impinging on the filament surface in the hot-film plane. The figure below shows the probe's actual CTA square wave response on the left and an optimal response from the TSI handbook[15] on the right.

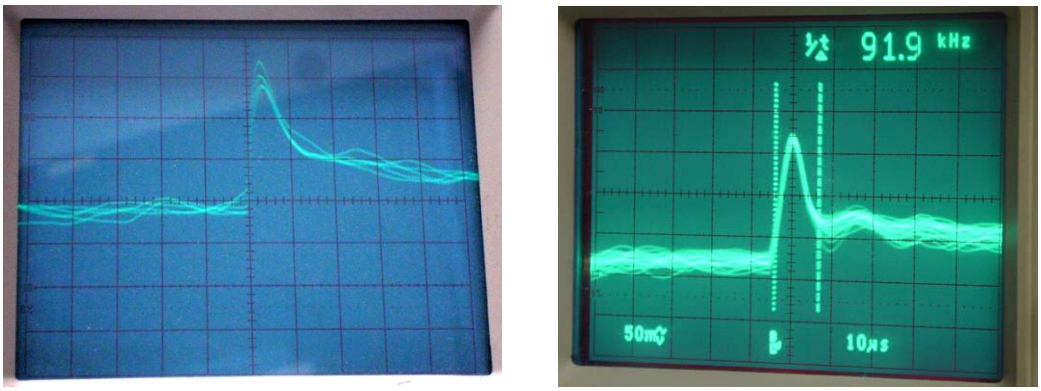

Figure 29: Square Wave Test Oscilloscope Output[15]

5.2 Pressure and Temperature Measurement

Instrument response time is generally provided by the manufacturer. Both the thermocouple and pressure transducer are 1st-order instruments with a gain of unity, and so their transfer functions are fully described by their respective time constants. The pressure transducer's frequency response depends on the natural frequency of its thin silicon diaphragm, which is generally very quick for the subminiature transducers. The probe's specific transducer has an estimated frequency response of 60 kHz.

Like the CTA, the thermocouple's response depends on the sensing element's thermal inertia equated with forced heat convection of the surrounding medium. Assuming lumped heat transfer for the sensor, the energy equation simplifies to:

$$mC\frac{dT_{TC}}{dt} = hA(T_{TC} - T_{\infty}) \tag{5.7}$$

T_{TC} is the temperature of the sensing element. Re-arranging into standard form and then taking the Laplace transform yields the thermocouple's transfer function:

$$\frac{T_{TC}(s)}{T_{\infty}(s)} = \frac{1}{\left(\frac{mC}{hA}\right)s + 1} = \frac{K}{\tau s + 1} \tag{5.8}$$

Time constants are experimentally determined by the vendor for a specific heat transfer coefficient 'h', which is strongly dependent on the velocity impinging on the sensing element. Thermal inertia of thermocouples may be decreased and the surface area increased by using smaller sensors, which greatly improves the time response. Unfortunately, an installation error was made during the probe assembly in which a slower thermocouple was installed in place of the selected unit. This thermocouple is a 24 AWG type-K with a time response of 1.95 seconds, instead of the selected type-K with a time response of 1.0 ms. Due to the risk of disassembling the probe and re-installing the correct thermocouple, it was decided instead to attempt dynamic compensation of the slow type-K.

During calibration, it was observed that temperature changes (if any) were gradual and thus unimportant. However, the same trend was not observed in wind tunnel testing, as the freestream supersonic flow is nominally 133 K at Mach 2.5. Tests seemed to indicate (inconclusively) a rapid drop in internal probe temperature, due to the thin, non-insulated brass exterior. If the thermocouple were not able to measure temperature accurately, the lag would produce major errors in helium concentration. Temperature sensitivity analysis was performed to determine the error in X_{He} for small temperature deviations using the methods in Section 4.4. A maximum error of 0.82% in X_{He} per °C was found. To improve the time response of the

thermocouple, a 10:1 passive dynamic compensation circuit was cascaded with the output. A picture of the RC lag compensator is below:

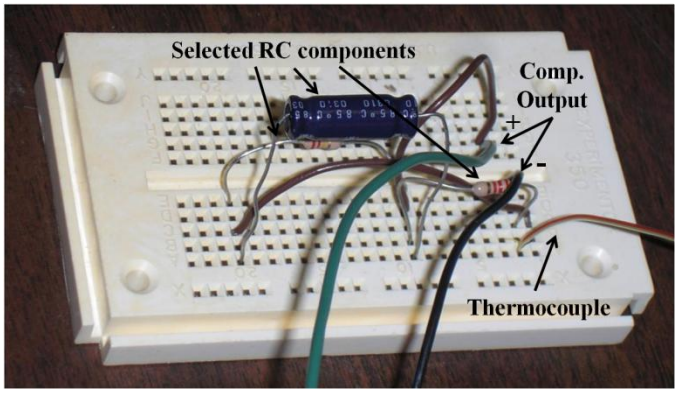

Figure 30: Thermocouple Lag Compensator

This reduced the time constant to 0.195 seconds, or more realistically 0.6 seconds with the expected velocity, which yields the simulated response below for the estimated temperature change:

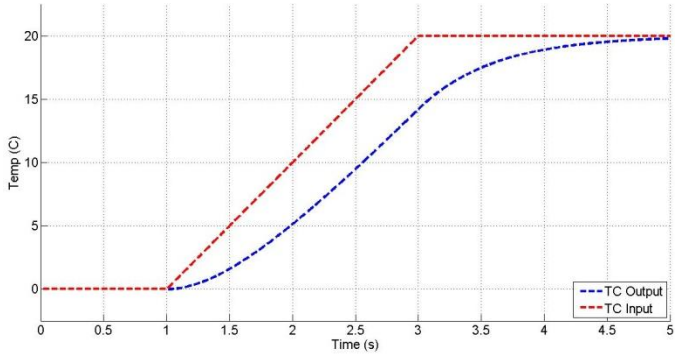

Figure 31: Compensated Temperature Output

In the plot above, there is a clear lag of the thermocouple output from the nominal ramp input of 10 °C/s. The maximum error in the measurement is 6.1 °C, which yields an error in X_{He} of 5%, so further compensation would be required. However, even a 10:1 compensation circuit produced unacceptable levels of noise and biased readings, due to data acquisition issues with

a small input signal of around 0.1 mV. The inability to compensate for the temperature lag led to unreliable temperature readings in the first series of tests, which ultimately prevented reliable measurements of mean concentration, to be discussed further in Section 7.3. At the time of this writing, plans to install the correct, high-frequency thermocouple have been finalized.

5.3 Frequency Response of the Probe's Internal Volume

The overall response time is also limited by the probe's internal volume, which must be filled with the freestream mixture to achieve steady-state. A control volume model is used to calculate the fill time.

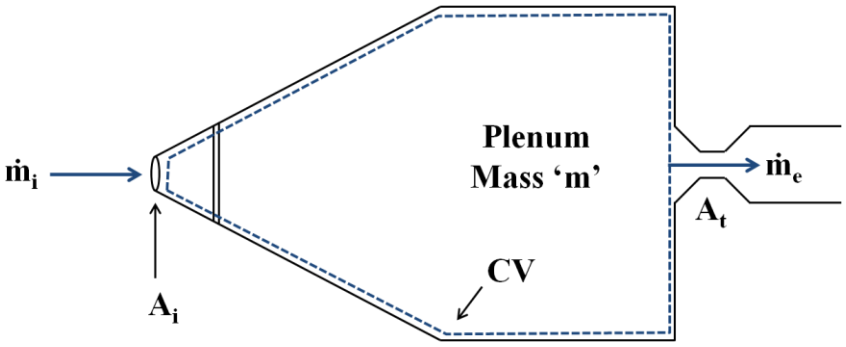

Figure 32: Control Volume Model

The selected control volume encloses the normal shock that occurs in the divergent channel. Continuity accounts for mass flow entering and exiting the probe, while mass accumulates inside the probe for this transient process:

$$\dot{m}_i = \dot{m}_e + \dot{m} \tag{5.9}$$

The perfect gas law may be differentiated in time for mass inside the control volume.

$$m = \frac{PV}{RT} \Rightarrow \dot{m} = \left(\frac{V}{RT}\right)\dot{P} - \left(\frac{VP}{R^2T}\right)\dot{R} - \left(\frac{VP}{RT^2}\right)\dot{T} \tag{5.10}$$

Mass entering and exiting the probe are expressed using stagnation conditions.

$$\dot{m}_i = \left(\frac{P_t A^* C^*}{\sqrt{T_t}}\right)_i \quad \dot{m}_e = \left(\frac{P_t A^* C^*}{\sqrt{T_t}}\right)_e \tag{5.11}$$

The virtual nozzle area A_∞^* is used to quantify $\dot{m}_i$ while the throat area A_t is used for $\dot{m}_e$.

$$\frac{P_{t,i}A_\infty^* C^*_i}{\sqrt{T_{t,i}}} = \frac{P_{t,e}A_t C^*_e}{\sqrt{T_{t,e}}} + \left(\frac{V}{RT}\right)\dot{P} - \left(\frac{VP}{R^2T}\right)\dot{R} - \left(\frac{VP}{RT^2}\right)\dot{T} \tag{5.12}$$

This is the most general form for massflow through the probe for a perfect gas mixture. A_t and V are fixed geometric quantities. A_∞^* is calculated with the fixed inlet area A_i, and is dependent on M_∞ and γ. Every other variable is related to the gas composition and thermodynamic state, evaluated at different points in space. In general, all non-geometrical quantities can be functions of time.

To approximate the response time of this system, the continuity equation must be simplified. First, the control volume may be modeled as a plenum, since $P/P_t > 0.99$ for 97% of the volume. Stagnation and static conditions are negligibly different. Second, the entire system is assumed adiabatic, and therefore the total temperature T_t is constant everywhere in the system. This assumption is reasonable for a time interval of $\mathcal{O}(10\ ms)$. Lastly, the composition is fixed for this calculation. A calorically perfect gas assumption is valid for the expected pressure and temperature ranges, so C^* is also fixed. Re-writing the simplified continuity equation:

$$\frac{P_{t,i}A_\infty^* C^*}{\sqrt{T_t}} = \frac{PA_t C^*}{\sqrt{T_t}} + \left(\frac{V}{RT_t}\right)\dot{P} \tag{5.13}$$

The only remaining differential term is pressure. Re-arranging into standard form yields:

$$\dot{P} + \left[\frac{A_t C^* R\sqrt{T_t}}{V}\right]P = \left[\frac{A_t C^* R\sqrt{T_t}}{V}\right]\frac{A_\infty^*}{A_t}P_{t,i} \tag{5.14}$$

This is a first-order system with a time-dependent forcing function. The term in square brackets is constant. The transfer function is determined using the Laplace transform, and models the probe's response to any arbitrary input. Imposing that P(0) = 0:

$$H(s) = \frac{P(s)}{P_{t,in}(s) * \frac{A_\infty^*}{A_t}(s)} = \frac{1}{\left(\frac{V}{A_t C^* R\sqrt{T_t}}\right)s + 1} = \frac{K}{\tau s + 1} \tag{5.15}$$

The time constant τ is easily recognizable for this first-order system.

$$\tau = \frac{V}{A_t C^* R \sqrt{T_t}} \tag{5.16}$$

The response time is defined as 3τ for a 95% response to a step input. To improve the response time, one must decrease the internal volume or increase the throat size. τ does not depend on A_∞^*, a function of the freestream Mach number. Trade-off studies were performed to minimize volume while allowing space for instrumentation, and to increase the throat area without violating any aerodynamic constraints. The inlet area A_i was chosen to be small for improved spatial resolution in the freestream, and A_t/A_i is limited by the desired Mach number range of the probe.

The derivation of τ is based on an analytical model; no consideration is given to the internal geometry, flow obstacles, or area changes in its calculation. A 1-dimensional model was therefore used to calculate the particle flush time through the probe under steady-state conditions. This is used to validate the control volume prediction. The maximum flush time is conservatively calculated by taking $M_\infty = 1.8$. The Mach number is known everywhere inside the probe from the 1-dimensional area-Mach relation. The speed of sound and velocity are then calculated for each area. A numerical approach is taken to find the flush time, taking the sum of discrete lengths along the particle flow path. Results of both calculations are shown in Table 6.

Table 6: Response Times

	Air	Helium
Internal volume	8.49 ms	2.98 ms
Flush time	2.83 ms	0.992 ms

5.4 Overall System Characteristics

Nominal freestream inputs to the probe are helium concentration, pressure, temperature, and Mach number. The Mach number establishes the pressure ratio across the swallowed normal shock, and can be considered as a combined input of pressure and helium

concentration, since the shock strength depends on Mach number and γ. The overall time response as related to the instruments may be determined from the block diagram below:

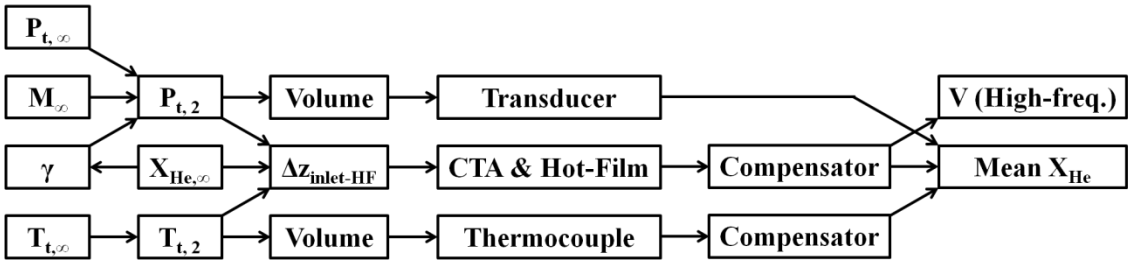

Figure 33: Probe Frequency Response Block Diagram

Each block has a given transfer function, and the final output depends on the overall system. For pressure and temperature, the internal volume must be filled before the instruments themselves respond to ambient conditions. The hot-film is not limited by the volume of the probe, and instead undergoes mixing in the space $\Delta z_{inlet\text{-}HF}$. Therefore the main limiting factor on the frequency response for mean concentration measurements, assuming the correct thermocouple is installed, is the fill time of the internal volume. To calculate the probe's slowest response for mean concentration measurements, a normalized temperature step is input at the inlet. The plenum must then be filled with the mixture at the new temperature, which heats the thermocouple sensor. A Simulink model was built to cascade these two transfer functions and output the response, and the results are presented below:

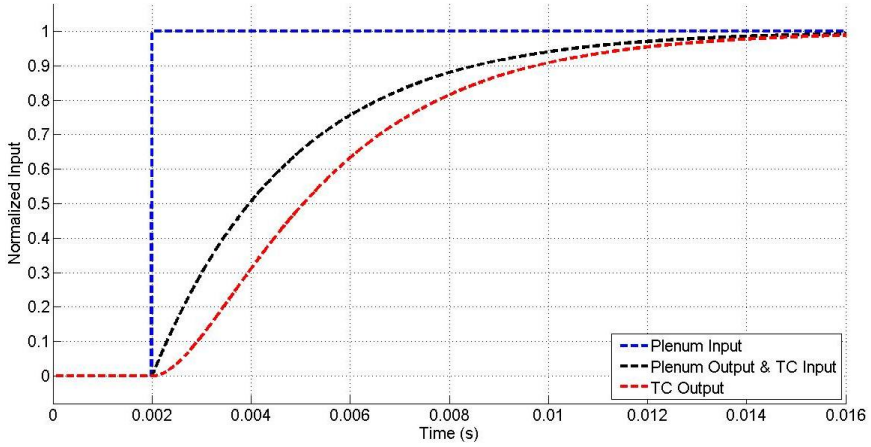

Figure 34: Prediction of Overall Probe Frequency Response

The slowest case is for 100% air, where the 95% time response has been calculated as 8.49 ms, which is confirmed by this model. The plenum temperature output is also the thermocouple sensor input, and the thermocouple output is then increased to 9.72 ms. Therefore the overall frequency response of the probe, with the correct thermocouple, is 103 Hz for *mean* concentration measurements.

Chapter 6

Analysis of High-Frequency CTA Voltage Trace

In addition to mean concentration measurements, high-frequency mixing behavior can be implicitly derived from the CTA voltage trace. This data is useful for interpreting the appropriateness of mean concentration measurements from UTA's new laser-based system, because an averaged measurement where intermittent mixtures exist is *not sufficient* to characterize the flow, and therefore assess mixedness. The hot-film responds to the *local* mixture impinging on its surface, and is therefore not constrained by the probe's internal volume like temperature and pressure measurements. However, the usefulness of this additional data has practical limitations. Like any instrument, the output is a time-area-averaged measurement. Temporal resolution is limited by the finite system response, while spatial resolution is limited by machining capabilities and instrument size. Additionally, internal mixing occurs from the sampling point to the sensor plane. High-frequency measurements are consequently distorted, and the output will erroneously indicate exaggerated mixing.

6.1 Mixing Behavior from CTA Voltage Trace

Vortices are intentionally introduced into the flowfield considered in this study. Mean concentration measurements serve to quantify helium dispersion in air, but they do not describe mixing at the *molecular* scale, which is essential for combustion. For example, the probe would output a 50% concentration value for rapidly alternating pockets of air and helium. The hot-film and CTA system has a frequency response of $\mathcal{O}(100\ kHz)$, and can detect different species over time. High-frequency fluctuations in *helium concentration* cannot be explicitly determined due to time lag of the probe's internal volume. However, as seen in the calibration curves, the CTA voltage is a strong function of helium concentration and some mixing behavior may still be determined through qualitative and quantitative analysis.

The probability density function (PDF) is a valuable tool in mixing studies, as it enables distinction of separate mixtures that are not otherwise evident. In the calibration phase, the PDFs are expected to be tightly bound Gaussian distributions centered about the CTA voltage that corresponds to the *nominal* helium concentration in the calibration tank. PDFs of the CTA voltage do not *exclusively* correspond to helium concentration, because $V = f(X_{He}, P_t, \text{and } T_t)$. If pressure and temperature dependence are neglected in the short timespan for which high-frequency data is recorded (usually a reasonable assumption), then any deviations from this Gaussian distribution may be attributed to concentration intermittency, i.e. multiple mixtures. Tightly bound PDFs indicate excellent mixing (or only 1 mixture present). Two peaks in a PDF indicate the presence of two separate mixtures impinging intermittently. To illustrate the behavior of the CTA voltage over a discrete time interval, two example cases are plotted from calibration data. These cases demonstrate certain physical phenomena that occur at different pressures and concentrations.

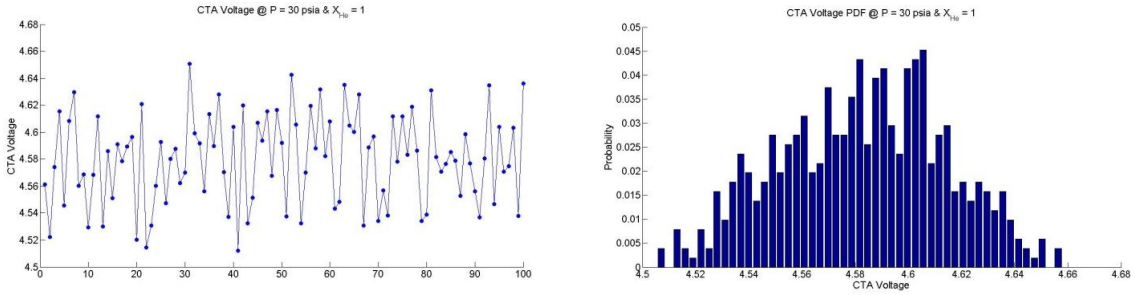

Figure 35: CTA Voltage Traces & PDFs for $X_{He} = 1.0$ @ 30 psia

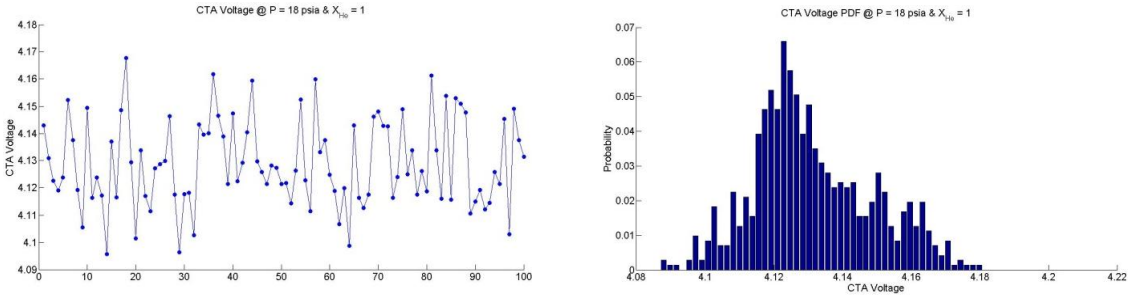

Figure 36: CTA Voltage Traces & PDFs for $X_{He} = 1.0$ @ 18 psia

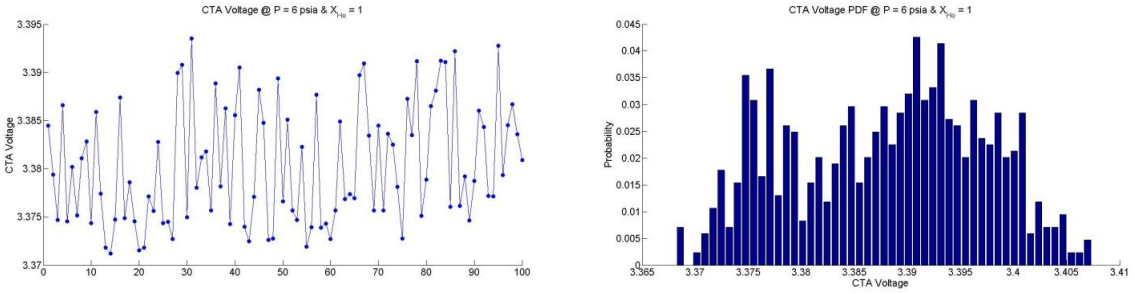

Figure 37: CTA Voltage Traces & PDFs for X_{He} = 1.0 @ 6 psia

Figure 35 through Figure 37 above are for 100% helium at three different pressures. CTA voltage increases with pressure for a fixed composition, as expected from eq. (2.10). Fluctuations about the nominal voltage become larger as pressure increases, since more mass is impinging on the hot-film. The voltage fluctuations here are not due to the presence of multiple mixtures, but rather due to turbulence because only helium is present. For a uniform mixture in turbulent flow, a Gaussian distribution is theoretically expected in the PDF. These three PDFs indicate that for the timeframe examined, the concentration does not deviate significantly from its nominal value. For PDFs that resemble a Gaussian distribution, a mean concentration measurement by any probe or laser is sufficient to characterize the concentration in time. A second case is now examined with multiple species for X_{He} = 0.3.

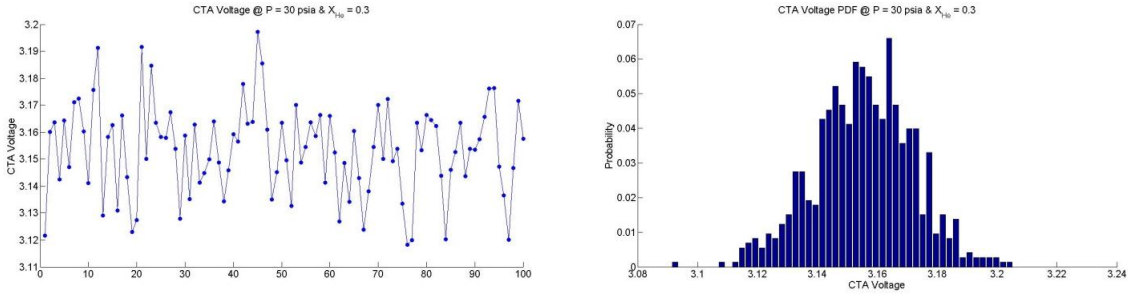

Figure 38: CTA Voltage Traces & PDFs for X_{He} = 0.3 @ 30 psia

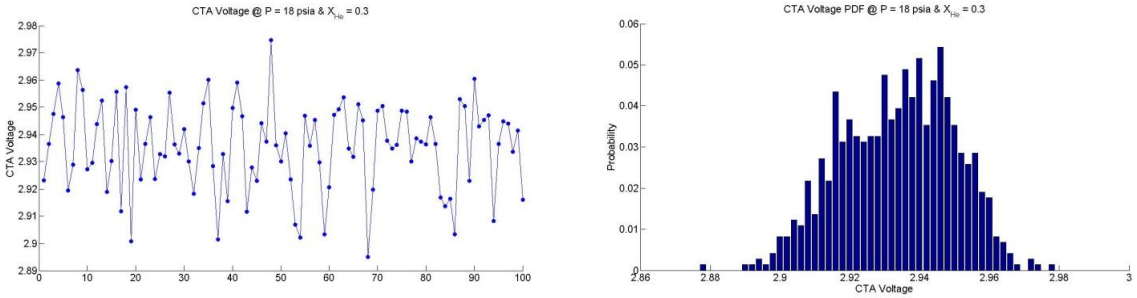

Figure 39: CTA Voltage Traces & PDFs for X_{He} = 0.3 @ 18 psia

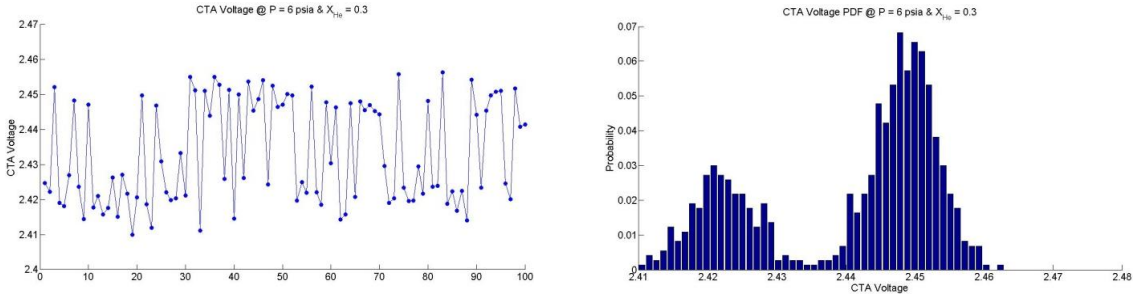

Figure 40: CTA Voltage Traces & PDFs for X_{He} = 0.3 @ 6 psia

At this concentration, two distinct *peaks* occur at the lowest pressure in Figure 40, which resembles a bimodal distribution. This deviation from a single Gaussian distribution indicates two statistically distinct *mixtures* impinging on the hot-film intermittently. For PDFs with multiple peaks, the additional high-frequency data is essential to understand concentration fluctuations in this timeframe. A mean concentration measurement by any probe or laser would indicate an averaged concentration corresponding to some intermediate CTA voltage between the two peaks, which is *not sufficient to temporally characterize the concentration*. In the calibration tank, these peaks represent either intermittent air leaks due to sub-atmospheric tank pressure or helium stratification. With positive gauge pressure inside the tank, the tank mixture will vent to the atmosphere, but with negative gauge pressure, ambient air may leak into the tank and contaminate the nominal helium concentration. This effect is also why the most recent calibrations did not include lower target pressures. In either case, two different mixtures are

being sampled intermittently, which is exactly what these PDFs are intended to detect in supersonic flow. To further illustrate the behavior of the CTA voltage over an array of pressures, an example calibration curve is shown below with PDFs superimposed for each nominal P-V point.

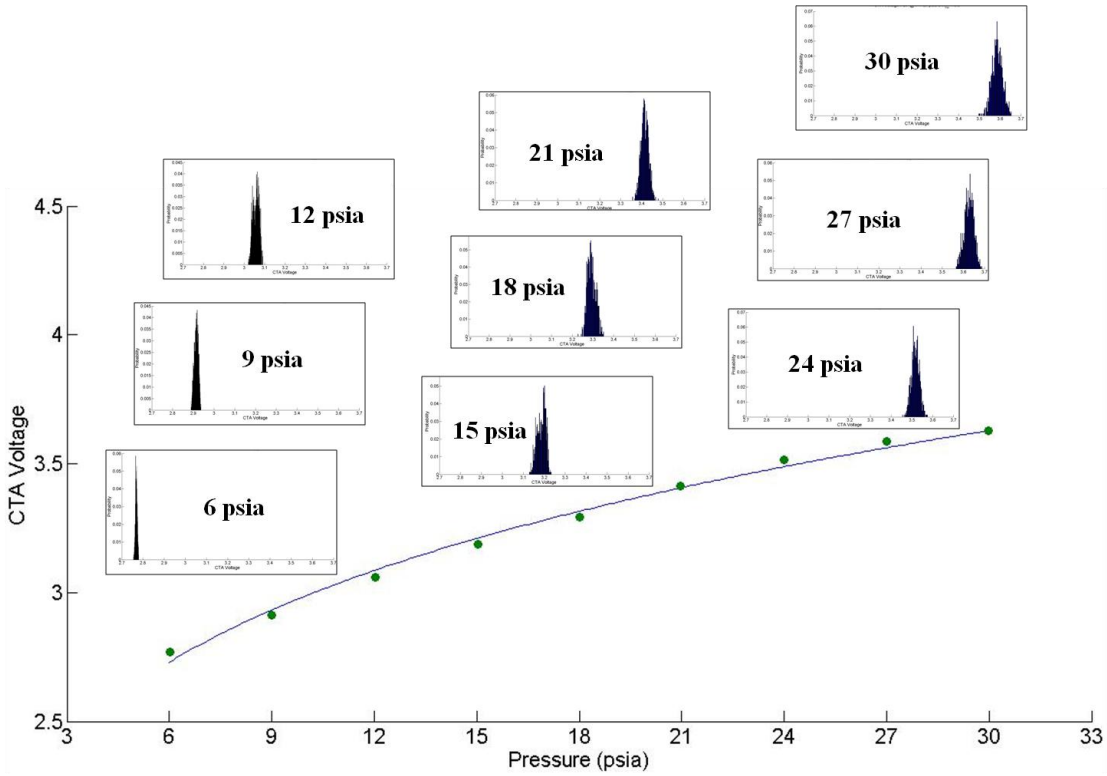

Figure 41: PDFs of CTA Voltage for X_{He} = 0.6

The above PDFs are all closely Gaussian, which is desirable in the calibration tank where multiple peaks would cause errors in the nominal CTA voltage. In supersonic tests, the detection of multiple, intermittent mixtures at a fixed point in space is a critical component to improving these fuel injection schemes. In order to capture this intermittency, the Nyquist criteria must be satisfied to record this high-frequency behavior, both from the CTA and data acquisition system.

As a simple example, the hot-film and CTA system's ability to spatially resolve an eddy of the same diameter of the inlet is examined. Ignoring the effects of the normal shock and internal mixing, the residence time of the eddy across the hot-film is simply its diameter divided by its velocity across the hot-film. With an eddy of diameter 0.0135" (0.343 mm) and a velocity of ~20 m/s, the residence time of the eddy is ~17 μs. The 60 kHz CTA system cannot satisfy the Nyquist criteria in this case, which demonstrates that coherent structures entering this probe (which have a *maximum* diameter of the inlet) are not temporally resolvable. However, the probe's intended purpose is to measure a scalar concentration value, and determine if multiple mixtures are intermittently sampled. The entire flowfield of interest must be probed and analyzed before any determination of the mixing characteristics of freestream vortical structures may be assessed. The probe measures *mean* concentration using all three instruments, while the PDFs, with proper assumptions and analysis, indicate the *mixedness*, i.e. whether or not the concentration of a fixed point changes with time.

6.2 Time-Area-Averaged Measurement

In turbulent flowfields, identifying the flowfield's characteristic time and length scales is crucial for mixing measurements. Comparison with an instrument's temporal and spatial resolution will quantify the instrument's capacity to measure some physical aspect of the flowfield. The CTA ultimately measures a time-area-average, which corresponds to the mixture impinging at the physical scale of the hot-film, averaged over the time required for the hot-film to respond. This corresponds to a volume of fluid which is visualized in the sketch below:

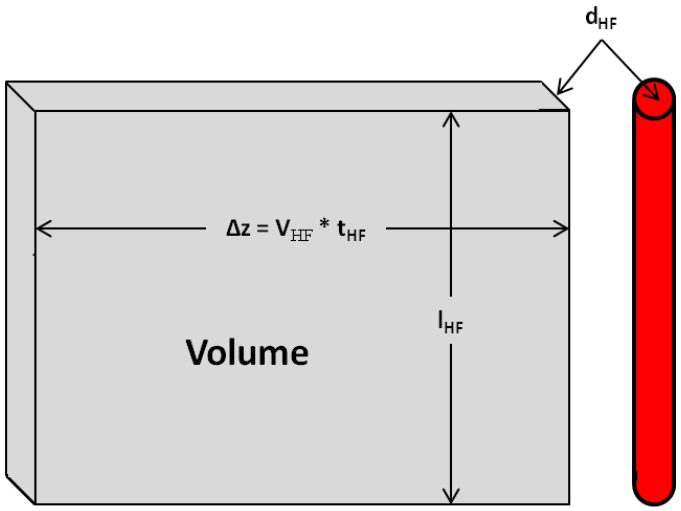

Figure 42: Hot-Film Time-Area-Average

This volume of fluid is easily calculated as d_{HF} x l_{HF} x Δz, where Δz is defined above as the hot-film impingement velocity V_{HF} times the hot-film's time response t_{HF}. For a ~20 m/s impinging velocity and the hot-film's 17 μs time response, Δz is 0.34mm, and thus the volume is 0.0021 mm^3. This is the *best* resolution that this system can attain. Put simply, these high-frequency measurements are limited to the *average* mixture inside this volume. Decreasing the volume requires shrinking the filament, which is not practical below a certain size, or reducing Δz, which is difficult since decreasing V_∞ increases t_{HF} and vice versa. Estimation of the flowfield's length scales will reveal how this resolution compares.

The flowfield in the current study is highly turbulent, and its characteristic time and length scales are very small. The Kolmogorov hypothesis from Pope[16] is used to approximate these scales using combined empirical and analytical methods. The Kolmogorov length scale, denoted l_k, is the diameter of the smallest eddy in the flowfield just before viscous dissipation. The integral scale, denoted L, is the diameter of the largest turbulent eddy in the flow. Turbulence can be modeled as a cascade of progressively smaller turbulent eddies, and each eddy contains energy from its velocity components. Turbulent kinetic energy (TKE) corresponds to the *fluctuating* velocity component only, and is defined as:

$$TKE = {}^{1}/_{2}\left(\overline{u'^2} + \overline{v'^2} + \overline{w'^2}\right) \tag{6.1}$$

Turbulence enhances mixing by increased molecular diffusion, and in this study a higher TKE is desirable to increase helium and air mixing. Each turbulent eddy contains a certain amount of TKE, which increases with larger structures. The wavenumber κ, defined as $2\pi/d_e$, is inversely proportional to the eddy diameter d_e. The logarithmic plot below qualitatively shows the TKE distribution as a function of wavenumber for isotropic turbulence.

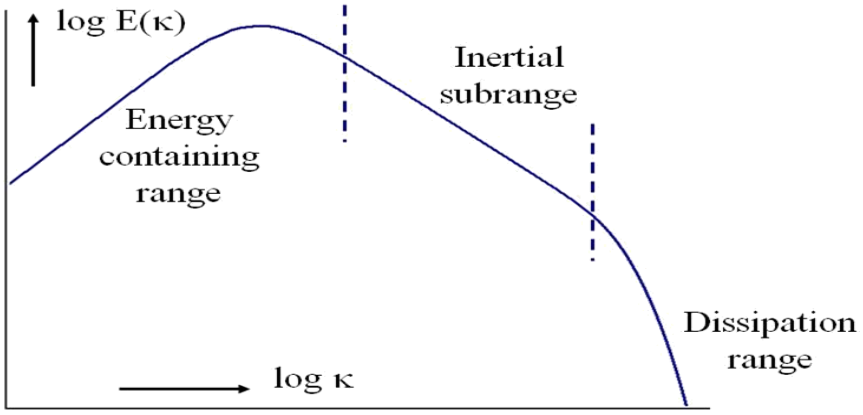

Figure 43: Turbulent Energy Spectrum[16]

The ratio of L to l_κ indicates to what degree the largest eddies in the flow break down into smaller eddies before viscous dissipation. Higher freestream Reynolds numbers result in smaller l_k according to the expression[16]:

$$\frac{L}{l_\kappa} = Re^{3/4} \tag{6.2}$$

Since mixing occurs at all scales, measurements (in principle) should be made at or below this minimum length scale. In the current study L is of $\mathcal{O}(1\ cm)$, the same size of the induced vortical structures in the flowfield, and Re is of $\mathcal{O}(10^5)$. For this vortex-dominated flowfield, Re is evaluated as vortex circulation Γ divided by the kinematic viscosity v. Therefore l_κ, the smallest characteristic length scale for turbulent flow, is of $\mathcal{O}(1\ \mu m)$. For applications with high Reynolds number, e.g. a complex supersonic flowfield, this order of spatial resolution is an

obstacle. Measurements at this scale are not realistically attainable for *any* modern probe or laser. Resolving the flowfield with DNS is also impractical with modern CFD and processing speeds, as the real 3-dimensional flow requires a mesh size at this scale to accurately model the physics. For this probe, spatial resolution is limited by machinability and instrument size, and the hot-film diameter is typically of $\mathcal{O}(25\,\mu m)$. This limitation must be recognized for any measurement in a flowfield with irresolvable characteristic scales. To this end, the smaller length scales are often neglected to obtain quantitative results.

For combustion to occur, mixing of air and hydrogen is required at the *molecular* scale. The challenge is how to predict and interpret mixing at the molecular and Kolmogorov scales based on measurements from a system that lacks the required temporal and spatial resolution as discussed in this section. This is one of the main reasons why mixing at high Reynolds numbers is still an active research area, and is currently being studied for this project.

6.3 Internal Mixing Effects

Additional mixing inevitably occurs from the sampling point to the sensor plane, and understanding this limitation on the probe's high-frequency measurements is critical. After the mixture enters the inlet, the effect of this secondary mixing may be determined by comparison of the flow residence time inside the probe and characteristic mixing times. The CTA trace will usually indicate any mixture intermittencies within its resolution, which includes the combined freestream and internal probe mixing. If the effect of internal probe mixing is accounted for, the actual freestream mixing (i.e. the desired output) may be accepted with its limitations. Three mixing mechanisms are expected inside the probe and will be examined in this section, and a physical interpretation of these mechanisms is modeled using the figure below:

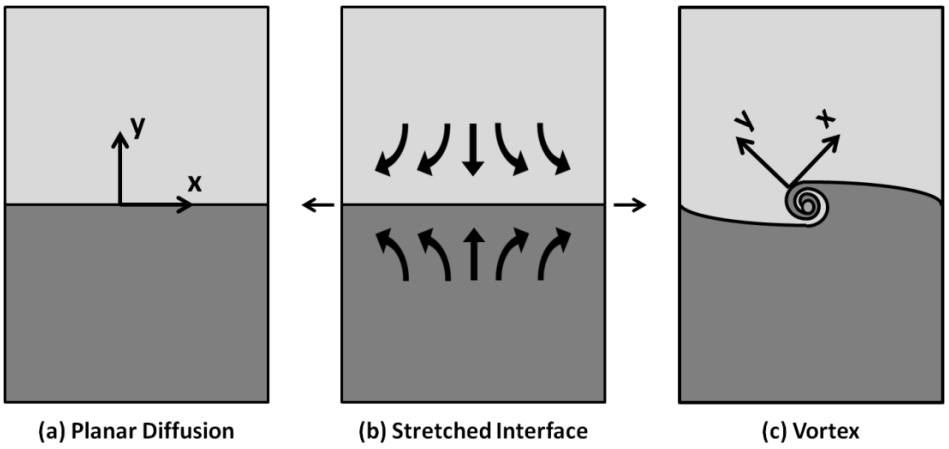

Figure 44: Mixing Interface Scenarios[17]

Two mixing mechanisms are clearly distinguishable here. Molecular diffusion (a) occurs at any species interface. If a normal strain rate (b) is applied at the interface, mixing is promoted by increasing both the interface area and the local concentration gradients as each mixture penetrates the other. A vortex (c) is analyzed as a simple example for mixing enhancement. If a vortex is introduced into the flow, the local species interface is distorted and stretched in time. The third mixing mechanism is the augmentation of molecular diffusion by turbulent motion. The scalar diffusion equation models mass transfer across a local fluid interface in time, and incorporates each of these mixing mechanisms. The following equation is presented by Waitz[17] for a binary gas mixture.

$$\frac{\partial C}{\partial t} = D_t(x,y,z,t)\frac{\partial^2 C}{\partial y^2} + \varepsilon_{yy}(x,y,z,t)y\frac{\partial C}{\partial y} \tag{6.3}$$

C is the mass concentration, D_t is the turbulent mass diffusion coefficient, and ε_{yy} is the normal strain rate at the interface. The y-coordinate is normal to each *local* fluid interface, as indicated in Figure 44 above. Equation (6.3) quantifies the rate of change in mass concentration of one species along the y-coordinate over time. In general D_t is a tensor, but reduces to a scalar quantity for isotropic turbulence, a common assumption in turbulent mixing studies. A turbulent model is presented by Waitz[17] to estimate augmentation of molecular diffusion due to

turbulence. For the flowfield in this study, molecular diffusion is enhanced by a factor of $\mathcal{O}(10)$. In this 2D example, ε_{yy} is related to a vortex of circulation Γ according to Waitz[17]:

$$\varepsilon_{yy} \sim \frac{\Gamma}{\pi r^2} \tag{6.4}$$

Here, r is the local radial coordinate from the vortex core, although the equation is not valid as r → 0, because stretching only takes place *outside* the viscous core. In general, both D_t and ε_{yy} are defined at each point in space and time, but may be assumed constant for small time intervals. To quantify vortex mixing augmentation in (6.3), ε_{yy} is initially set to zero, and the equation reduces to Fick's 2nd law. For an initially unmixed layer of 2 species such as part (a) of Figure 44, the solution to Fick's 2nd law is:

$$C_{He}(y,t) = erf\left[\frac{y}{\sqrt{4D_t t}}\right] \quad and \quad C_{air}(y,t) = 1 - erf\left[\frac{y}{\sqrt{4D_t t}}\right] \tag{6.5}$$

When ε_{yy} is non-zero, a solution of the same form is obtained by applying the following substitutions for y and t, and is shown for constant values of ε_{yy}:

$$\zeta = y\, exp\{\varepsilon_{yy} t\} \quad and \quad \lambda = \frac{exp\{2\varepsilon_{yy} t\} - 1}{2\varepsilon_{yy}} \tag{6.6}$$

The solution then becomes:

$$C_{He}(y,t) = erf\left[\frac{\zeta}{\sqrt{4D_t \lambda}}\right] \quad and \quad C_{air}(y,t) = 1 - erf\left[\frac{\zeta}{\sqrt{4D_t \lambda}}\right] \tag{6.7}$$

Mixing enhancement due to the normal strain rate is dependent on the ratio of the flow residence time compared with the strain rate itself. The quantity $t_{res} \times \varepsilon_{yy}$ determines the magnitude of this enhancement at the local interface; if $t_{res} \times \varepsilon_{yy} << 1$, there is insufficient time for the interface to stretch significantly, and the mass transfer is similar to that of the unstrained case. The residence time from the inlet to the sensor plane is determined using the methods described in Section 3.2. The area ratios determine the Mach number, because the flow is choked downstream, and the velocity is calculated using static temperature from the isentropic flow relations.

Once the mixture enters the probe, the normal shock will alter the mixing behavior between the pre-shock and post-shock regions. The model below shows these two regions:

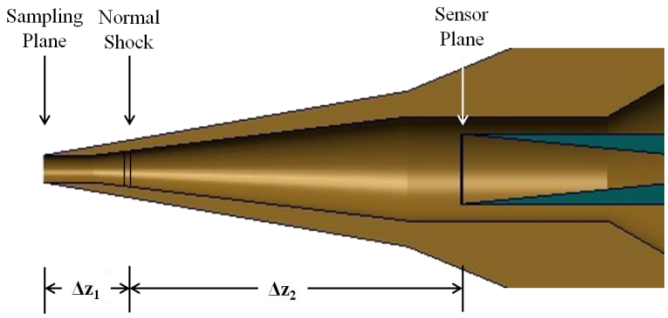

Figure 45: Internal Probe Mixing Region

Freestream coherent structures do not play a significant role in internal probe mixing. The *largest* vortex that enters the probe will have the same diameter as the inlet, and the side walls will tend to dampen this vorticity regardless. The normal shock occurs very close to the inlet, and so the supersonic region over the length Δz_1 has a maximum residence time of 2 μs, compared with the subsonic region whose residence time is 170 μs. For this reason, pre-shock mixing may be safely neglected. Consider a hypothetical example where unmixed fluid enters the probe in a stratified manner, as indicated in Figure 46.

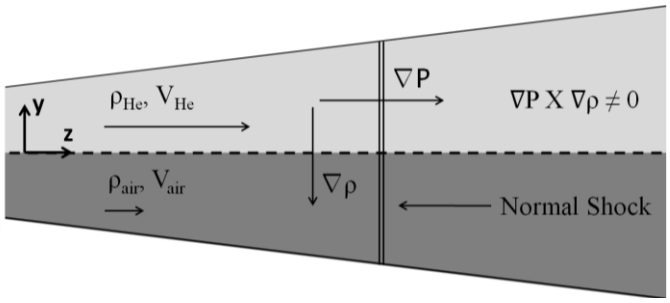

Figure 46: Shock-Induced Vorticity

A strong pressure gradient is induced by the normal shock and is always oriented in the z-direction. Due to the misalignment of the pressure and density gradients that results from multiple species, baroclinic vorticity is generated according to the following equation:

$$\frac{D\Gamma}{Dt} = \int \frac{1}{\rho^2}(\nabla\rho \times \nabla P) \cdot \vec{n} dA \tag{6.8}$$

In this example, the baroclinically produced vorticity will coalesce into a coherent structure similar to Figure 44c. Marble[18] analytically derived mixing augmentation due to the introduction of a vortex in the flowfield, and presented the following relation:

$$Augmented\ Mixing\ Ratio \sim 1 + \left(\frac{\Gamma}{D_t}\right)^{2/3} \tag{6.9}$$

This augmented mixing ratio is the ratio of mixing with a vortex of circulation Γ compared to the unstrained case with turbulent molecular diffusion, i.e. Fick's 2nd Law. As an example, the supersonic flowfield in this study contains vortices with measured circulation of 1.6 m^2/s, and D_t is approximated based on thermodynamic conditions as 1.5 cm^2/s. Marble's relation predicts an augmented mixing rate of ~500! Equation (6.9) demonstrates quantitatively the value of introducing vortical structures into the flow to enhance mixing. This enhancement also occurs from vortices generated across the normal shock inside the probe, which will enhance mixing but be much weaker than the freestream structures.

The purpose of this discussion was to demonstrate that internal mixing is a significant problem which must be considered, even in the short timespan of 170 μs. In general, the incoming flow will have a complex 3-dimensional fluid interface. Because the nature of the incoming mixture is unknown (indeed, it is to be measured), correction for this internal mixing effect is impossible for any arbitrary incoming flowfield. Although mean concentration measurements remain accurate, the high-frequency components measured at the sensor plane will always be distorted and exaggerated by additional mixing. Mixing behavior at the *sampling plane* is the desired output, but aerodynamic constraints dictate that measurements must occur downstream at the hot-film *sensor plane*. High-frequency measurements of the CTA voltage must take these internal mixing effects into consideration to determine the proper freestream mixing conclusions.

Chapter 7

Experimental Design Verification in Supersonic Flow

Two sets of tests were performed to demonstrate the probe's operation in supersonic flow. The first test used Schlieren photography to verify that the bow shock was swallowed, thus validating the crucial assumption of isokinetic sampling. The second test was a 1-dimensional traverse perpendicular to a free mixing layer of helium and air, intended to verify that the probe measured the expected helium plume in supersonic flow. An independent measurement from a Filtered Rayleigh Scattering system was used to predict this plume as a basis for comparison. Additionally, the high-frequency hot-film trace was investigated to quantify the intermittency of helium (if any) in the helium plume. Unfortunately, due to the erroneous installation of an incorrect thermocouple which could not be compensated, mean concentration measurements (which rely on temperature) were irretrievable from existing datasets. However, it was successfully demonstrated that the leading edge shock was swallowed, and quantitative high-frequency data was obtained during the test runs. Plans have been finalized at the time of this writing to install the correct, fast thermocouple and perform an additional series of tests.

7.1 Supersonic Test Facility and Setup

Tests were conducted in the supersonic wind tunnel (SSWT) of the Aerodynamics Research Center (ARC) at The University of Texas at Arlington (UTA). The tunnel is a blow-down type outfitted with a variable Mach number nozzle with ranges from Mach 1.5 to Mach 4.0. For these tests, the nozzle was set to nominally achieve Mach 2.5 in the test section. The test section has dimensions of 6.0" x 4.5" x 30" with sufficient optical access of the flowfield through a side plate. Nominal stagnation conditions are set to 650 kPa and 300K, yielding a unit Reynolds number of 60 x 10^6 per meter. The storage tank is filled to yield approximately 12 seconds of steady run time. A strut-type fuel injector[19] sonically injects helium into supersonic air through a 3.5" slit. The helium flowrate is calculated by measuring stagnation conditions in

the injection plenum and assuming choked flow at the narrowest point in the injection line. This injector is the platform for mixing enhancement schemes currently being studied for this project, but without enhancement simply generates a two-dimensional free mixing layer downstream of the injection point. A CAD model is shown below:

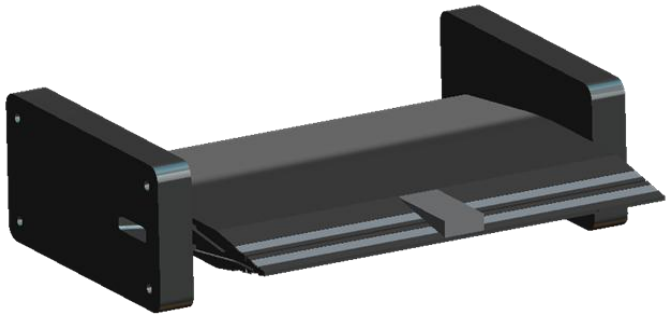

Figure 47: Fuel Injector[20]

A new two-dimensional traversing system was designed for the SSWT to accommodate intrusive measurements for this test campaign, including helium concentration. The top plate of the SSWT was re-designed into a platform which is able to translate with two degrees of freedom. A stainless steel arm is attached to the platform and holds an instrument rake inside the test section. Precision movement is controlled by two Velmex BiSlide stepper motors on alternate axes connected to a VXM Stepping Motor Controller. A cover box was built over the platform to reduce exposure to ambient conditions during test runs, which also provided an exit port for the instrument's wiring and tubing. The system can be implemented at three strategic downstream coordinates with respect to the injection point; for these tests, a downstream distance of 93 mm was surveyed. A CAD model of the system is shown below.

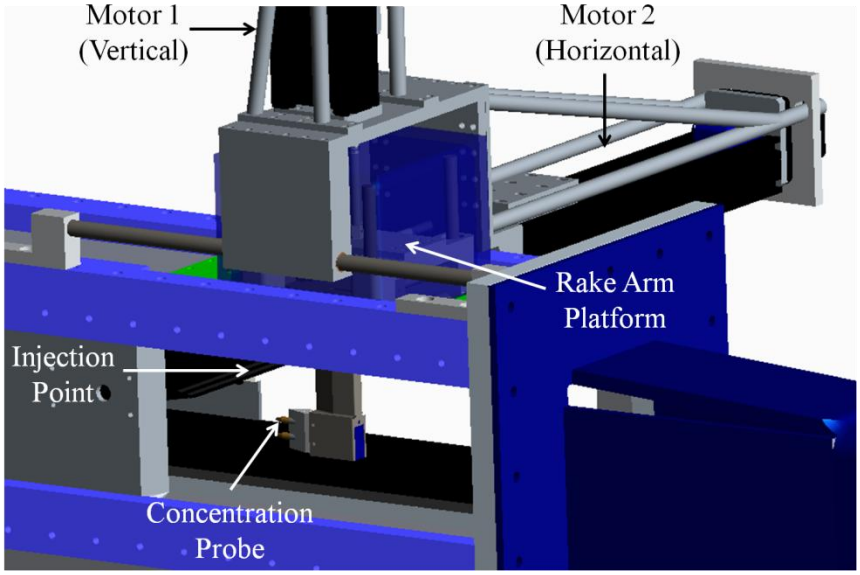

Figure 48: CAD Model of 2D Traversing System

A LabView VI was constructed by the author to interface with this new traversing system, controlling motor movements and acquiring data in timed intervals. The VI was designed to be adaptable to other instrument arrays as well. The user inputs the desired 2-dimensional traversing distances and step size, and the VI generates an array of motor commands for each nominal position. After aligning the probe to the injector center and initializing motor and data acquisition preferences, the VI alternates sending commands to the motor controller via a serial cable and recording data via the DAQ in specified time intervals. The same data acquisition system was used for these tests as for calibration. The output can be monitored before and during the run. This VI collected 2500 samples at 41 positions along the vertical centerline within the 12 second run time constraint. A screenshot of the partial interface is shown below:

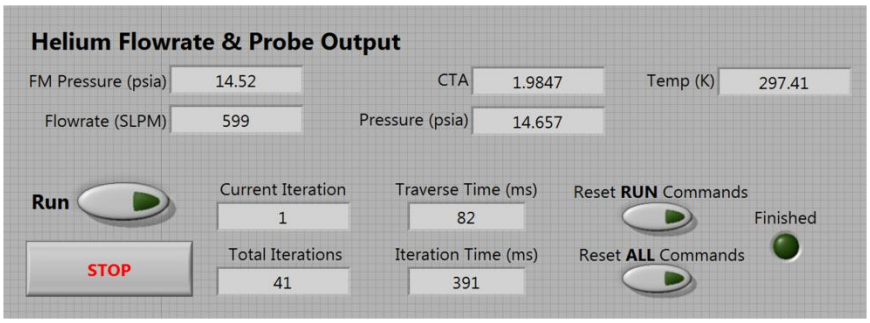

Figure 49: SSWT Traversing VI Interface

A rake holder was specifically designed to house the probe during test runs, with an additional space for a second probe if needed. For these tests, the second slot is filled with a sharp cone, i.e. a dummy probe. The design is minimally intrusive and encloses the probe's wiring and tubing, which then pass through the rake arm and exit the test section through an exit port in the cover box. The CAD model and image below shows the rake holder concept and its successful integration into the new traversing system in the SSWT.

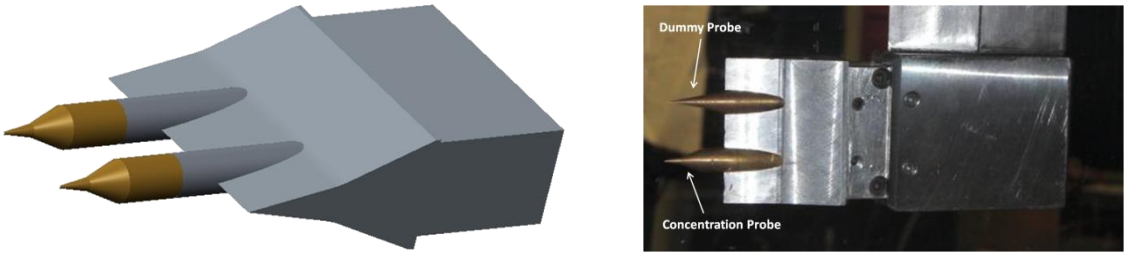

Figure 50: Concentration Probe Rake Holder

A non-intrusive laser-based setup has recently been implemented in the SSWT for independent measurements of mean concentration profiles[21]. The specific technique used is Filtered Rayleigh Scattering, which involves casting a laser sheet spanwise across the flowfield, filtering the signal of other elastic scattering processes and background reflections, and capturing the signal of the scattered molecules on a CCD camera. The system uses a Surelite EX Nd:YAG Laser with an NP Photonics Rock Fiber Laser Seeder attached to a TSI Model

610024 Light Sheet Collimator. The iodine filter was manufactured by Innovative Scientific Solutions, Inc. and the signal is captured with an LaVision Imager Intense CCD camera equipped with a 50mm lens and synchronized with LaVision Davis 7.1 software. A CAD model of the system is shown below:

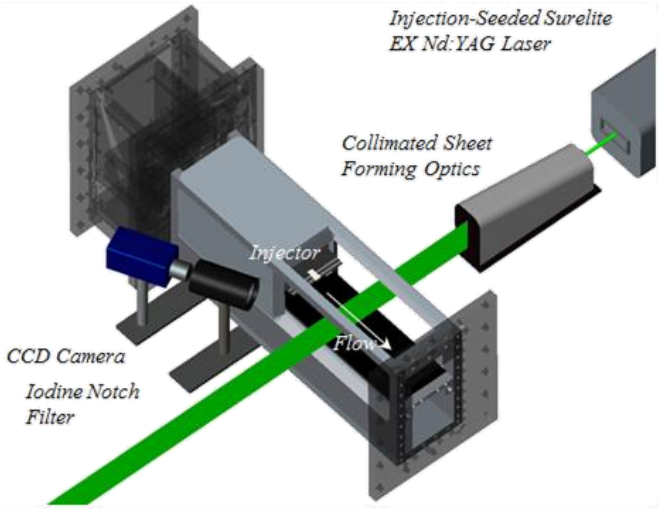

Figure 51: CAD Model of FRS Laser Setup[21]

7.2 Shock Location Using Schlieren Photography

A Schlieren image of the shock formations at the probe's inlet is needed to verify the design intention of isokinetic sampling. In addition to flow visualization, pressure measurements will be used to calculate the shock position and verify its passage into the divergent channel. Due to the very small inlet size (0.34 mm), upstream shock formations were not clearly distinguishable using a 10.1 MP digital camera with optical or digital zoom. For this reason, a pressure comparison was used to verify that the shock was swallowed. Schlieren images are also useful for ensuring that the SSWT starts, since the rake arm and instrumentation obstruct a large portion of the test section's cross-sectional area. Time-averaged Schlieren images of the probe are shown below, both inside and outside the injection plume.

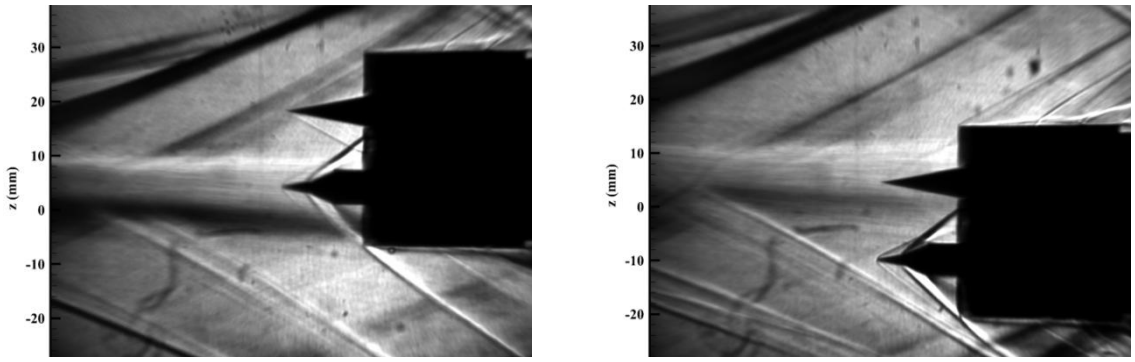

Figure 52: Probe Schlieren Images in Supersonic Flow

In the images above, it is possible to see the typical double-shock cone system that occurs from the double-divergent exterior angles of the probe. The images are sharper outside the injection plume, as air will have a steeper density gradient across a shock, which is what the Schlieren indicates. The images also clearly show starting of the tunnel, indicating that the probe itself and the new traversing system work well with this particular setup.

An independent total pressure survey was recently conducted using the new traversing system and a rake of pitot probes. This survey was conducted with the same tunnel stagnation conditions and nozzle, and it is therefore assumed that conditions are identical between that survey and the Schlieren tests in this section. A pitot probe measures stagnation pressure behind a normal shock in supersonic flow, whereas the concentration probe is designed to swallow this shock. After the inlet, the mixture expands supersonically until the massflow constraint from the throat imposes a normal shock. Since the shock inside the probe nominally occurs at a *higher* Mach number, the shock is stronger, and the expected post-shock stagnation pressure should be *lower* than a normal shock occurring at the freestream Mach number. From the aerodynamic calculations in Section 3.2, the nominal pressure ratio across the shock is calculated using the area ratio of the virtual nozzle to the inlet. The pressure ratio is determined by:

$$\frac{P_{t,2}}{P_{t,1}} = \frac{A_1^*}{\mathrm{A_t}} \quad \Rightarrow \quad \left(\frac{A_t}{A_1^*}\right)^2 = \frac{1}{M_\infty^2}\left[\frac{2}{\gamma+1}\left(1+\frac{\gamma-1}{2}M_\infty^2\right)\right]^{\frac{\gamma+1}{\gamma-1}} \tag{7.1}$$

The stagnation pressure ratio behind a normal shock is given by:

$$\frac{P_{t,2}}{P_{t,1}} = \left[\frac{(\gamma+1)M_\infty^2}{(\gamma-1)M_\infty^2+2}\right]^{\frac{\gamma}{\gamma-1}}\left[\frac{(\gamma+1)}{2\gamma M_\infty^2-(\gamma-1)}\right]^{\frac{1}{\gamma-1}} \tag{7.2}$$

For air at Mach 2.3, the total pressure ratio is predicted as 0.583 for the pitot tube, and 0.468 for the probe. Because the freestream stagnation pressure is nominally 94.6 psia for both cases, the two numbers may be compared directly. For ideal flow, the probe plenum pressure should be 83.1% of the pitot pressure. The table below summarizes the results:

Table 7: Total Pressure Measurements

	Predicted Value	Actual Value	% Error
Pitot Pressure (psia)	55.15	57.64	4.5
Probe Plenum Pressure (psia)	44.27	48.90	10.5
$P_{t2,Probe}$ / $P_{t2,Pitot}$	0.831	0.848	2.0

The nominal value of freestream stagnation pressure agrees well with the pitot measurement, within the uncertainty of the precise Mach number. Between the two instruments, the measured total pressure ratio is 0.848, compared to the nominal prediction of 0.831. These two values are in excellent agreement within the uncertainties of each measurement, which proves that the shock is indeed swallowed inside the probe. This also demonstrates that the isokinetic sampling assumption is valid, and the effects of local blunt surfaces do not significantly inhibit the incoming mixture at this downstream station for this injector configuration. Based on the probe's pressure measurement, the location of the normal shock can now be measured in the divergent channel. The image below shows where the actual shock occurred for this test compared to the nominal prediction and projected worse case, i.e. when the shock is furthest downstream. As observed in the image, these shocks remain very close to the inlet, even in the furthest downstream case.

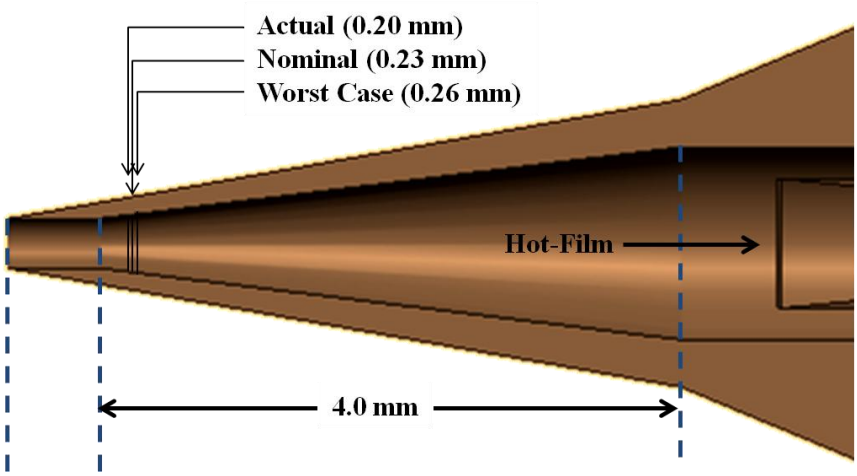

Figure 53: Shock Locations inside Divergent Channel

7.3 Mean Concentration Results

Due to unforeseen rapid temperature drops inside the probe from the cold 133 K freestream, mean concentration measurements from this probe were not attainable within the timeframe of this work. The most valuable data collected from this test campaign is the high-frequency voltage trace, to be explored in Section 7.4. The purpose of the current section is three-fold: to show partial data obtained from the probe in the SSWT, to analyze the observed rapid temperature drop inside the probe's plenum, and to present preliminary mean concentration measurements from the independent non-intrusive laser system for comparison with high-frequency CTA results in the next section.

To demonstrate the probe's ability to measure helium concentration in supersonic flow, the probe was vertically traversed across a free mixing layer of helium and air, generated from an upstream slit injector outputting ~600 SLPM of helium. This produces a helium plume which, at this particular downstream coordinate of 93 mm, spans approximately 1 cm. Although helium concentration cannot be retrieved without accurate temperature data, the probe's output indicates the presence of a plume from the pressure and CTA traces. The following plots are taken from a test run which spanned 2 cm at 0.5 mm intervals:

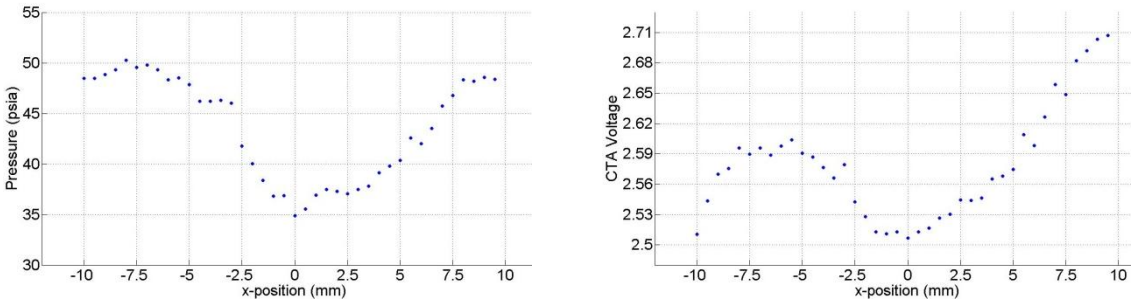

Figure 54: Pressure and CTA Voltage Traces from SSWT

Pressure decreases towards the middle of the fuel plume because the injection total pressure is only around ~15 psia, compared with the air's total pressure of ~90 psia. These data points are recorded after the co-flowing streams have mixed for ~0.20 ms, which explains why the pressure has not fully equilibrated. The CTA voltage also decreases at the center of the plume, because less pressure entails less mass flow across the filament, and thus less heat convected to the impinging mixture. Each test begins at the -10mm coordinate and ends at the +10mm coordinate approximately 12 seconds later. Total temperature inside the probe decreases substantially over the test time, and thus the CTA voltage increases towards the end of the run in order to convect more heat to the colder impinging mixture.

For an ideal instrument, the flow is adiabatic inside the plenum. Even with heat losses to the 133 K supersonic freestream, the incoming mixture reaches its total temperature soon after the normal shock, and the incoming "hot" gas is constantly being replenished and theoretically counter-acting the probe's heat loss to the freestream. This equilibrium has been observed in previous work for different probe configurations, test sections, testing times, etc. However, this probe passes very little massflow (80 mg/s) through its inlet, and the brass exterior is thin (wall thickness of 0.8 mm) with very little thermal inertia. In a steady-state condition, the brass exterior would reach an intermediate temperature between the mixture's total temperature (nominally 300 K) and the 133 K freestream. Heat fluxes are obviously much

larger for the supersonic freestream than the subsonic internal flow, due to the drastic difference in velocity. For test durations much less than the nominal 12 seconds for this setup, the brass wall's internal temperature would be only slightly affected, allowing the mixture's total temperature to be measured inside the plenum. The combination of relatively long test duration, a very thin brass wall with low thermal inertia, and a small replenishing massflow through the probe ultimately leads to a rapid drop in temperature. The latter two are both design parameters than can and should be modified for future versions of this class of instrument.

As a baseline for comparison with the high-frequency analysis, preliminary mean concentration results have been successfully obtained from the laser system recently implemented at UTA. As mentioned in the introduction, these systems are incapable of retrieving high-frequency mixing information, which is critical to detecting concentration intermittencies. Because the ongoing mixing enhancement study involves manipulation of vortical structures, the vortices' measured ability to mix the two species downstream of the injection point is critical to understanding the vortex dynamics with a binary gas mixture. For the probe, the successful installation of the new thermocouple will yield mean concentration measurements, which are useful for comparison with these laser-based results. The plot below indicates X_{He} for a mixing enhancement scheme involving a particular configuration of vortical structures.

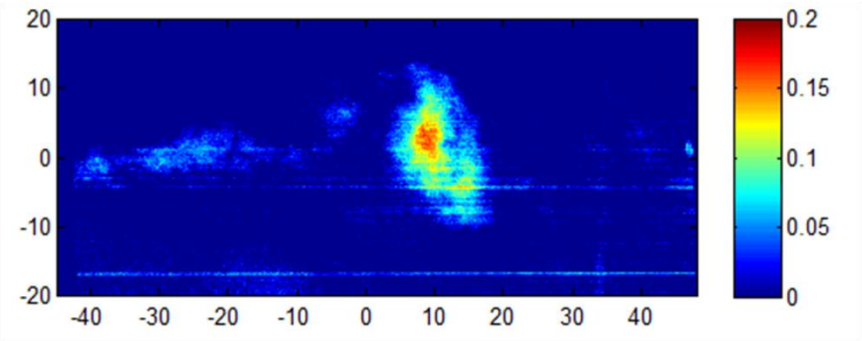

Figure 55: Mean Concentration Map from Laser System

7.4 High-Frequency CTA Voltage Results

As observed in equation (2.10), the CTA responds to changes in helium concentration as well as local pressure and temperature. In the short timespan of 100 ms per vertical coordinate when data is being collected in the SSWT, it is assumed that pressure and temperature will change negligibly. This assumption implies that the CTA voltage *only* responds to the local helium concentration impinging on the hot-film surface. In this timespan, the probe's internal volume will be flushed 35-100 times, depending on whether the incoming mixture is fast-moving helium or relatively slow air. The traces can then be quantitatively and qualitatively analyzed to interpret the presence of multiple mixtures impinging intermittently. Ultimately, this high-frequency information indicates whether a mean concentration measurement is sufficient to characterize the flow. The data acquisition system used was capable of sampling one AI channel at 200 kHz, but for several inputs, this reduced the sampling frequency to 25 kHz per channel. A future test will likely be performed for the exclusive purpose of obtaining high-frequency data where the CTA voltage will be collected at the highest possible sampling rate, and temperature and pressure will be collected in a separate command block. The plots on the next few pages show the CTA voltage trace and PDFs from a 4 cm vertical traverse across the mixing layer at selected points, from top to bottom:

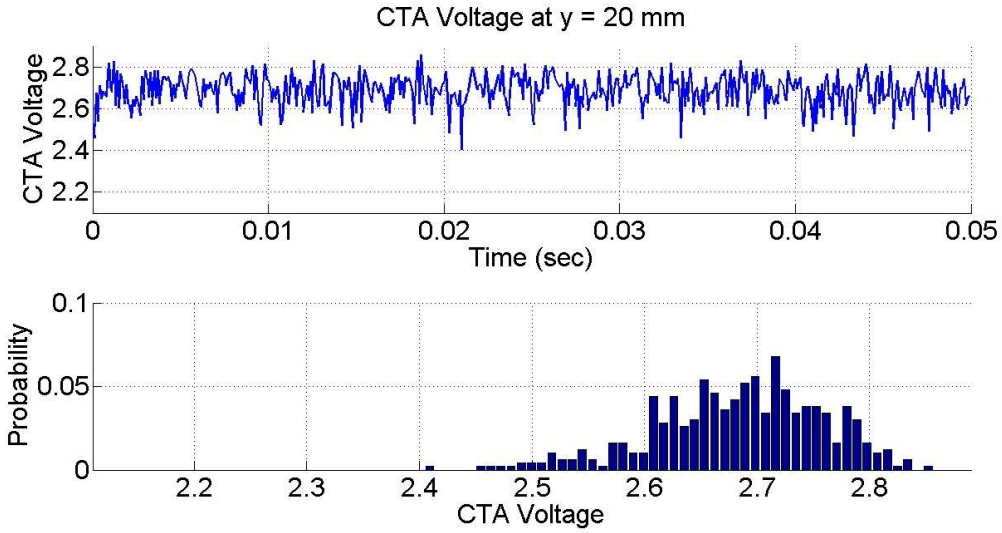

Figure 56: CTA Voltage at y = 20 mm

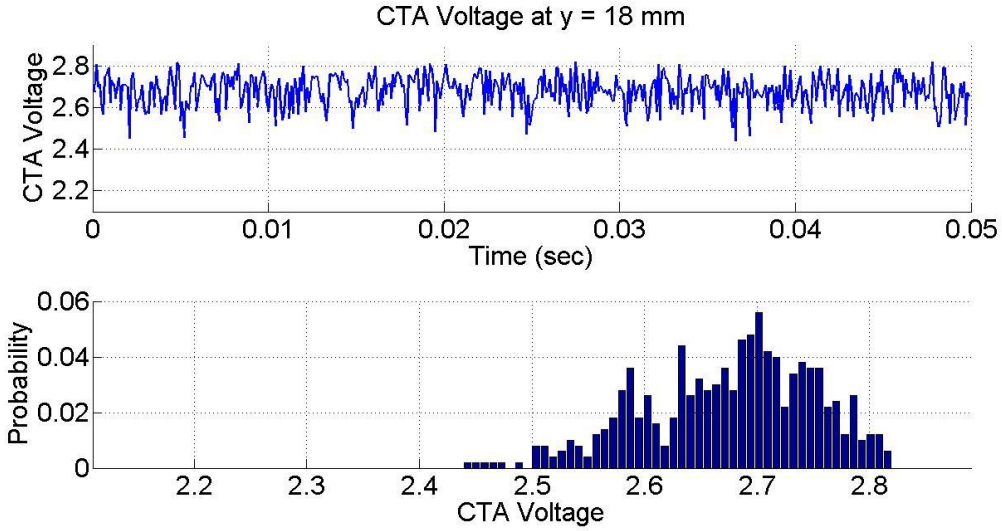

Figure 57: CTA Voltage at y = 18 mm

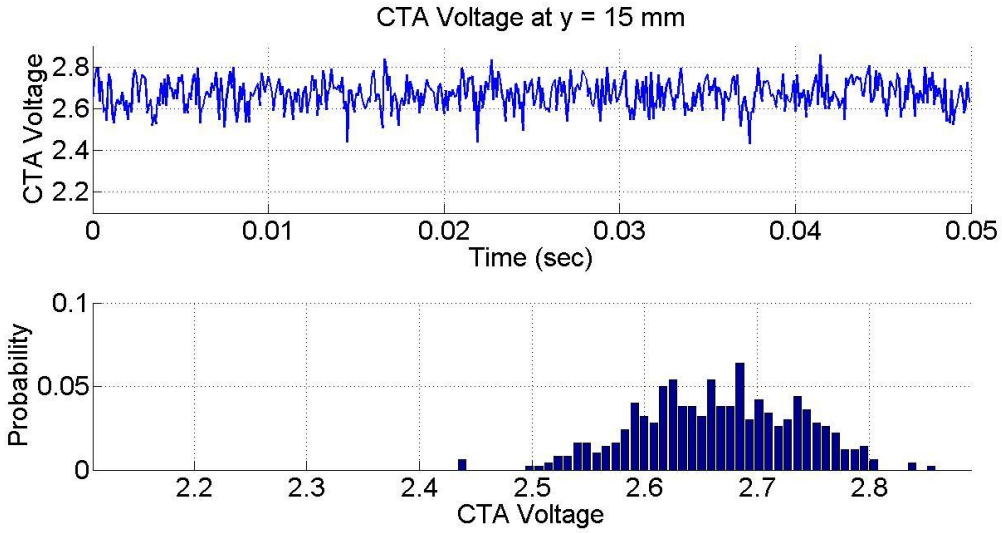

Figure 58: CTA Voltage at y = 15 mm

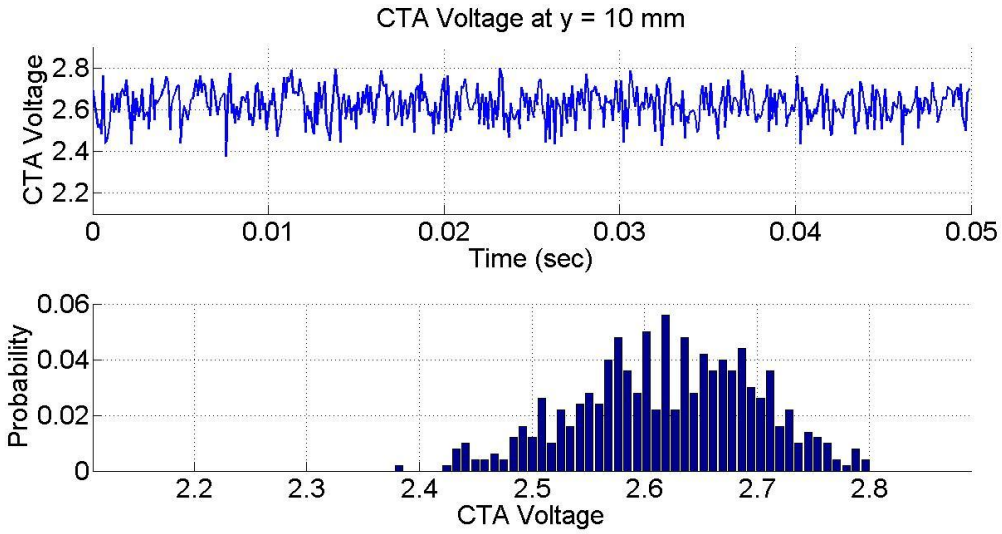

Figure 59: CTA Voltage at y = 10 mm

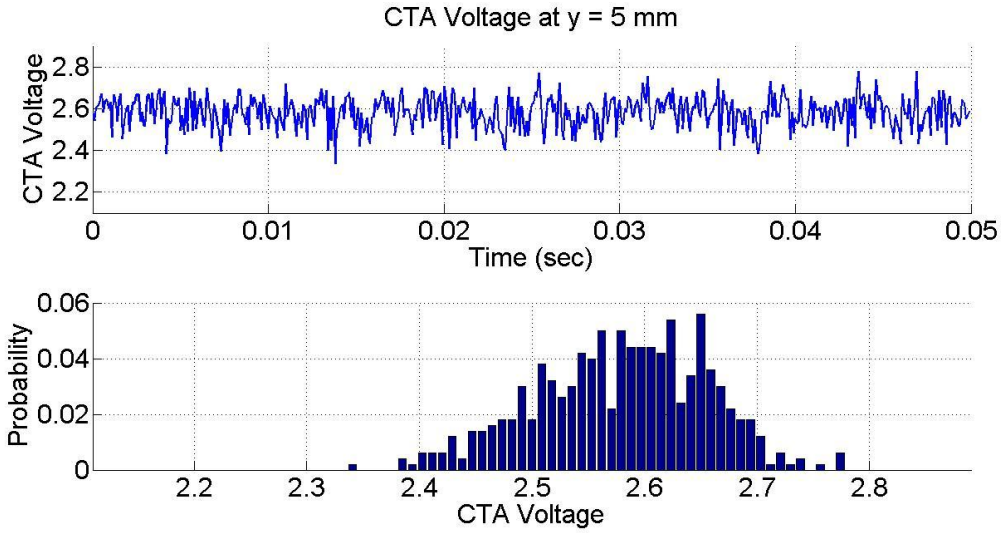

Figure 60: CTA Voltage at y = 5 mm

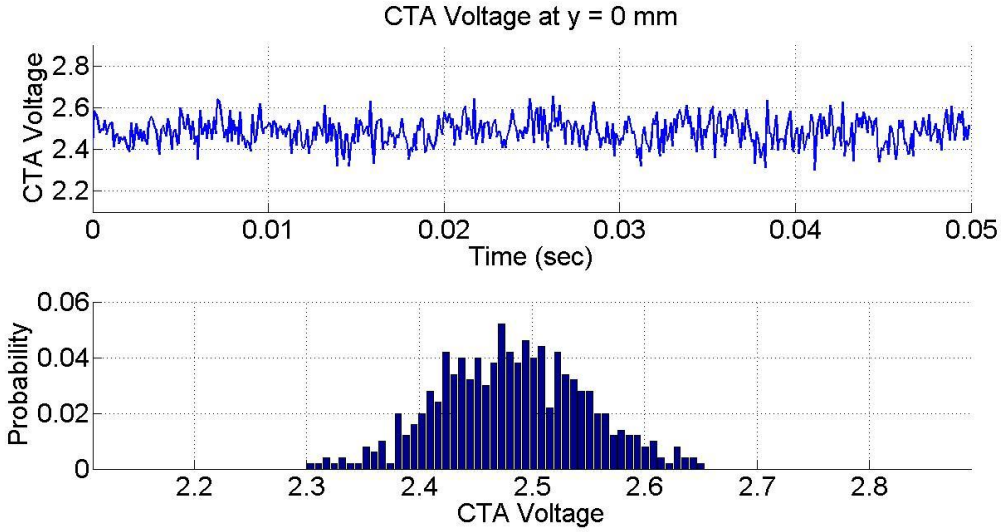

Figure 61: CTA Voltage at y = 0 mm

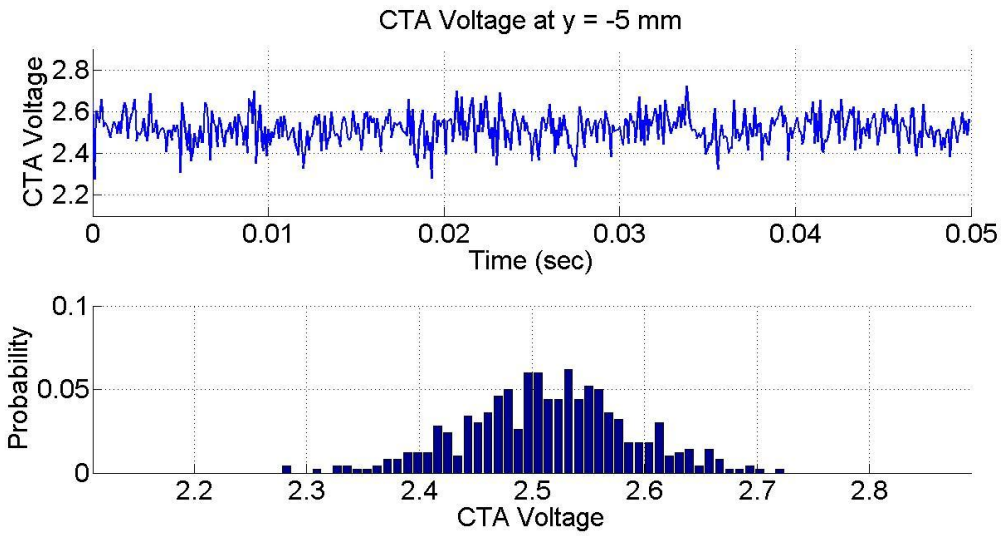

Figure 62: CTA Voltage at y = -5 mm

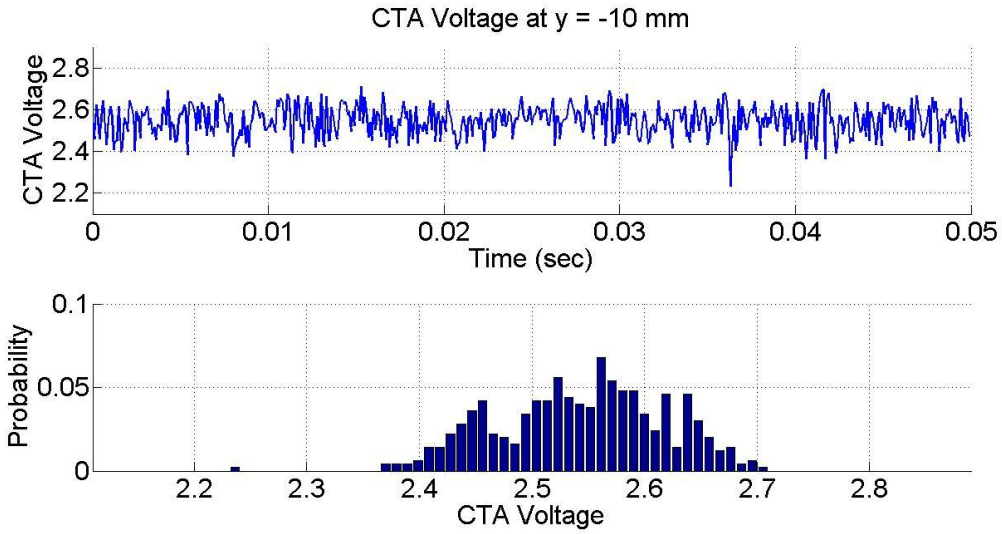

Figure 63: CTA Voltage at y = -10 mm

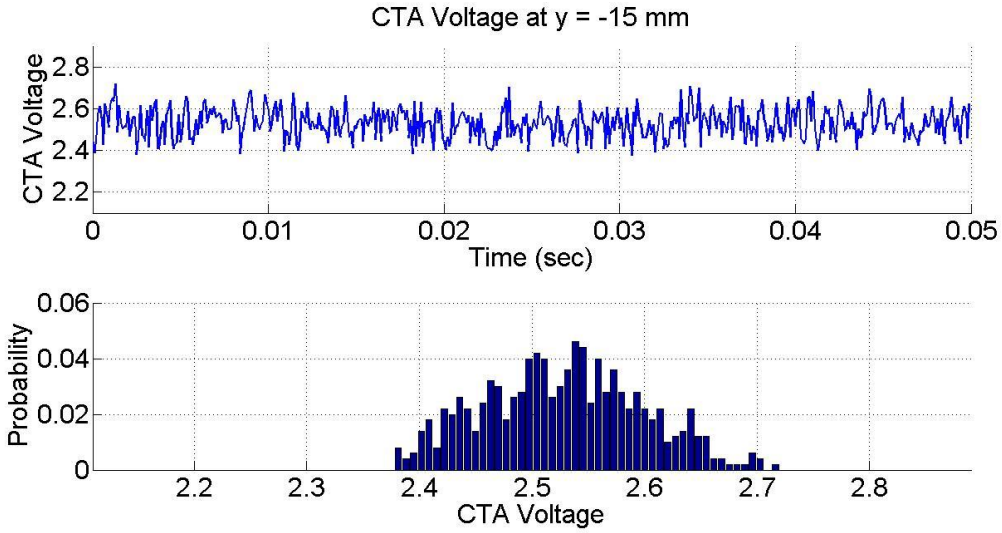

Figure 64: CTA Voltage at y = -15 mm

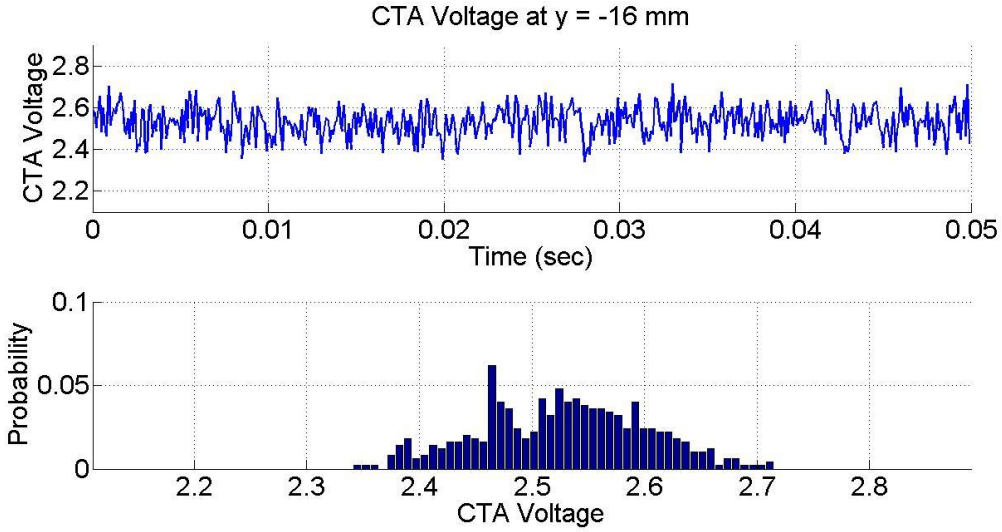

Figure 65: CTA Voltage at y = -16 mm

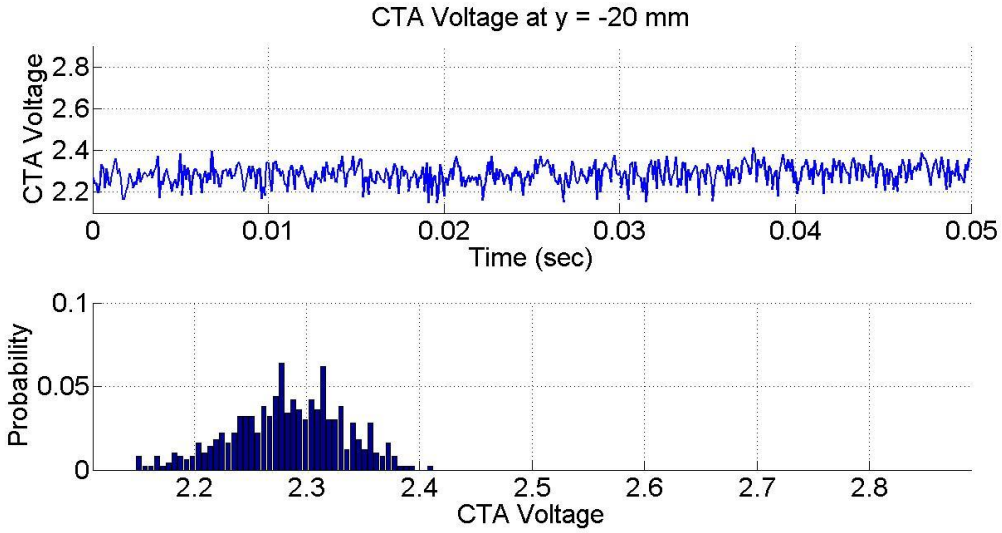

Figure 66: CTA Voltage at y = -20 mm

In the plots above, the tallest peak of the PDF is referred to as the *most probable* CTA voltage, i.e. the voltage corresponding to the helium concentration that impinges on the hot-film *most often*, since X_{He} will fluctuate locally inside the probe due to internal mixing effects as discussed in Section 6.3. The nominal PDF for a uniform impinging mixture has a Gaussian distribution, as observed in most of the plots above, with the fluctuations due to turbulence. Refer to Figure 63 above; there is a somewhat distinguishable second peak that occurs in the PDF. This particular coordinate is at the edge of the helium plume, where two mixtures are likely impinging intermittently. The same trend can be seen in Figure 57 and Figure 65, although the secondary peaks in these PDFs are more likely due to the CTA's response to shock oscillations that alternate the pressure inside the probe. Refer again to Figure 40c in Section 6.1; inside the calibration tank, the two species are clearly distinguished, likely due to intermittently leaking air or stratification. This clear separation was not observed (or expected) in the SSWT, because the two species mix in the freestream, through the normal shock, and inside the probe.

Several runs were performed in which the probe was traversed across the free mixing layer. The run for which results are shown above was chosen because it best illustrates certain

trends which can be correlated to incoming structures of air and helium. For all of the runs performed in this survey, helium was injected at ~600 SLPM in a Mach 2.3 co-flowing stream of air. The maximum time-averaged concentration inside the plume at this downstream location is expected to be approximately 5-10% molar fraction of helium, which was determined from independent laser-based measurements. Using the calibration output, the deviation of voltage from 0% to 10% helium varies from 60 to 77 mV, depending on the pressure. Most of the PDFs have a 95% confidence interval of +/- 100 mV. Therefore the *maximum* expected fluctuations of CTA voltage are still bound within the nominal distribution, demonstrating quantitatively that drawing conclusions on the mixture intermittency based on these second ambiguous peaks is unreliable for this particular setup.

The purpose of these tests was two-fold: to obtain mean concentration measurements as well as identify any mixture intermittencies at each vertical coordinate from the high-frequency CTA voltage trace. These are two distinct outcomes from the same instrument, and both use the hot-film and CTA system as the primary indicator. However, the simultaneous acquisition of these two results presents an interesting challenge. Recall from Section 5.1 that the CTA is *tunable* to a specific hot-film circuit by adjusting trim and gain, where a successful square wave test yields low pulse amplitude (less noise) and narrow pulse width (faster response). Mean concentration measurements do not rely on a fast response, and so the preferred configuration would be to minimize noise for more accurate CTA voltage measurements. Conversely, high-frequency measurements demand a fast response to instantaneous changes in the mixture impinging on the hot-film, and reduced noise is preferable but not essential. In general, reducing the CTA noise decreases the frequency response, and vice versa. Finding a balance between minimal noise and a fast response is not an intuitive trade-off, particularly if both are required for separate outputs. Ultimately, this probe will likely need to be re-tuned and the signal carefully conditioned to achieve a tolerable amount of noise at the desired frequency response.

Chapter 8

Conclusion

Due to short fuel residence times in scramjet combustors, combustion is limited by the mixing of fuel and air. Expanding on previous work, an instrument has been designed, fabricated, and tested which measures mean concentration and gives insight into the high-frequency concentration fluctuations which occur in these complex supersonic flows. This high-frequency data is not attainable by other techniques such as LIF or mass spectroscopy in complex supersonic flows.

This probe operates by exploiting the difference between the thermodynamic properties of two species through independent massflow measurements and calibration. The probe samples isokinetically from the flowfield of interest and the helium concentration may be uniquely determined by a hot-film attached to an anemometer (CTA) and measured stagnation conditions. The final design has a diameter of 0.25”, is only 2.22” long, and was machined and assembled without excessive cost. Difficulties were experienced with maintaining a vacuum through a thin line, but this was overcome with a quick modification after assembly.

A calibration facility was built and implemented specifically for this probe, as well as a data acquisition system and data reduction code. The overall accuracy of the probe, both from calibration error and instrument error, was evaluated to be typically 2.7% molar fraction of helium. The frequency response of mean concentration measurements is mainly limited by the internal volume of the probe, and is estimated at 103 Hz. High-frequency measurements are attained from the CTA voltage trace, and were measured to be around 60 kHz.

PDFs of the CTA voltage were analyzed to determine some limited mixing characteristics of the two species at high frequencies. These measurements are ultimately a time-area-averaged concentration value, which can be distorted by continued mixing inside the probe downstream of the sampling point.

The probe went through two series of tests; the first test series used Schlieren photography and verified that the probe sampled the supersonic flowfield isokinetically. The second test series involved traversing the probe across a free mixing layer of air and helium, to obtain both mean concentration and high-frequency measurements. An installation error temporarily prevented successful mean concentration measurements, although plans to correct this error and re-test have been finalized at the time of this writing. High-frequency measurements of the simple mixing layer indicated no significant deviations from a nominal, turbulent mixture at each point in the survey, as expected.

The probe is minimally intrusive, has accuracy comparable to its predecessors, has an improved frequency response for mean concentration measurements from previous designs, and samples from a very small area in the flowfield. The probe will be used to assess the mixedness of complex supersonic flowfields of air and helium for prototype injection schemes currently being developed at UTA. The understanding and analysis of high-frequency PDFs of CTA voltage will be extended to PDFs of mixing. It has been demonstrated that mean concentration measurements are not generally adequate to temporally characterize the mixture in complex supersonic flows. Therefore for flowfields with predicted or known concentration intermittencies, mean concentration measurements should always be accompanied by an analysis of the PDF, thereby presenting a statistical concentration value instead of a deterministic one.

8.1 Performance Specifications and Comparison

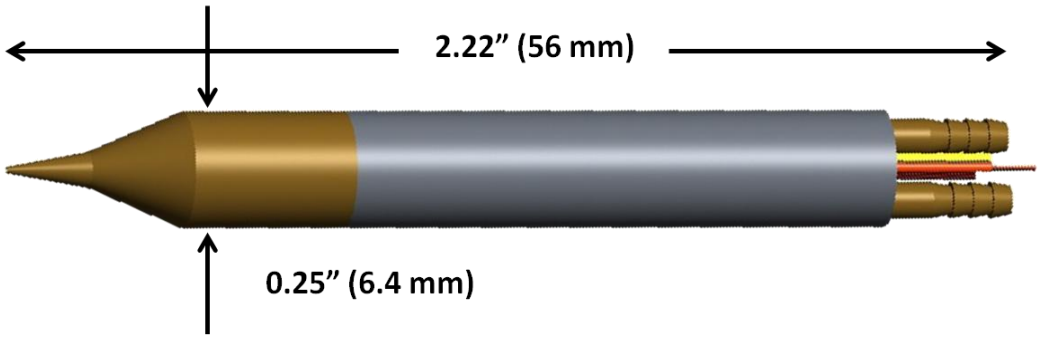

Figure 67: Bulk Probe Dimensions

Table 8: Probe Performance Specifications

Mean X_{He} Frequency Response	103 Hz (Min)
CTA Frequency Response	60 kHz
X_{He} Accuracy	2.7% Typ., 7.3% (Max)
Inlet Diameter	0.0135” (0.343 mm)
Hot-film Diameter (Characteristic Measurement Length)	0.0010” (25 µm)
Freestream Mach Number Range	0 - 3.40 Max.
Internal Pressure Limits (from Transducer)	0 - 100 psia Max.
Internal Temperature Limits (from Transducer)	-55 °C to 120 °C Max.

Table 9: Supersonic Probe Comparisons

Designer		Ninneman and Ng	Xillo	Maddalena	Wiswall
Year		1989	1998	2007	2013
Frequency Response		10 Hz	2.5 kHz	3 Hz	103 Hz
X_{He} Accuracy	Typ. %	2%	5%	2%	3%
	Max. %	Not Given	27%	7%	7%
Inlet Diameter		0.011”	0.086”	0.025”	0.014”
Maximum Mach		2.5	3.25	4.0	3.25
Integrated Temp. Measurement		None	Hot-film	Thermo-couple	Thermo-couple
Bulk Diameter		0.25”	0.25”	0.31”	0.25”

8.2 Recommendations for Future Designs

Some ideas for design improvement are presented below. It is first recommended that a better strategy for the wiring and tubing exit be conceived, to avoid problems with the vacuum line by using larger tubing. Second, tightly bounding the instruments in an enclosed space improved the frequency response, but made post-assembly repairs to the probe very difficult. Leak prevention and thin wire protection was a very delicate and time-consuming task in the limited workspace. Third, all three instruments should have their respective sensing elements in the same plane. This ensures that the measured stagnation properties in the downstream plenum are the same as those impinging on the hot-film, which is implicitly assumed in the governing equation. This placement should not, however, come at the cost of reduced hot-film impingement velocity, which improves high-frequency measurements. Finally, a thicker and more insulating material (e.g. stainless steel) would prevent excessive heat losses to the cold freestream and yield test data closer to room temperature, where calibration is performed.

Appendix A

MatLab Scripts

```
% Variables (specific to 1 probe)
R_series=.75; % Series bridge resistance
R_film=6.65; % Hot film "hot" resistance
T_film=273.15+224; % Constant hot-film temperature in Kelvin
l_film=250E-6; % Hot film sensing length in meters
d_film=25.4E-6; % Diameter of the hot-film in meters
d_throat=0.3429E-3; % Diameter of the throat(s) in meters
n_throats=1; % The number of throats
d_HF=1.3208E-3; % Hot-film plane diameter in meters
A_star=n_throats*(d_throat/2)^2*pi; % Throat area in m^2
A_HF=(d_HF/2)^2*pi; % HF area in m^2
R_Uni=8314.4; % Universal gas constant in J/kg*K
M_air=28.97; % molecular weight of air
M_He=4.0026; % molecular weight of helium
N1=(R_series+R_film)^2*pi*l_film/R_film; % Intermediate variable
        N2=d_film*A_star/A_HF; % Intermediate variable

% Evaluate thermodynamic properties
Cp_air=1004.5;
Cp_He=5193.0;

k_air=1.61344*10^-4
+8.89970*10^-5*T
+3.85599*10^-8*T.^2
-2.39332*10^-10*T.^3
+3.48891*10^-13*T.^4
-1.84858*10^-16*T.^5;
k_He=4.33185*10^-2
+1.23854*10^-4*T
+2.77149*10^-6*T.^2
-1.11774*10^-8*T.^3
+1.81601*10^-11*T.^4
-1.03892*10^-14*T.^5;

mu_air=-1.31554*10^-6
+9.53265*10^-8*T
-1.50660*10^-10*T.^2
+2.41737*10^-13*T.^3
-2.58576*10^-16*T.^4
+1.26849*10^-19*T.^5;
mu_He=-4.56080*10^-6
+2.05152*10^-7*T
-8.89707*10^-10*T.^2
+2.41714*10^-12*T.^3
-3.2072*10^-15*T.^4
+1.6306*10^-18*T.^5;

% Binary gas mixture calculations
```

```
M_mix=X_air*M_air+X_He*M_He;
R_mix=R_Uni./M_mix;
Cp_mix=X_air.*Cp_air.*(M_air./M_mix)+X_He.*Cp_He.*(M_He./M_mix);
gamma=Cp_mix./(Cp_mix-R_mix);
C_mix=sqrt(gamma./R_mix).*(2./(gamma+1)).^((gamma+1)./(2*(gamma-1)));

% mu and k of the mixture
Phi_mu_air_He=(1+(mu_air./mu_He).^0.5.*(M_He./M_air).^0.25).^2 ...
./(4*2^0.5.*((1+M_air./M_He).^0.5));
Phi_mu_He_air=(1+(mu_He./mu_air).^0.5.*(M_air./M_He).^0.25).^2 ...
./(4*2^0.5.*((1+M_He./M_air).^0.5));
Phi_k_air_He=(1+(k_air./k_He).^0.5.*(M_He./M_air).^0.25).^2 ...
./(4*2^0.5.*((1+M_air./M_He).^0.5));
Phi_k_He_air=(1+(k_He./k_air).^0.5.*(M_air./M_He).^0.25).^2 ...
./(4*2^0.5.*((1+M_He./M_air).^0.5));

mu_mix_1=mu_air./(1+X_He./X_air.*Phi_mu_air_He);
mu_mix_2=mu_He./((1+X_air./X_He).*Phi_mu_He_air);
k_mix_1=k_air./(1+(X_He./X_air).*Phi_k_air_He);
k_mix_2=k_He./(1+X_air./X_He.*Phi_k_He_air);
mu_mix=mu_mix_1+mu_mix_2;
        k_mix=k_mix_1+k_mix_2;
```

A.2 Probe Calibration Code

```
% John D. Wiswall
% Probe Calibration Code [ProbeCal.m]
% Created Jan 24, 2012

% Load data file & define nominal calibration points
load('080113 Full.mat','Raw_Data');
P_array=(20:5:60); % Nominal pressures in data file
X_array=(0:0.1:1); % Concentrations in data file
P_tol=0.5; % Pressure tolerance
delP=P_array(2)-P_array(1); % Pressure step

% Filter out data outside pressure tolerances
Good_Data=zeros(size(Raw_Data)); % Pre-allocate the array
i1=0;
for i2=length(Raw_Data):-1:1
   P_dev1=mod(Raw_Data(i2,3),delP);
   P_dev2=min(P_dev1,delP-P_dev1);
   if P_dev2 < P_tol
      i1=i1+1;
      Good_Data(i1,:)=Raw_Data(i2,:);
   end
end
if i1~=size(Good_Data,1)
```

```
    Good_Data(i1:1:size(Good_Data,1),:)=[]; % Remove blank rows
end

% Sort and extract individual data for analysis
Sorted_Data=sortrows(Good_Data,[2 3]);
Time=Sorted_Data(:,1);
X_He=Sorted_Data(:,2);
P=Sorted_Data(:,3);
T=Sorted_Data(:,4);
V=Sorted_Data(:,5);
X_air=1-X_He;

% Calculation of Reynolds and Nusselt Number
N3=k_mix.*(T_film-T);
N4=6895*P.*C_mix./(mu_mix.*sqrt(T));
Re=N2.*N4;
Nu=V.^2./(N1.*N3);

% Compile all data into 1 array used to find a & b.
Compiled_Data=zeros(length(P),7);
for i3=1:size(P,1)
    Compiled_Data(i3,:)=[X_He(i3),P(i3),T(i3),V(i3),P_tol,Re(i3),Nu(i3)];
end

% This routine groups data into average points
Final_Data=zeros(Length(X_array)*Length(P_array),7);
N_Points=zeros(Length(X_array),Length(P_array));
Mat=zeros(Length(X_array),Length(P_array));
i4=0; % Index for number of data points
i5=0; % Index for Final_Data
i6=1; % Index for Compiled_Data
X_stop=false;
P_bound=true;
X_bound=true;
sum10=zeros(1,7);
mag=0; % Total weight for each station
for i385=1:1:Length(X_array) % Sweep X_He
    if X_stop == true; break; end
    while X_bound==true % While at current X_He
        if X_stop == true; break; end
        if abs(X_He(i6)-X_array(i385))<=10^-5 % Still in current X_He
            if X_stop == true; break; end
            for i9=1:1:Length(P_array) % Sweep Pressure
                if X_stop == true; break; end
                while P_bound==true % While at current pressure
                    if X_stop == true; break; end
                    if abs(P(i6)-P_array(i9))<=P_tol % Still in current Pressure
                        sum10=sum10+Compiled_Data(i6,:);
                        i4=i4+1;
                        i6=i6+1;
```

```
                else
                    P_bound=false; % Outside current data range
                end
                if P_bound==false && i4~=0 && i6 ~= length(P)+1 % If N ~=0
                    i5=i5+1;
                    Final_Data(i5,:)=sum10/i4;
                    N_Points(i385,i9)=i4;
                    Mat(i385,i9)=1;
                    i4=0;
                    sum10=zeros(1,7);
                    mag=0;
                end
                if i6==size(Compiled_Data,1)+1 % If this is the last data point
                    if i4~=0 % Record last data point if data was collected
                        i5=i5+1;
                        Final_Data(i5,:)=sum10/i4;
                        N_Points(i385,i9)=i4;
                        Mat(i385,i9)=1;
                    end
                    X_stop=true;
                    break;
                end
            end
            P_bound=true;
        end
    else
        X_bound=false;
    end
  end
  X_bound=true;
end

Final_Data(sum(sum(Mat))+1:size(Final_Data,1),:)=[]; % Remove blank rows
Re_new=Final_Data(:,6); % Averagred Re
Nu_new=Final_Data(:,7); % Averaged Nu

% Intermediate values for a & b calculation
ln2=log(Re_new);
ln3=log(Nu_new);
ln1=ln2.*ln3;
ln4=ln2.^2;

% The calibration constants are found 1 concentration at a time.
Cal_Const=zeros(Length(X_array),3); % Pre-allocate the file
Cal_Const(1:Length(X_array),1)=transpose(X_array);
N=zeros(Length(X_array),1);
i17=0; % Data index
for i13=1:1:Length(X_array)
  N(i13)=sum(Mat(i13,:));
  if N(i13)~=0 % If data exists for this X_He
```

```
        sum1=0;
        sum2=0;
        sum3=0;
        sum4=0;
        for i16=1:1:N(i13)
            i17=i17+1;
            sum1=sum1+ln1(i17);
            sum2=sum2+ln2(i17);
            sum3=sum3+ln3(i17);
            sum4=sum4+ln4(i17);
        end
        num1=sum1-(1/N(i13))*sum2*sum3;
        den1=sum4-(1/N(i13))*sum2*sum2;
        b=num1/den1;
        a=exp((1/N(i13))*(sum3-sum2*b));
        Cal_Const(i13,2)=a;
        Cal_Const(i13,3)=b;
    else
        Cal_Const(i13,2)=NaN;
        Cal_Const(i13,3)=NaN;
    end
end

% Calculate nominal deviation from Nu-Re curve
i39=0;
for i31=1:1:length(X_array)
    for i32=1:1:length(P_array)
        if N_Points(i31,i32)~=0
            i39=i39+1;
            dNu_nom1(i39)=Nu_new(i39)-Nu_Cal(i39);
            if i31==1
                dNu1(i39)=Nu_Cal(i39)-Cal_Const(i31+1,2)*Re_Cal(i39)^Cal_Const(i31+1,3);
                nomError(i31,i32)=dNu_nom1(i39)/dNu1(i39)*10;
            elseif i31==length(X_array)
                dNu2(i39)=Cal_Const(i31-1,2)*Re_Cal(i39)^Cal_Const(i31-1,3)-Nu_Cal(i39);
                nomError(i31,i32)=dNu_nom1(i39)/dNu2(i39)*10;
            else
                dNu1(i39)=Nu_Cal(i39)-Cal_Const(i31+1,2)*Re_Cal(i39)^Cal_Const(i31+1,3);
                dNu2(i39)=Cal_Const(i31-1,2)*Re_Cal(i39)^Cal_Const(i31-1,3)-Nu_Cal(i39);
                if dNu_nom1(i39)<=0
                    nomError(i31,i32)=dNu_nom1(i39)/dNu1(i39)*10;
                else
                    nomError(i31,i32)=dNu_nom1(i39)/dNu2(i39)*10;
                end
            end
        else
            nomError(i31,i32)=NaN;
        end
    end
end
```

```
% Calculate fixed and random errors
i42=1;
T_nom=300;
dT=0.1;
dV=0.0001;
dP=0.01;
X_tol=0.0001;
for i31=1:1:length(X_array)
   for i32=1:1:length(P_array)
      if N_Points(i31,i32)~=0
         i39=0;
         T_rand=1.96*std(T(i42:i42+N_Points(i31,i32)-1));
         T_fixed=T_accuracy+T_rand;
         P_rand=1.96*std(P(i42:i42+N_Points(i31,i32)-1));
         P_fixed=P_accuracy+P_rand;
         i42=i42+N_Points(i31,i32);
         V_lower=2;
         V_upper=4;
         V_found=false;
         while V_found == false
            i39=i39+1;
            V_guess=0.5*(V_lower+V_upper);
            X_guess=findX(P_array(i32),T_nom,V_guess,2);
            if X_guess > X_array(i31)
               V_upper=V_guess;
            else
               V_lower=V_guess;
            end
            if abs(X_guess-X_array(i31))<X_tol
               V_found=true;
            end
         end
         X_pert_T=findX(P_array(i32),T_nom+dT,V_guess,2);
         T_sens(i31,i32)=(X_pert_T-X_array(i31))/dT;
         TError(i31,i32)=100*T_sens(i31,i32)*T_fixed;
         X_pert_P=findX(P_array(i32)+dP,T_nom,V_guess,2);
         P_sens(i31,i32)=(X_pert_P-X_array(i31))/dP;
         PError(i31,i32)=100*P_sens(i31,i32)*P_fixed;
         X_pert_V=findX(P_array(i32),T_nom,V_guess+dV,2);
         V_sens(i31,i32)=(X_pert_V-X_array(i31))/dV;
         instrError(i31,i32)=sqrt(PError(i31,i32)^2+TError(i31,i32)^2);
      else
         instrError(i31,i32)=NaN;
      end
   end
end
```

A.3 SSWT Data Reduction Code

```
% John D. Wiswall
% Tunnel Data Reduction Code [SSWT_1-dimensional.m]
% Created Tues, May 15, 2012

% User Inputs
x_array=transpose(-20:1:20);
N_points=2000;
N_usable=1500;

% Load calibration file
load('041513 Half Cal.mat','NuRe_Cal');
X_He=NuRe_Cal(:,1);
a=NuRe_Cal(:,2);
b=NuRe_Cal(:,3);

% Load raw data file
load('SSWT 4 filtered.mat','Raw_Data');
i58=1;
for i57=1:N_points:size(Raw_Data,1)-N_points+1
    Raw_Data(i57+1:i57+N_points-1,4)=Raw_Data(i57,4);
    Raw_Data(i57+1:i57+N_points-1,5)=Raw_Data(i57,5);
end

% Filter out unusable points
i93=1;
New_Data=zeros(size(Raw_Data,1)*(N_usable/N_points),5);
for i57=1:N_points:size(Raw_Data,1)-N_points+1
    New_Data(i93:i93+N_usable-1,:)=
    Raw_Data(i57+(N_points-N_usable):i57+N_points-1,:);
    i93=i93+N_usable;
end
Sorted_Data=sortrows(New_Data,[4 5]);

% Extract parameters from the Good_Data file
P=Sorted_Data(:,1); % psia
T=Sorted_Data(:,2); % Kelvin
V=Sorted_Data(:,3); % Volts
x=Sorted_Data(:,4); % mm

% Calculate an average value
P_avg=zeros(length(x_array),1);
V_avg=zeros(length(x_array),1);
T_avg=zeros(length(x_array),1);
i52=0;
for i48=1:1:length(x_array)
    sumP=0;
    sumV=0;
    sumT=0;
```

```
    i51=0;
    for i50=1:1:N_usable
        i52=i52+1;
        i51=i51+1;
        sumP=sumP+P(i52);
        sumV=sumV+V(i52);
        sumT=sumT+T(i52);
    end
    P_avg(i48)=sumP/i51;
    V_avg(i48)=sumV/i51;
    T_avg(i48)=sumT/i51;
end

% Calculate concentration by interpolating Nu
X=zeros(length(x_array),1);
for i38=1:1:size(x_array)
    Re=zeros(11,1);
    Nu=zeros(11,1);
    Nu_Cal=zeros(11,1);
    for i39=1:1:size(X_He,1)
        % Calculation of Reynolds and Nusselt Number
        N3=k*(T_film-T_avg(i38)*Tratio); % Intermediate variable
        N4=6895*P_avg(i38)*C_mix/(mu*sqrt(T_avg(i38))); % Intermediate variable
        Re(i39)=N2*N4; % Reynolds number
        Nu(i39)=V_avg(i38)^2/(N1*N3); % Nusselt number
        Nu_Cal(i39)=a(i39)*Re(i39)^b(i39);
    end
    X_lower=find(Nu>Nu_Cal,1,'last');
    X_upper=find(Nu<Nu_Cal,1,'first');
    if isempty(X_lower)
        dNu=Nu_Cal(2)-Nu_Cal(1);
        if Nu_Cal(1)-Nu(1)<dNu
            X(i38)=0;
        else
            X(i38)=NaN;
        end
    elseif isempty(X_upper)
        dNu=Nu_Cal(11)-Nu_Cal(10);
        if Nu(11)-Nu_Cal(11)<dNu
            X(i38)=1;
        else
            X(i38)=NaN;
        end
    else
        dNu_Cal=Nu_Cal(X_upper)-Nu_Cal(X_lower);
        dNu1=Nu(X_lower)-Nu_Cal(X_lower);
        dNu2=Nu_Cal(X_upper)-Nu(X_upper);
       X(i38)=dNu1/(dNu1+dNu2)*0.1+X_He(X_lower);
    end
end
```

Appendix B

Technical Drawings

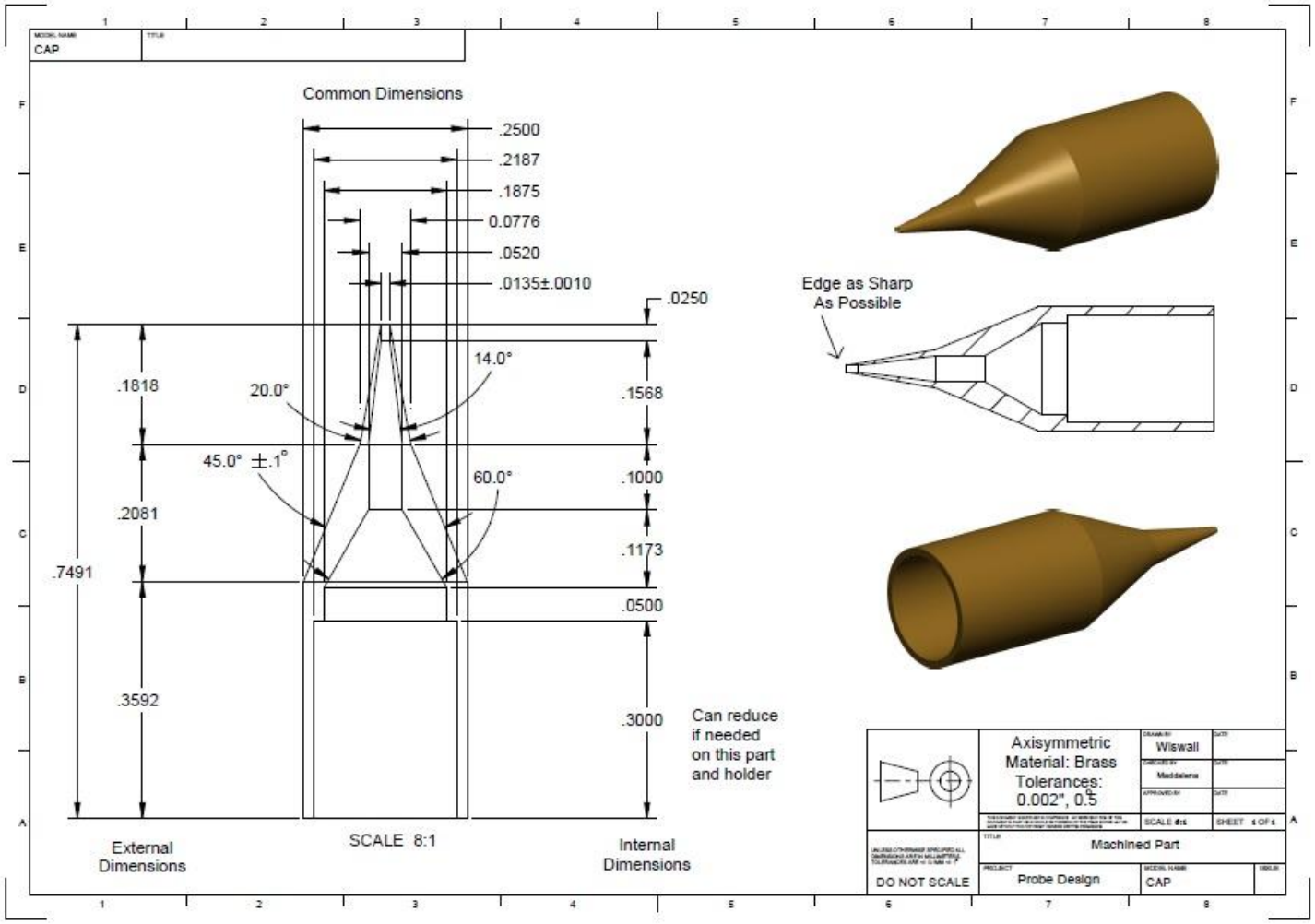

Figure 68: Cap Geometry

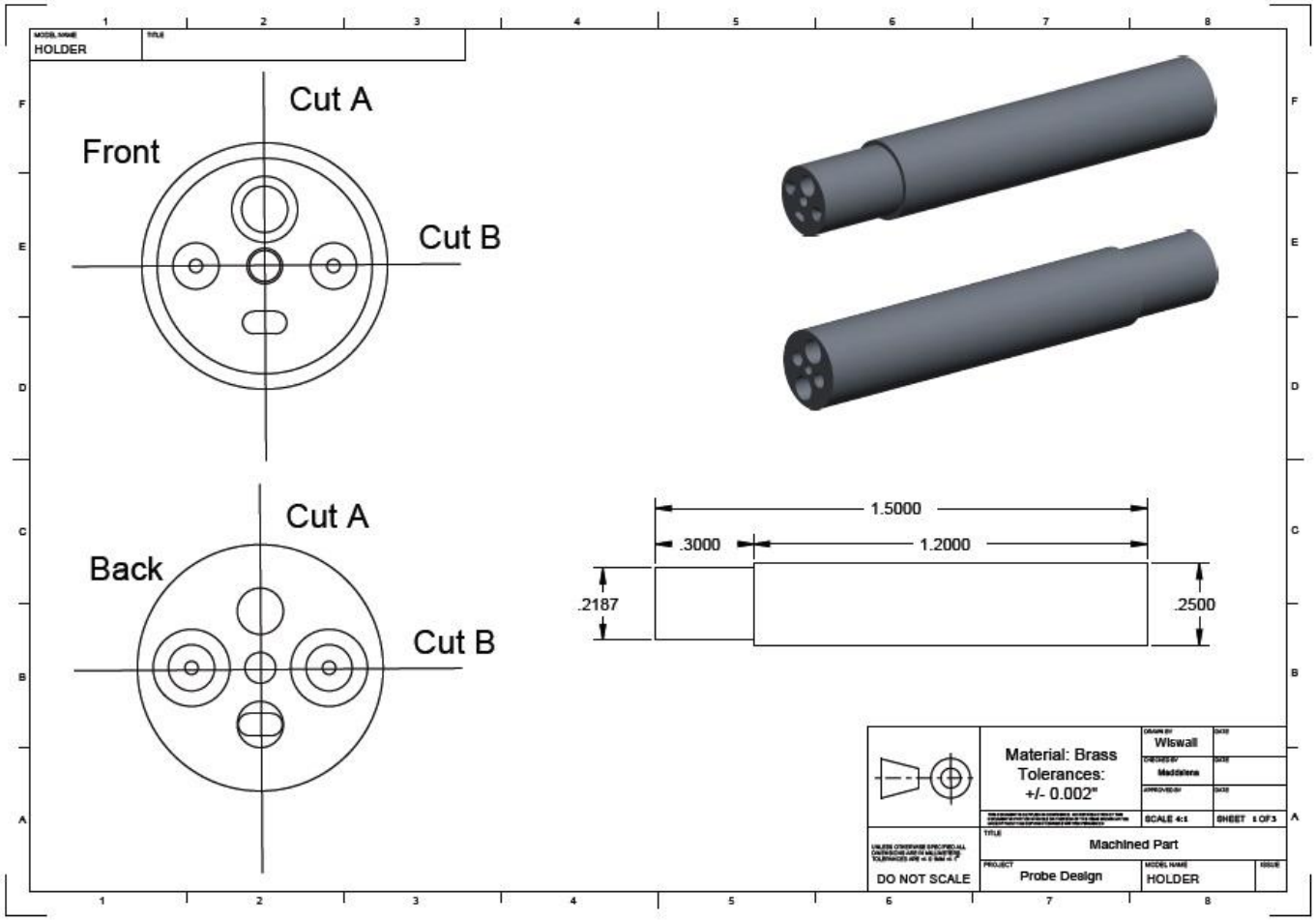

Figure 69: Holder Geometry 1

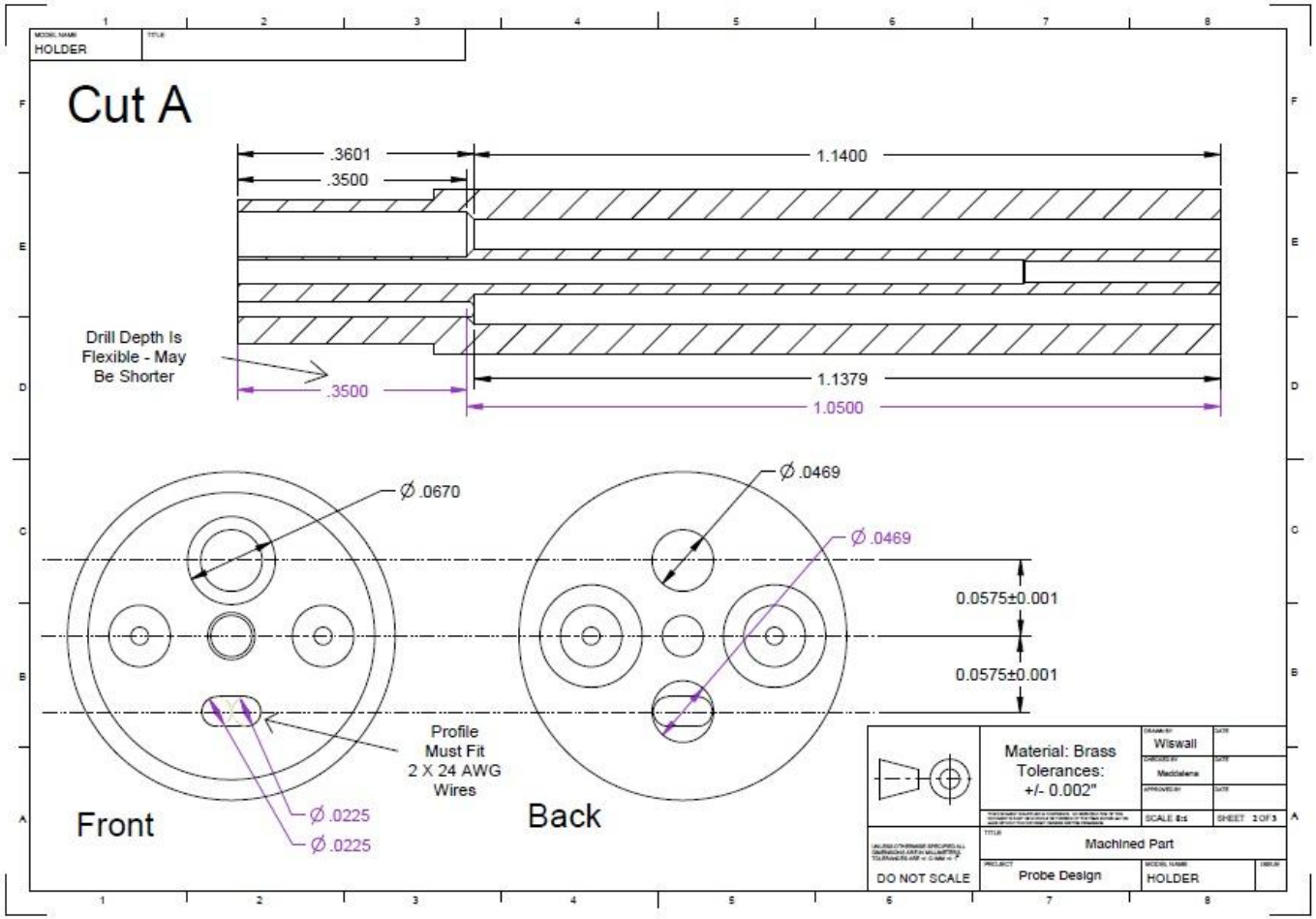

Figure 70: Holder Geometry 2

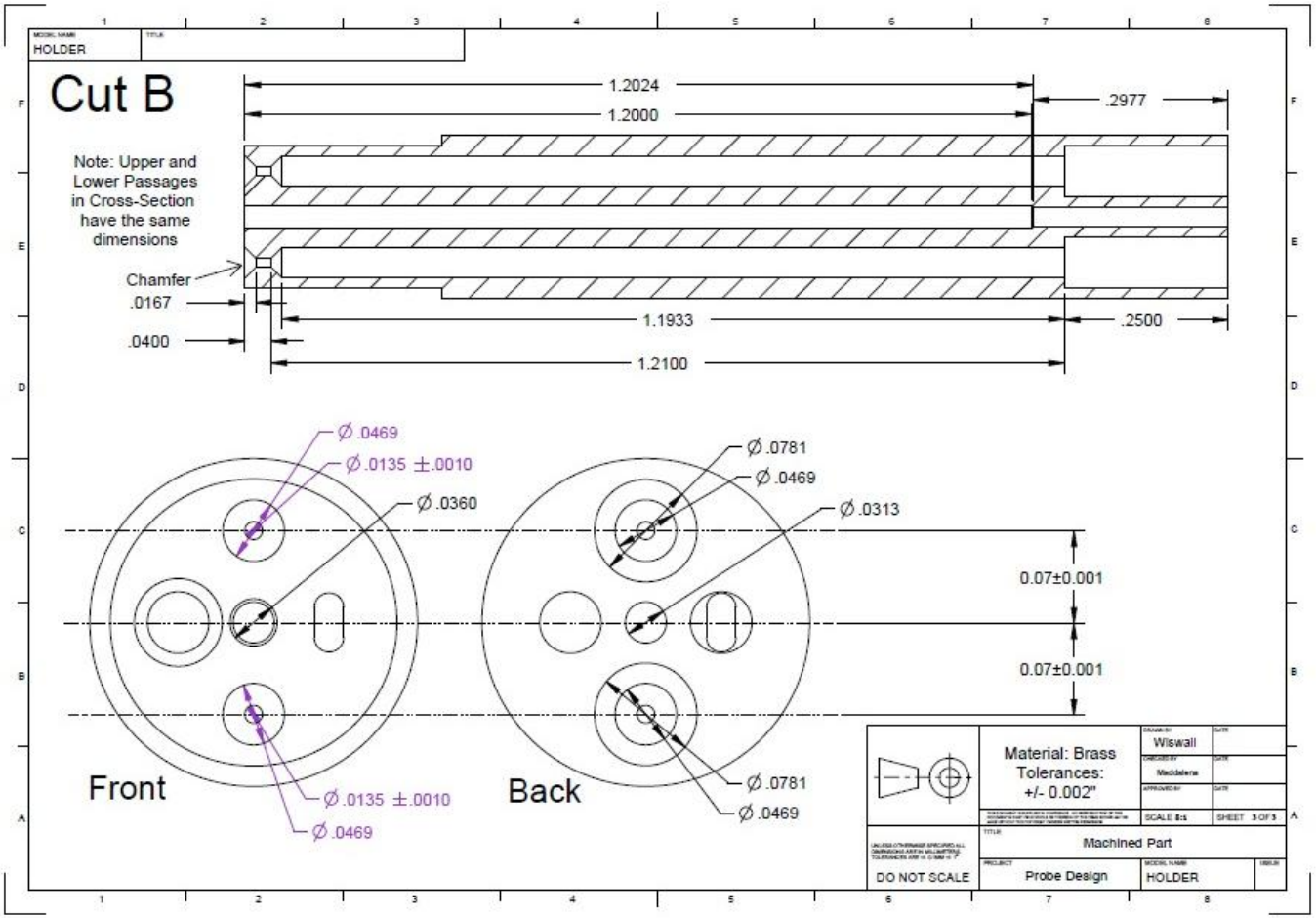

Figure 71: Holder Geometry 3

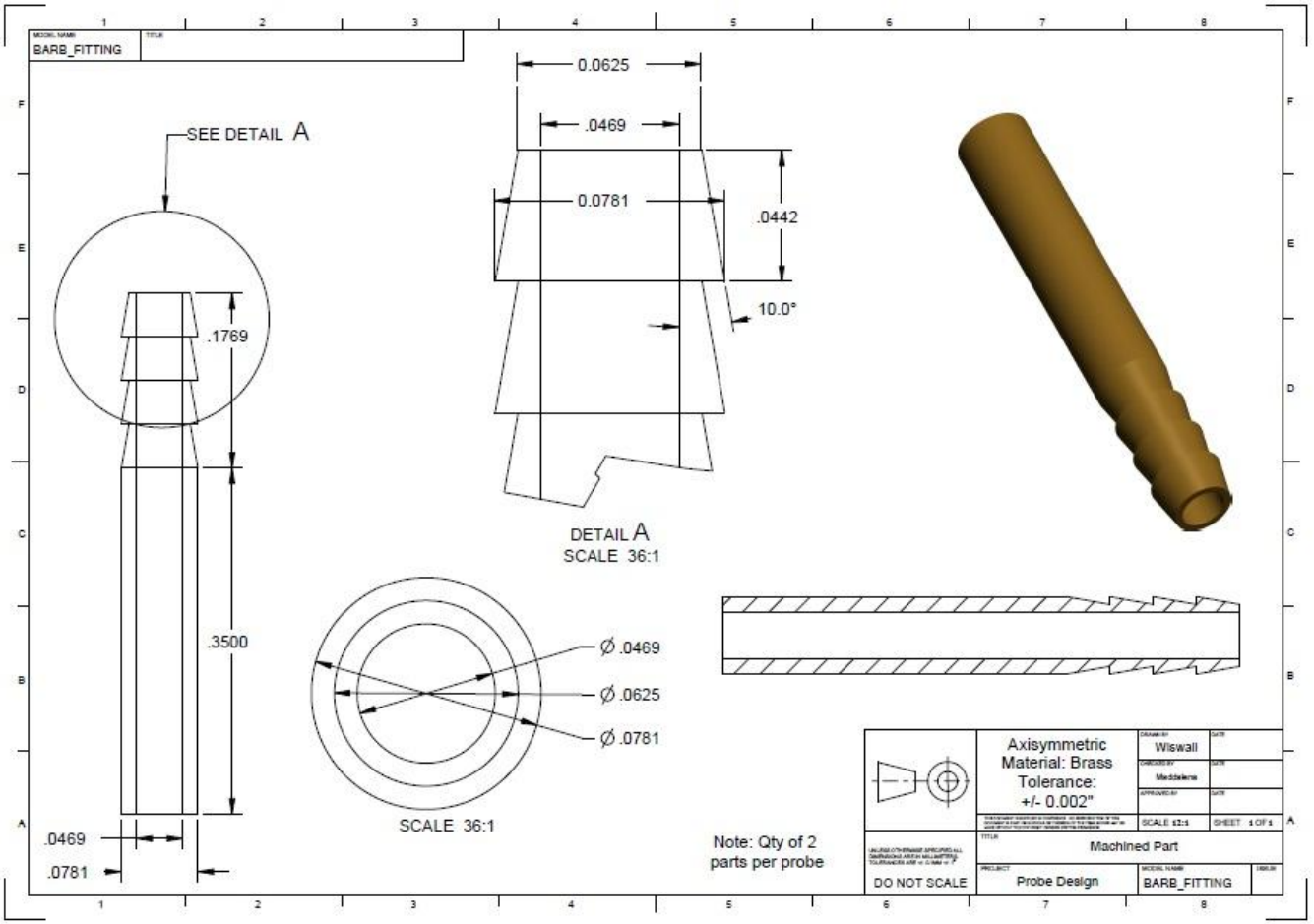

Figure 72: Barb Fitting Geometry

References

[1] Fry, R.S., “A Century of Ramjet Propulsion Technology Evolution”. Journal of Propulsion and Power, 20(1), Jan-Feb 2001.

[2] Brown, G. L., Rebollo, M. R., “A Small, Fast-Response Probe to Measure Composition of a Binary Gas Mixture,” AIAA J., Vol. 10 No. 5, p 649-652, May 1972.

[3] Birch, A. D., et. al., “Aspects of Design and Calibration of Hot-film Aspirating Probes used for the Measurement of Gas Concentration”, J. Phys. E: Sci. Instrum., 1986.

[4] Ng, W.F., Kwok, F.T., and Ninnemann, T.A. “Concentration Probe for the Study of Mixing in Supersonic Shear Flows”, AIAA Paper 89-2459, July 1989.

[5] Xillo, O. C., “A Sampling Probe for Fluctuating Concentration Measurements in Supersonic Flow”, Master’s Thesis, Virginia Polytechnic Institute and State University, 1998.

[6] Maddalena, L. “Investigations of Injectors for Scramjet Engines”, PhD Dissertation, Virginia Polytechnic Institute and State University, 2007.

[7] Blackshear, P., L. Jr., "Rapid-Response Heat Flux Probe for High Temperature Gases", ARS Journal, Vol. 32, No. 11, pp. 1709-1715, 1962.

[8] Devillers, J. F., Diep, G. B., “Hot-wire Measurements of Gas Mixture concentrations in a Supersonic Flow”, DISA info. 14, 1973 (pp. 29-36).

[9] Anderson, J. D. Jr., “Fundamentals of Aerodynamics”, 3rd ed., McGraw-Hill, New York, NY, 2001.

[10] Fuller, R.P. “Fuel Vortex Interactions for Enhanced Mixing in Supersonic Flow”, PhD Dissertation, Virginia Polytechnic Institute and State University, August 1996.

[11] Wilke, C.R. “A Viscosity Equation for Gas Mixtures”, The Journal of Chemical Physics, 18 (4): 517-519, 1950.

[12] Burgers, J. M., “Flow Equations for Composite Gases” Academic Press, 1969.

[13] Doebelin, E. O., “Measurement Systems: Applications and Design”, 5th ed., Tata McGraw-Hill, New Delhi, India, 2004.

[14] Incropera, F. P., Dewitt, D. P., Bergman, T. L., Lavine, A. S., “Fundamentals of Heat and Mass Transfer”, 6th ed., J. Wiley & Sons, Inc., Hoboken, NJ, 2005.

[15] “TSI Model 1750 Constant Temperature Anemometer User’s Manual”, Revision N, TSI Incorporated, February 2008.

[16] Pope, S. B., “Turbulent Flows”, Cambridge University Press, 2000.

[17] Waitz, I., A. et. al, “Enhanced Mixing with Streamwise Vorticity”, Prog. Aerospace Sci., Vol. 33, pp. 323-351, 1997.

[18] Marble, F. E., “Growth of a Diffusion Flame in the Field of a Vortex”, Recent Advances in the Aerospace Sciences, Plenum Publishing, New York, 1985.

[19] Vergine, F., Maddalena, L., “Evolution of Large-Scale Structures Generated by a Strut Injector in a Mach 2.5 Flow”, 50th AIAA Aerospace Sciences Meeting, AIAA Paper 2012-0332, January 9–12, 2012, Nashville, Tennessee.

[20] Vergine, F., Maddalena, L., Gamba, M., and Miller, V., “Supersonic Combustion and Flame-Holding Characteristics of Pylon Injected Hydrogen in a Mach 2.4 High Enthalpy Flow”, 50th AIAA Aerospace Sciences Meeting, AIAA Paper 2012-333, January 9–12, 2012, Nashville, Tennessee.

[21] Crisanti, M., Vergine, F., Maddalena, L., “Filtered Rayleigh Scattering Measurements in Helium-Air Mixing Experiments of Selected Streamwise Vortex Interactions in a Mach 2.5 Flow”, 52nd AIAA Aerospace Sciences Meeting, 2014 [future paper].

Biographical Information

John D. Wiswall was born in 1988 in Waco, Texas. In 2006, he graduated from Midway High School in Waco. In the same year, he began his bachelor's studies in the engineering department at Baylor University. In 2010 he graduated from Baylor University with a Bachelors degree in Mechanical Engineering, and married Amanda Neslony in October later that year. John enrolled at The University of Texas in Arlington in 2011 to pursue a graduate degree in Aerospace Engineering, being grateful for the opportunity to explore his specific field of interest at a higher academic level. He earned his Master's degree in Aerospace Engineering from UTA in August 2013 and plans to pursue an AE career in industry after graduation.